Harmonic and anharmonic phonons and associated thermal and electrical properties in thermoelectric clathrates

著者	WU Jiazhen
学位授与機関	Tohoku University
学位授与番号	11301甲第16580号
URL	http://hdl.handle.net/10097/61393

PhD Thesis

Harmonic and anharmonic phonons and associated thermal and electrical properties in thermoelectric clathrates

(熱電材料クラスレートにおける調和フォノンと
非調和フォノンおよび関連する電子物性)

Wu Jiazhen

Department of Physics
Graduate School of Science
Tohoku University
September, 2015

Harmonic and anharmonic phonons and associated thermal and electrical properties in thermoelectric clathrates

Jiazhen Wu[1, *]
[1] *Department of Physics, Graduate School of Science*
Tohoku University, Aramaki, Aobaku, Sendai 980-8578, Japan

INTRODUCTION

Thermoelectric energy conversion attracts a surge of interest, as it is considered to be a potential way to produce electric energy from waste heat as future technology. Thermoelectric efficiency is commonly evaluated by the figure of merit $ZT = \frac{S^2\sigma}{\kappa}T$, where S is the Seebeck coefficient, σ is the electrical conductivity and κ is the thermal conductivity. Therefore, a perfect thermoelectric material should be a "phonon-glass electron-crystal" (PGEC) material as proposed by Slack *et al.* [1]. Intermetallic type-I clathrates are regarded as such materials and have been widely studied [1–3].

A typical structure of clathrate-I is shown in Fig. 1, where the guest atoms reside in both dodecahedral (blue) and tetrakaidecahedral (orange) cages. Type-I clathrate shows very low κ like a glass due to the guest vibration phonon modes, but it can show a high σ like a metal according to the Zintl-Klemm concept [1]. Anharmonicity of phonons arising from the guest vibrations can suppress thermal conductivity, with exerting little influence on electron conductivity, both factors of which enable clathrates a PGEC material [1]. However, researches so far mainly emphasized on the thermoelectric properties of a limited number of clathrates, and there are only few studies concerning a variety of clathrates to find a general rule of the rattling phonon modes for designing new thermoelectric materials.

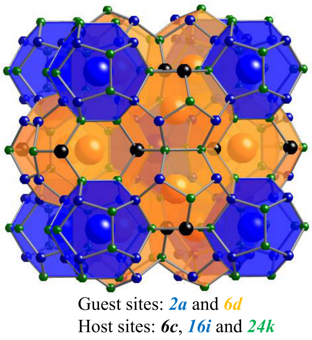

FIG. 1. A typical structure of type-I clathrate.

The present thesis describes a systematic study on phonons in type-I clathrates. The guest vibration energies, indicated by boson peaks in heat capacity (C_p), are shown to be rationalized in terms of a single unified exponential line for a series of clathrates. The unified picture indicates the quasi-harmonic nature of the guest-atom vibrations. Strong anharmonicity in guest-atom vibrations, emerging from quantum tunneling, is also studied by C_p measurements. In addition, we show that high quality single crystals are favored for improving thermoelectric performance in a clathrate system by focusing on Cu, Ag and Au containing clathrates.

EXPERIMENTS

Single crystals of a series of type-I clathrates were synthesized by applying a flux method. In particular, single crystals of Cu, Ag and Au containing clathrates were successfully grown by using a Sn-flux for the first time. The crystal quality was checked by X-ray powder and single crystal diffraction measurements. Physical properties were measured by using a physical properties measurement system (Quantum Design) and magnetic properties were measured by using a Quantum Design superconducting quantum interference device (Quantum Design).

RESULTS AND DISCUSSION

Boson peaks

Fig. 2 (a) shows the boson peaks appearing in C_p for a series of type-I clathrates. The C_p data can be well fitted by applying the Einstein and Debye models of solids, indicating that the guest-atom vibrations are almost harmonic and can be described by the Einstein oscillators. The harmonic fittings give the characteristic energies (ω_E) of the guest atoms. In order to find a general rule of ω_E for a variety of clathrates, many parameters are tested, and finally the space factor and the mass of a guest atom (m) are confirmed as the most important two factors. The mass factor is renormalized by applying a single harmonic oscillator model: $\omega = \sqrt{Fc/m}$, where Fc is the force constant describing the strength of the interactions between a guest atom and its surrounding cage atoms. By careful analyses, Fc is shown to be exponentially dependent on the free space parameter R_{free} as shown in

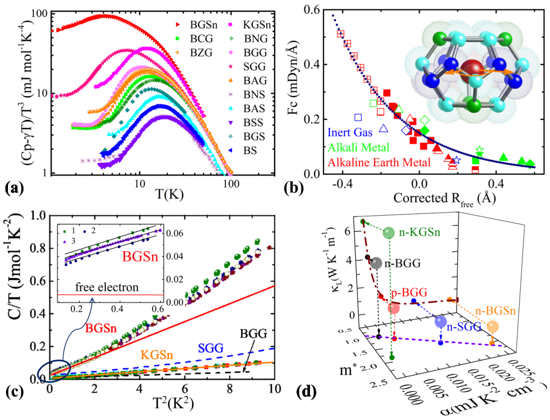

FIG. 2. (a) Boson peaks appearing in C_p (C_p/T^3 vs. T). (b) The unification of the excitation energies of boson peaks. (c) Temperature linear and time dependent C_p (C_p/T vs. T^2) for type-I clathrates. (d) The relationship of phonon anharmonicity, indicated by α, and lattice thermal conductivity (κ_L) and m^*.

Fig. 2 (b). A modified Morse potential, which is generally applied for intermolecular interactions, is used to describe the guest-framework interactions in the present work. It is revealed for the first time that the guest-framework interactions are essentially dominated by weak van der Waals type interactions and it shall be very important for designing thermoelectric materials from the view point of rattling phonons. Our conclusion can be confirmed by first principle calculations [4].

Tunneling states

The anharmonicity of guest vibrations increases as the guest atoms become off-centered, and κ is suppressed even more strongly [3]. At extremely low temperatures below 1 K, the phonon anharmonicity, indicated by tunneling states of the guest atoms, is observed as a temperature linear and time dependent C_p as shown in Fig. 2 (c). It is shown that the two terms in C_p, the temperature linear dependent term, due to the tunneling states ($\alpha\, T$), and conduction electron one (γ_e) were found to be successfully separated. Based on the obtained α values, the influences of the phonon anharmonicity on thermoelectric parameters are discussed as shown in Fig. 2 (d). The values of κ_L strongly decrease as the anharmonicity of phonons increases, while on the other hand the effective mass increases. Consequently, thermoelectric performance can be improved by including phonon anharmonicity. Although large free space is important for having off-centered guest atoms, the arrangement of the atoms/vacancies on the framework cage should also be equally considered.

Cu, Ag and Au containing clathrates

In the last chapter of the thesis, electrical transport properties are discussed for having a better understanding on the thermoelectric performance by focusing on Cu, Ag and Au containing clathrate single crystals. In a clathrate system, low κ is mainly due to the rattling phonons, and therefore the situation is different from those of other material systems, where κ can be largely reduced by grain boundaries. On the contrary, a decrease of grain boundaries gives rise to an increase of carrier mobility and leads to an increase of ZT values in clathrates. Fig. 3 shows that our single crystals have higher carrier mobility (μ) than that reported in the previous poly-crystalline work, especially for Cu containing clathrates. It is also shown that this high carrier mobility will lead to a better thermoelectric performance as $ZT \propto \mu$.

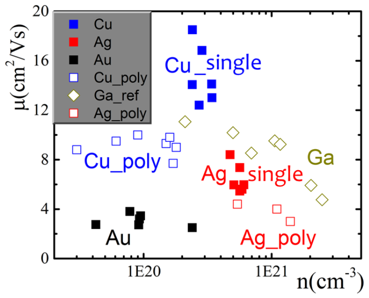

FIG. 3. Carrier mobility as a function of carrier concentration.

CONCLUSION

We made a systematic study on guest-atom vibrations by focusing on their harmonic and anharmonic behaviors in type-I clathrates. We discussed the boson peaks appearing at around 15 K as well as the tunneling states below 1 K in C_p measurements. Our systematic study on the phonons in clathrates provided a quantitative guideline for thermoelectric materials design from the viewpoint of the "PGEC" concept. We also showed the importance of single crystals for enhancing ZT values in clathrates.

---

* wujzphystu@gmail.com

[1] G. A. Slack, CRC Handbook of Thermoelectrics; Rowe, D. M., Ed.; CRC Press: Boca Raton, FL, 1995; pp 407-440.
[2] M. Christensen, et al. *Nature Materials* 7, 811 (2008).
[3] T. Takabatake, et al. *Rev. Mod. Phys.* 86, 669 (2014).
[4] J. Wu, et al. (submitted).
[5] J. Wu, et al. *Phys. Rev. B* 89, 214301 (2014).

Dedication

To God the Father for His amazing love,
and my beloved parents, Enzhi Wu and Xiangqing Xu.

Acknowledgements

I would like firstly to give thanks to my supervisor, Professor Katsumi Tanigaki, for his constant guidance, support and encouragement on my research work as well my life of studying abroad during the last five years. I appreciate him for the opportunities he provided, for studying in Tohoku University as well as attending many domestic and international conferences. In particular, I feel deeply grateful for his unlimited patience in teaching me about experiment and manuscripts preparation, and sometimes he even stayed with me until midnight. Without his contributions and suggestions, I could not finish this work.

I wish to thank Prof. Masami Terauchi, the chief referee of my dissertation and other referees: Prof. Akira Ochiai, Prof. Sumio Ishihara, and Prof. Takashi Takahashi for their valuable suggestions ever since my qualifying exam until my final defense.

Also I would like to thank all the members in my laboratory for the five years we spent together, especially Dr. Jingtao Xu for his kind help in teaching me about crystal growth and physical properties measurement during the first two years of my research life from 2010 to 2012. I wish to express my sincere thanks to Professor Hidekazu Shimotani for his help in making ab initio calculations by using Gaussian 09 code and Professor Kazuto Akagi for making first principle band calculations by using VASP code.

I want to thank the Ministry of Education, Culture, Sports, Science and Technology of Japan (MEXT) for the five-year financial support and their promotion of student education through the IGPAS program in Tohoku University. I would also like to give my thanks to the DIRECT office of Tohoku University, especially to the staff, Ms. Narumi Yamada and Ms. Junko Hori for their timely help in my daily life.

I want to thank my family: my parents, my brother and my sister. They always love me, support me, and pray for me unconditionally. Their comforting words is the source of my power. I would also like to give special thanks to my girlfriend Yichen for waiting for me for five years, even though we were staying apart. Her love and support is my future.

Finally, I want to thank God the Father for His amazing love. I would also like to thank the brothers and sisters in Christ in Sendai as well as in China.

Contents

List of Figures

List of Tables

Chapter 1

Introduction

This chapter serves as an introduction of the whole dissertation. In order to understand well of the research purpose and significance as well as the main content of the following chapters, we start with a review of the research background by focusing on energy issues in Section 1 and the specific thermoelectric energy conversion issue in Section 2. Section 3 describes the chemical and structural information as well as physical properties of clathrates, which are one of the potential materials for thermoelectric application as described in Section 2. We continue going deeper in clathrates in Section 4 to reveal the important role of rattling phonons in improving the thermoelectric performance. The physical properties associated with rattling phonons are also described. Section 5 presents a chapter-wise description of the dissertation and the key results. Figure 1.1 shows the overview of this chapter.

1.1 Background

Energy has become important since the origin of life, as it promotes all species to a wise direction, and the use of energy, such as fire, has been the elementary power for the human civilization as well as the development of society. The world's demand for energy has been increasing since

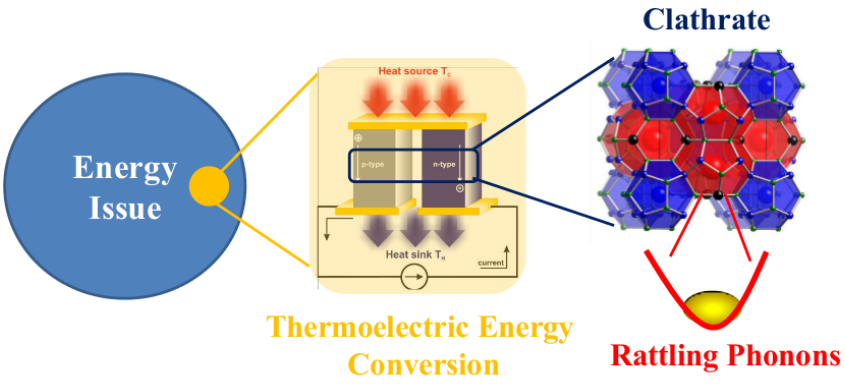

Figure 1.1: Overview of the content in Chapter 1, which serves as an introduction of the whole dissertation.

the industrial revolution, especially the recent several decades. Although energy provides a lot of convenience, such as electric power and motor vehicle etc., the associated problems are also obvious. For example, fossil fuels, which are the main energy source at present, can be used up in the near future and an energy crisis would appear. And the combustion of fossil fuels has already caused a lot of environment problems, such as smog, as well as global climate changes, such as the global warming. Therefore, it is quite necessary to develop sustainable and environmental friendly energy for long-term development. One way to achieve this goal is through the improvement of the energy utilization efficiency, because most energy becomes waste heat and diffuses to environment during the energy conversion process. Thermoelectric generator is one promising approach to convert the waste heat into useful electric power and has been widely studied both theoretically and experimentally [1–4]. Actually it has already been considered to replace the alternator in cars with a thermoelectric generator by mounting the generator on the exhaust stream to enhance the fuel efficiency [2, 5, 6].

In spit of the potential application prospect, the thermoelectric energy conversion efficiency, indicated by a dimensionless parameter: figure of merit ZT, is still low. Although the highest ZT reported recently for SnSe single crystal reaches 2.6 [7], it can not meet the request for wide applications. In order to maximize ZT, many conflicting parameters, which are electrical conductivity (σ), thermal conductivity (κ) and Seebeck coefficient (S) need to be optimized at the same time, and this will be discussed further in Section 2. Further more, in real application, the mechanical strength, chemical stability, toxicity and the price of a thermoelectric material should also be seriously taken into account. Therefore there are generally two targets for thermoelectric materials research: one is fundamental study to find out new approaches or guidelines for materials design; the other is materials engineering to make new desired compounds. In this work, we focus on the fundamental study of rattling phonons, which can suppress heat conduction efficiently, and thereby improve thermoelectric performance.

1.2 Thermoelectric energy conversion

The energy conversion between electricity and heat can be realized through Joule heating and thermoelectric effect. In the case of Joule heating, electric energy becomes thermal energy when an electric current passes through a conductor. Joule heating is independent of a measurement direction and the energy conversion process is irreversible. On the contrary, the thermoelectric effect is not a heat dissipation, the energy can be changed from electricity to heat and vice versa. The following paragraphs in this section will describe the thermoelectric effect and the associated researches.

1.2.1 Thermoelectric phenomena

The thermoelectric phenomena [4] were first discovered by T. J. Seebeck in 1821, as he observed a deflection of a compass needle in the presence of a loop composed of two metals where their junctions are exposed in deferent temperatures. Although, at beginning, Seebeck mistook it as thermomagnetic effect, a Danish physicist H. C. Ørsted corrected it and termed it "thermoelectricity" in 1823. Thirteen years after the discovery of Seebeck effect, J. C. A. Peltier, a French watchmaker, observed another thermoelectric effect, which was called Peltier effect afterwards. The relationship between Seebeck effect and Peltier effect was first derived by W. Thomson by using the theory of thermodynamics in 1855, and the third thermoelectric effect–Thomson effect was discovered at the same time as a result of his theory. A brief theory based description of the thermoelectric effect is shown below.

Seebeck effect describes an electromotive force induced by a temperature gradient. According to Figure 1.2, suppose different temperatures at A and B, and a galvanometer is connected between C and D, the differential Seebeck coefficient of the metal a and b can be defined as:

$$S_{ab}(T) = \lim_{\triangle T \to 0} \frac{\triangle V}{\triangle T} \tag{1.1}$$

where, $\triangle T$ is the temperature difference between T_{A} and T_{B} and $\triangle V$ is the corresponding voltage difference. It is noted that Seebeck coefficient is also called thermoelectric power or thermal electromotive force coefficient due to some historical reasons.

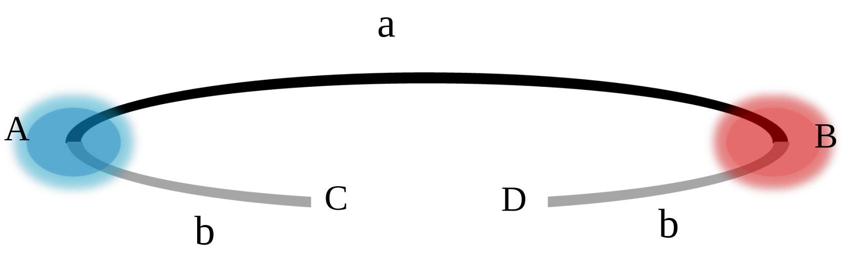

FIGURE 1.2: A basic thermocouple, composed of metal a and b. The junction A is supposed to have a lower temperature T_{A} and the junction B a higher temperature T_{B}. C and D are open for connecting a galvanometer to measure Seebeck effect, or a power source to carry out the measurement of Peltier effect. If C and D are closed, it becomes a simple thermoelectric circuit.

Peltier effect describes a small cooling or heating effect of a thermocouple with the passage of an electric current flow. The cooling and heating sides are reversible depending on the direction of an electric current. It can be shown in Figure 1.2, if an electric current I was applied in the loop by a power source between C and D, the ratio of the heating(at A otherwise B) or cooling (at B otherwise A) rate q to I is defined as Peltier coefficient:

$$\Pi_{ab} = \frac{q}{I} \tag{1.2}$$

Thomson effect is a reversible heating or cooling effect when an electric current passes through a homogenous conductor with a temperature gradient. The Thomson coefficient, β, is defined as:

$$\beta = \lim_{\triangle T \to 0} \frac{\triangle q}{I \triangle T} \tag{1.3}$$

where, $\triangle q$ is the rate of heat release or absorbtion when I goes through a temperature difference $\triangle T$.

The relationships of the three thermoelectric effects are formulated by Kelvin relations:

$$S_{ab}T = \Pi_{ab} \tag{1.4}$$

$$\frac{d\,S_{ab}}{d\,T} = \frac{\beta_a - \beta_b}{T} \tag{1.5}$$

The above relationships can be derived from the laws of thermodynamics [3, 4, 8] and are briefly shown here. Refer to Figure 1.2 again, if we suppose that C and D are closed, and there is a current around the loop and the system is isolated from its surroundings, the energy conservation law demands that the consumed electric energy should be equal to the generated heat. So

$$\int_A^B S_{ab}IdT = \int_A^B (\beta_a - \beta_b)IdT + ((\Pi_{ab})_A - (\Pi_{ab})_B)I \tag{1.6}$$

Here Joule heating is neglected, as we assume the electric current is extremely small. From Equation (1.6), we have the first relationship of the three thermoelectric coefficients:

$$S_{ab} = \beta_a - \beta_b + \frac{d\Pi_{ab}}{dT} \tag{1.7}$$

Another relationship of the three coefficients can be found according to the second law of thermodynamics. In order to achieve this aim, we have to assume that the process is reversible, though, actually, it is irreversible due to Joule heating and thermal conduction. A strict prove of the Kelvin relations, regardless of the reversibility of the process, is given in Appendix A by using the Onsager relations. If the total entropy of the isolated system is assumed to be unchanged, we have $\delta\, s = \frac{du}{T} = 0$. Thus,

$$\int_A^B d(\frac{I\Pi_{ab}}{T}) + \int_A^B \frac{(\beta_a - \beta_b)IdT}{T} = 0 \tag{1.8}$$

The equation can be simplified by differentiating both side with respect to T,

$$\frac{d\Pi_{ab}}{dT} - \frac{\Pi_{ab}}{T} + \beta_a - \beta_b = 0 \tag{1.9}$$

According to Equations (1.7) and (1.9), the Kelvin relations Equations (1.4) and (1.5) can be easily derived. It should be noted that the Kelvin relation Equation (1.4) is only valid for materials with time-reversal symmetry, otherwise the equation should be in a more complicated form [3]. It should also be noted that S_{ab} and Π_{ab} are for junctions of two conductors, while β is for a single conductor. For calculating the absolute Seebeck coefficient S_a, one has to know S_b, and this can be realized at low temperatures, where, say for example b was a superconductor and $S_b = 0$. (The same for absolute Peltier coefficient.) However, the superconductor-approach is not guaranteed for temperatures higher than Tc of the applied superconductor. In order to solve the problem, one can change the Equation (1.5) to be $\frac{d\,S}{d\,T} = \frac{\beta}{T}$, and hence $S = \int_0^T \frac{\beta}{T}dT$. This means the absolute S can be alternatively obtained by measuring the Thomson coefficient[9]. Actually, the S of the metal lead was derived by using this method, and the lead has been used as a standard material for measuring Seebeck coefficients of other materials since then.

Additionally, in the presence of a magnetic field, the above thermoelectric effects should be changed, and there are two more effects: Nernst effect and Ettingshausen effect which are corresponding to Seebeck effect and Peltier effect, respectively [3, 4]. Among all the thermoelectric effects, Seebeck effect is most easily to be measured and has been most widely studied for energy-saving researches.

1.2.2 Thermoelectric performance and the optimization method

The thermoelectric effects are truly crucial for thermoelectric energy conversion; however the performance does not solely depend on these effects, other factors, such as electrical conductivity and thermal conductivity should also be seriously considered. Here we take a thermoelectric generator as an example to derive the energy conversion efficiency[3].

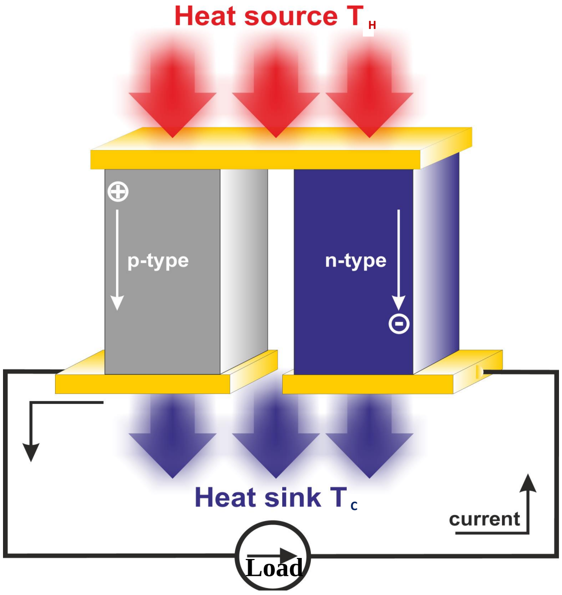

FIGURE 1.3: A thermoelectric generator based on the Seebeck effect.

According to Figure 1.3, the generator efficiency can be written as:

$$\eta = \frac{\varepsilon_{\text{load}}}{\varepsilon_{\text{heat}}} \tag{1.10}$$

where ε_{load} is the energy supplied to the load and ε_{heat} is the heat energy absorbed at hot junction and they can be expressed in the following forms:

$$\begin{aligned} \varepsilon_{\text{load}} &= I^2 R_{\text{load}} \\ \varepsilon_{\text{heat}} &= \kappa \triangle T + S_{\text{pn}} T_H I - \frac{1}{2} I^2 R_{\text{device}} \end{aligned} \tag{1.11}$$

where $I = \frac{S_{\text{pn}} \triangle T}{R_{\text{load}} + R_{\text{device}}}$ is the electric current, κ is the total thermal conductivity of the device, $\triangle T = T_H - T_C$ is the temperature deference. ε_{heat} is composed of heat conduction (the 1st term), a compensation to Peltier effect (the 2nd term) and half of the Joule heating, which returns to the heat source (the 3rd term). Therefore the efficiency becomes,

$$\eta = \frac{r \triangle T}{\frac{(r+1)^2}{Z} + r T_H + T_M} \tag{1.12}$$

where $r = \frac{R_{\text{load}}}{R_{\text{device}}}$, $Z = \frac{S_{\text{pn}}^2}{\kappa\, R_{\text{device}}}$ and $T_M = \frac{T_H+T_C}{2}$. One can find a maximum η when $\eta'(r) = 0$, and this leads to $r = (1 + ZT_M)^{1/2}$. The maximum efficiency can then be written as,

$$\eta_{\max} = \frac{T_H - T_C}{T_H} \frac{\sqrt{1 + Z\bar{T}} - 1}{\sqrt{1 + Z\bar{T}} + T_C/T_H} \tag{1.13}$$

As shown in Equation (1.13), $\eta_{\max}$ would become the efficiency of an ideal thermodynamic machine, if ZT tends to infinity; however it is not always good to have the maximum efficiency, because one need to consider power output as well (In this case, r might not equal to $(1+ZT_M)^{1/2}$, but we ignore the details here).

According to Equation (1.13), thermoelectric performance is determined by the dimensionless parameter ZT, which is also call the "figure of merit". The ZT for a single thermoelectric material can be defined as:

$$ZT = \frac{S^2\sigma}{\kappa}T \tag{1.14}$$

In order to improve ZT, one has to optimize S, σ and κ simultaneously, which however is quite difficult in practice.

According to Appendix A, the Seebeck coefficient for a single material can be expressed by the Mott equation [10]:

$$S = \mathbf{L}_{ET}(\mathbf{L}_{EE})^{-1} = \frac{\pi^2}{3}\frac{k_B^2 T}{e}(\frac{d\ln\sigma}{d\varepsilon})_{\varepsilon=\varepsilon_F} \tag{1.15}$$

where k_B is the Boltzmann constant and ε_F is the Fermi energy. For metals or degenerate semiconductors, S is written as [11]:

$$S = \frac{8\pi^2}{3h^2}\frac{k_B}{e}k_B T m^*(\frac{\pi}{3n})^{2/3} \tag{1.16}$$

where n is the carrier concentration, h is the Planck constant and m^* is the effective mass. On the other hand, electrical conductivity is normally expressed as $\sigma = ne\mu$, in which μ is electrical mobility. Therefore the optimization of S and σ simultaneously via carrier concentration (n) and effect mass (m^*) conflict with each other. A decrease in carrier concentration gives rise to a decrease of electrical conductivity while an increase of thermoelectric power and vice versa. Similarly, an increase of effective mass leads to an increase of thermoelectric power while a decrease of electrical conductivity through electrical mobility.

The optimization of thermal conductivity (κ) conflicts with the optimization of σ as well, because the electron contribution to thermal conductivity (κ_e) directly connect with σ via Wiedemann-Franz Law. The total thermal conductivity is given by,

$$\kappa = \kappa_e + \kappa_{ph} = LT\sigma + \kappa_{ph} \tag{1.17}$$

where κ_{ph} is the phonon contribution to heat conduction, L is the Lorenz number, which is a constant for metals. The above conflicts of the optimization between S and σ as well as σ and κ via carrier concentration are described in Figure 1.4 [2].

In spite of the conflicts, ZT reaches a maximum value when n is between $10^{19}cm^{-3}$ and $10^{20}cm^{-3}$. The n dependent ZT and associated parameters indicate that thermoelectric performance can be optimized by tuning carrier concentration. Actually a lot of studies have been focused on carrier

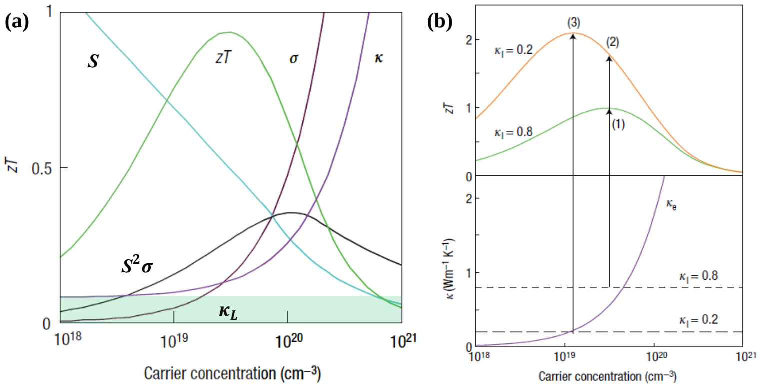

Figure 1.4: Optimization of ZT by carrier concentration tuning [2]. (a) The carrier concentration dependent κ, S, σ, power factor ($S^2\sigma$) and ZT. (b) Optimization of ZT by modifying lattice thermal conductivity (κ_L).

concentrations by doping for achieving high ZT values [2, 3, 12]. In addition to n, electrical mobility μ is also useful to maximize ZT. For semiconductors, ZT can be approximately expressed by, $ZT \propto \frac{m^{*3/2}\mu}{\kappa_L}T$, if $\kappa_L \gg \kappa_e$. At a same carrier concentration, an increase of μ would give rise to an increase of ZT directly. We will discuss this with more details in chapter 5. Besides, effective mass and band structure character are two important factors as well [12, 13].

It should be noted that the above approaches mainly revolve around electrical properties, while the role of phonon properties are equally important, and phonon engineering mainly aims at lowering lattice thermal conductivity (κ_L). Figure 1.4 (b) shows the significant influence of κ_L to ZT values. For simplicity κ_L is expressed as, $\kappa_L = \frac{1}{3}Clv$, where C is the heat capacity, l is the phonon mean free path and v is sound velocity. Therefore there are several ways to slow down heat transport: (1) Making non-crystalline structures (quasi-crystal and glass structures). (2) Increasing phonon scattering rate in crystalline materials by including point defects (doping, alloying, etc.) [2, 14], phonon anharmonicity [7], resonant scattering [15] and nano-structuring [16–18], which is very hot recently. (3) Lowering phonon speed by bending the acoustic branches [19]. However the methods for lowering phonon conduction sometimes lead to low electrical conductivity as well. In order to avoid the problem, a conceptual ”phonon-glass electron-crystal” (PGEC) has been proposed by Slack *et al.* [3]. Intermetallic clathrates [19] and filled skutterudites [20] are regarded as potential PGEC compounds due to their unique cage structures and rattling phonon modes, and therefore have been widely studied for thermoelectric application. More details about the two kinds of compounds and rattling phonons will be given below.

1.2.3 Thermoelectric materials

Although thermoelectric effects are universal effects for every kind of material, only those materials with $ZT > 0.5$ are regarded as thermoelectric materials [3]. Metals are good electrical conductors, while good thermal conductors as well and normally show very low thermoelectric power (fig. 1.4), therefore they are not thermoelectric materials. On the other hand, insulators normally possess high thermoelectric power, but they are very bad electrical conductors (fig. 1.4) and therefore not thermoelectric materials. Consequently, a good thermoelectric material should be a semiconductor with a appropriate width of band gap and an intermediate amount of carrier concentrations. For the completeness of the introduction for thermoelectricity, it is necessary to briefly introduce some thermoelectric materials and their advantages here.

Chalcogenide compounds consist of many kinds of materials, including sulphides, selenides and tellurides. Many of these materials are found to be good thermoelectric materials, because they are semiconductors with energy gaps between 0.1-0.8ev [12] and they have high electrical mobilities as well as strong phonon anharmonicities, which result in very low thermal conductivity [3, 7, 12, 21]. Typical compounds are $(Bi/Sb)_2Te_3$, which show ZT values around 1 below room temperatures (RT) and a ZT value of 2.4 at RT for thin films [22], PbTe, which has a maximum $ZT \approx 0.8$ at about 770K [3] (intermediate temperatures) and SnSe, which possesses a ZT value as high as 2.6 at 923K [7] (the highest value for bulk materials so far). There are many more Chalcogenide compounds for thermoelectric applications [3, 12].

Half-Heusler Intermetallic Compounds are studied for thermoelectrics because they have high power factors ($S^2\sigma$) and they are easily synthesized and they are very stable with almost zero sublimation at even 1000°C [3]. With high melting points of 1100°C-1300°C, Half-Heusler alloys are applied at high temperatures. A high ZT value of 0.81 has been reported for $Hf_{0.75}Zr_{0.25}NiSn_{0.975}Sb_{0.025}$ at 1025K. However the relative high thermal conductivities of these compounds limit the maximum ZT values to be less than 1 so far.

Some **Metal Oxides** are recently found to be potential p-type thermoelectric materials, especially cobaltates [3, 12]. The typical examples are Na_xCoO_2, which have high power factors and low thermal conductivities. It has been reported that the low κ of $Na_{0.8}CoO_2$ is ascribed to an Einstein-like rattling phonon mode of the sodium ions [23]. The importance of rattling phonons, particularly in clathrates, will be discussed later on. The maximum ZT was obtained at 800 K with a value larger than 1 for a single-crystal sample of cobaltates [12].

Filled skutterudites are identified as the conceptual "PGEC" compounds as described earlier. They are composed of A_xXY_3, where X is Co, Rh, or Ir, Y is P, As or Sb, and A is an alkali/alkaline-earth/rare-earth metal element; where XY_3 is the expression for an unfilled skutterudite, and A represents a filled element with $0.25 \geq x \geq 0$. The filled elements work very importantly on one hand as electron donors to tune power factor values, on the other hand as rattlers to provide strong anharmonic phonon scatterings. The highest ZT obtained for skutterudites so far is 1.25 at 900 K in the case of compounds $Ba_{0.30}Ni_{0.05}Co_{3.95}Sb_{12}$ [24].

Intermetallic clathrates is another class of "PGEC" materials and the materials that will be studied in this dissertation. Similar to filled skutterudites, clathrates are composed of empty frameworks and filled rattlers, which lead to high power factor values and low thermal conductivity values. The highest ZT was reported to be 1.35 at 900 K for $Ba_8Ga_{16}Ge_{30}$ [25]. More details of clathrates will be given in the next section.

Besides the compounds introduced above there are many more thermoelectric materials[2–4, 12], which will not be described in this dissertation. From the next section, we will focus on clathrates and the important rattling phonons.

1.3 Clathrates

The word *clathrate* is derived from the Latin *clatratus*, which means latticed or encaged [3]. It describes a class of materials, which consist of cage structures and filled molecules/atoms. It should be noted that the cavities of cages in clathrates is not large enough to allow a pass through of the fillers, not like the situation in zeolites, where fillers can move from one place to another and even escape from the compounds. In the clathrate family there are two branches: clathrate hydrate and intermetallic clathrate, both of which are related to energy storage in different ways. Clathrate hydrates are normally applied to store combustion gases, such as methane; while intermetallic clathrates are used for thermoelectric energy conversion as introduced earlier.

1.3.1 Clathrate hydrate

Clathrate hydrates (CH) are found to occur naturally in large quantities on the deep ocean floor and in the ice-cores of the Arctic and Antarctic, where a large amount of methane is stored in these minerals. These compounds are water-based solids, physically resembling ice, where gas molecules (Ar, Kr, Xe, Cl_2, O_2, N_2, H_2; CO_2, CH_4, H_2S etc.) are trapped inside the cages formed by the hydrogen bonds of water molecules. The first report of clathrate hydrate, $Cl_2[8H_2O]$, was given by H. Davy [26] and it was then studied by M. Faraday [27]. CH are formed under low temperatures and high pressures when water is mixed with a certain amount of gas molecules, without which, the water framework of clathrates collapses and a normal ice structure appears. It is noted that the formation and decomposition of a CH are not chemical reactions but first order phase transitions.

The structure of CH was not know until x-ray diffraction experiments were made by Stackelberg *et al.* [3, 28, 29]. The first structure, which is now known as type-I structure, was established to be cubic symmetry with space group $Pm\bar{3}n$. The structures of other types were obtained afterwards. Many years later, CH was classified into seven different structural modifications denoted by roman letters I-VII by Jeffrey *et al.* [30]. They are type-I with unit cell formula X_8Y_{46} and space group $Pm\bar{3}n$; type-II with $X_{24}Y_{136}$ and $Fd\bar{3}m$; type-III with $X_{30}Y_{172}$ and $P4_2/mnm$; type-IV with $X_{14}Y_{80}$ and $P6/mmm$; type-V with $X_{12}Y_{68}$ and $P6_3/mmc$; type-VI with $X_{16}Y_{156}$ and $I\bar{4}3d$; and type-VII with X_2Y_{12} and $Im\bar{3}m$. Here X is a gas molecule that accommodates inside a cage and Y is a framework molecule (normally water molecule). Among these types, CH-I is the most stable compounds.

1.3.2 A brief review of intermetallic clathrates

Intermetallic Clathrates, first reported by Cros *et al.* [31], are a class of compounds characterized by cagelike polyhedral hosts composed mainly of the IVth-group elements such as Si, Ge, or Sn with alkali metal or alkaline-earth metal or rear earth metal elements accommodated inside the cages as guest atoms. The framework elements can be substituted by transition metal elements or other main group elements (IIIth-, Vth-, VIth-, or VIIth-group). They have three structures in common with clathrate hydrates: type-I, II and III, and two additional structure types: type-VIII and type-IX [3]. The typical structures of intermetallic clathrates of different types are shown in Figure 1.5.

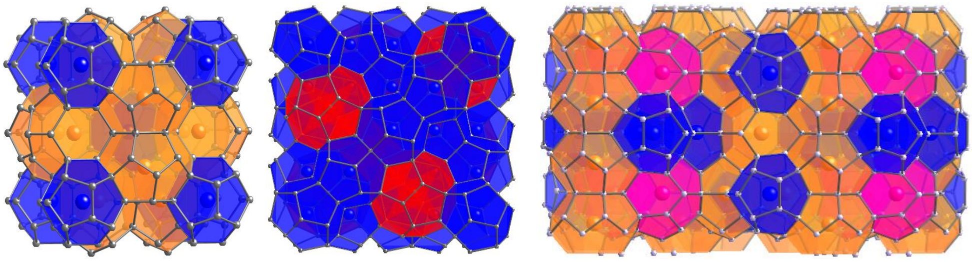

Type-I clathrate
(space group $Pm\bar{3}n$)

Type-II clathrate
(space group $Fd\bar{3}m$)

Type-III clathrate
(space group $P4_2/mnm$)

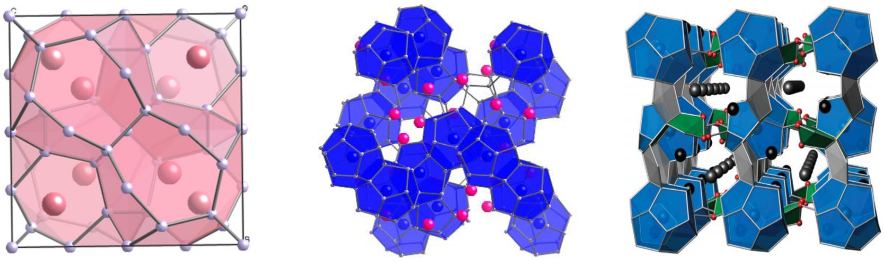

Type-VIII clathrate
(space group $I\bar{4}3m$)

Type-IX clathrate
(space group $P4_132$)

Clathrate $oP60$
(space group $Pmna$)

Figure 1.5: Crystal structures of intermetallic clathrates.

Type-I clathrate is composed of two kinds of polyhedra: two dodecahedra (blue) and six tetrakaidecahedra (orange) in one unit cell (Figure 1.5). The dodecahedron is made up of 12 pentagons faces and the tetradecahedron is made up of 12 pentagons as well as 2 hexagons. The composition can be summarized as $[5^{12}]_2[5^{12}6^2]_6$ according to P. Rogl [3]. Typical compounds of clathrate-I are Ba_8Si_{46}, $Ba_8Ge_{43}\square_3$ and their derivative ternary or quaternary compounds and many other compounds with Sn frameworks.

Type-II clathrate is also composed of two types of cages: two dodecahedra indicated by blue color and six hexadecahedra indicated by red color in one unit cell (Figure 1.5). The dodecahedron here is the same as that in type-I clathrate and the hexadecahedron is composed of 12 pentagons and 4 hexagons. The composition is written as $[5^{12}]_2[5^{12}6^4]_6$. Typical compounds of clathrate-II are Na_xSi_{136} and $Na_{16}Cs_8Ge_{136}$.

Type-III clathrate is made up of three kinds of cages: ten dodecahedra (blue), sixteen tetrakaidecahedral (orange) and four pentadecahedra (dark pink) in one unit cell ($[5^{12}]_{10}[5^{12}6^2]_{16}[5^{12}6^3]_4$). Typical compounds of this type are $Cs_{30}Na_{1.33x-10}Sn_{172-x}$, where $x \sim 9.6$ [32].

Type-VIII clathrate is made up of eight deformed pentadecahedral cages indicated by pink color in the figure ($[3^34^35^9]_8$). Actually it can be regarded as an open framework compound and the α phase compound of type-I clathrate (β phase). Typical type-VIII compounds are $Ba_8Ga_{16}Sn_{30}$ and $Eu_8Ga_{16}Ge_{30}$.

Type-IX clathrate is another open framework clathrate compound, which is composed 8 dodecahedral cages (blue) and other undefined framework compositions. Typical compounds are $Ba_{24}Si_{100}$, $Ba_{24}Ge_{100}$ and $Ba_6In_4Ge_{21}$. In addition, there are two more types of intermetallic clathrates: type $oP60$ represented by $BaGe_5$ [33] as shown in Figure 1.5 and $Ba_8Cu_{16}P_{30}$/$Ba_8Au_{16}P_{30}$ [34] type clathrate (space group, $Pbcn$).

Similar to clathrate hydrates, the number of type-I compounds is dominant among all the intermetallic clathrate species, therefore they have been most widely studied. A more detailed description of type-I clathrate is given below.

1.3.3 Type-I clathrates

Formation

Different from CH, the formation of intermetallic clathrate is chemical reaction, during which the cage-framework atoms are bonded together by diamond-like sp^3 covalent bonds and guest atoms are trapped inside the cages simultaneously as electron acceptors or donors depending on the guest species. According to the periodic table of elements shown in Figure 1.6, type-I clathrates are generally divided into three groups: binary clathrate (BC), ternary clathrate with cation guests (TC+) and ternary clathrate with anion guests (TC-, also known as inverse clathrate).

(1)A binary clathrate is composed of a green and a red elements, but it is not a random combination of the two elements; only Ba-Si, Ba-Ge, Na-Si, K-Si, Rb-Si, Cs-Si, K-Ge, Rb-Ge, Cs-Ge, K-Sn, Rb-Sn and Cs-Sn clathrates actually exist [31, 35–40]. Normally, this group of compounds are parent materials for having their ternary derivatives except for Na-Si and Cs-Si systems, where ternary compound hasn't been reported yet. Although binary compounds of Sr-Si, Sr-Ge, Ba-Sn and Eu-Ge haven't been obtained so far, their ternary derivatives, known as Sr-Al-Si, Sr-Ga-Si, Si-Ga-Ge, Eu-Ga-Ge and Ba-Ga-Sn clathrates have been well studied [41–44]. (2) A ternary clathrate with cation guests is composed of a green, a pink and a red elements as shown in

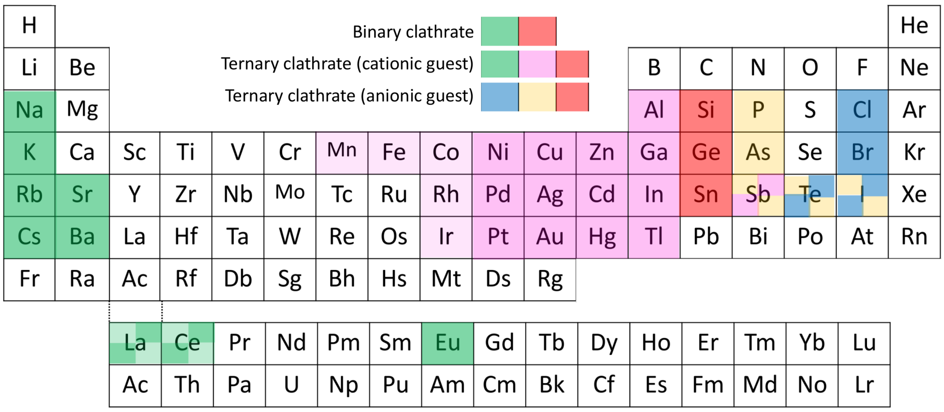

FIGURE 1.6: Formation of intermetallic clathrates. Elements with green color can be applied as cation guests, which provide electrons to the framework. Elements with blue color are applied as anion guest, which accept electrons from the framework. Elements with mixed green and light green colors (Ce and La) are those which have to combine with other "green" elements so as to be guest atoms [45]. Elements with mixed blue and orange colors are those which can be applied as either guest atoms or cage atoms. Framework cages are mainly composed of the elements with red color, which can be partially substituted by either the elements with pink color in the case of cation guests or the elements with orange color in the case of anion guests. Sb can be found in both cases. Clathrates, which contain the elements with light pink color, are rarely reported.

clathrate with cation guests is composed of a green, a pink and a red elements as shown in

Figure 1.6. This group of compounds are relatively easily synthesized and have been most broadly concerned for thermoelectric interest. Different from metallic BC's, TC+'s are normally metals or semiconductors, whose carrier concentration can be tuned for optimizing their thermoelectric performance. (3) A ternary clathrate with anion guests is composed of a blue, an orange and a red elements as shown in Figure 1.6. Comparing to TC+'s, TC-'s are rather difficult to be synthesized and most of them are bad conductors. Therefore they have not been widely concerned for thermoelectric application [46, 47]. In addition, researchers have found another type of clathrate-I, which is not based on group 14 elements but group 15 elements [48].

Zintl-Klemm Concept [49] can be applied to interpret the formation of the intermetallic compounds. According to the concept, the interaction of a guest atom and its surrounding framework is understood as charge transfer, and actually this point has been verified by theoretical calculations (See ref. [50] and chapter 3). In the case of TC-, a guest atom receives one or two electrons from the framework, and the electron balance can be found as (take $\mathrm{Ge_{38}P_8I_8}$ as an example),

$$\mathrm{Ge_{38}P_8I_8} \;=\; [(4b)\mathrm{Ge}^0]_{38}[(4b)\mathrm{P}^{1+}]_8[\mathrm{I}^{1-}]_8$$

where $4b$ means the sp^3-type 4 bonds. As for TC+, a guest atom gives one or two electrons to the framework, and the electron balance is expressed as (take $\mathrm{K_8Ga_8Sn_{38}}$, $\mathrm{Ba_8Ga_{16}Ge_{30}}$ and $\mathrm{Ba_8Cu_{5.3}Ge_{40.7}}$ as examples):

$$\mathrm{K_8Ga_8Sn_{38}} \;=\; [\mathrm{K}^{1+}]_8[(4b)\mathrm{Ga}^{1-}]_8[(4b)\mathrm{Sn}^0]_{38}$$

$$\mathrm{Ba_8Ga_{16}Ge_{30}} \;=\; [\mathrm{Ba}^{2+}]_8[(4b)\mathrm{Ga}^{1-}]_{16}[(4b)\mathrm{Ge}^0]_{30}$$

$$\mathrm{Ba_8Cu_{5.3}Ge_{40.7}} \;=\; [\mathrm{Ba}^{2+}]_8[(4b)\mathrm{Cu}^{3-}]_{5.3}[(4b)\mathrm{Ge}^0]_{40.7}$$

In this sense, the charge balance determines the composition ratio between the substituted element (a pink or orange element in fig. 1.6) and the 14-group element (red) in one compound. However, actual composition ratios can deviate from stoichiometric composition ratios and carrier concentrations can thus be tuned as from n-type to p-type as well as from semiconductor to conductor.

Similar to TC+, a guest in BC donates one or two electrons to its surroundings, but there is no electron acceptor in a complete host framework, so these electrons become itinerant carriers and the BC becomes a metal. Take $\mathrm{Ba_8Si_{46}}$ as an example, the electron transfer is written as:

$$\mathrm{Ba_8Si_{46}} \;=\; [\mathrm{Ba}^{2+}]_8[(4b)\mathrm{Si}^0]_{46} + 16e^{1-}$$

In the case that a host framework is not complete but has some vacancies, then the electrons from guest atoms will be transferred to dangling bonds near those vacancies, a charge balance can be obtained as (for $\mathrm{K_8Sn_{44}\square_2}$):

$$\mathrm{K_8Sn_{44}\square_2} \;=\; [\mathrm{Ba}^{2+}]_8[(3b)\mathrm{Si}^{1-}]_8[(4b)\mathrm{Si}^0]_{38}$$

Nevertheless, this rule is not always right, because $\mathrm{Ba_8Ge_{43}\square_3}$ is an exception. Although there are three vacancies, there are four itinerant electrons in one unit cell as well. This indicates that, in addition to the Zintl concept, there are other factors, which influence compositions and occupancies. As one shall see it later on, structure is one of the most important factors. It deserves to note two points here: (1) The symmetry of BC can be lowered by including vacancies and a superlattice can be expected (the space group is modified to be $\mathrm{Ia\bar{3}d}$). (2) The charge transfer is usually not complete and covalent host-guest interactions have been observed [50, 51].

Structure

The typical structure of clathrate-I is shown in Figure 1.7, where the atomic sites information can be found in Table 1.1. According to Table 1.1, the chemical formula of type-I clathrate in one unit cell can be written as G_8H_{46}, where G and H stand for guest and host respectively. We have already used this formula for describing the Zintl concept. There are general two ways to describe the three dimensional structure (fig. 1.7). One was suggested by Demkov et al. [52] that the tetrakaidecahedral cages are joined together through their hexagonal faces to form pillars, which are arranged to construct the final structure (dodecahedral cages are nothing but the remained voids). The other description starts from dodecahedral cages: they connect one another through $16i$ sites forming a scaffold structure with vacancies at $6c$ sites, and tetrakaidecahedral cages appear once these vacancies are filled with host atoms. The latter approach may help to explain the preference for vacancies and lower valence substitution elements on the 6c site [53]. As shown in Figure 1.7, there are several characters of the bonding between different host sites: $6c$ sites don't connect $16i$ sites and any other $6c$ sites; every $24k$ site has two $16i$, one $6c$ and one $24k$ sites as its neighbors.

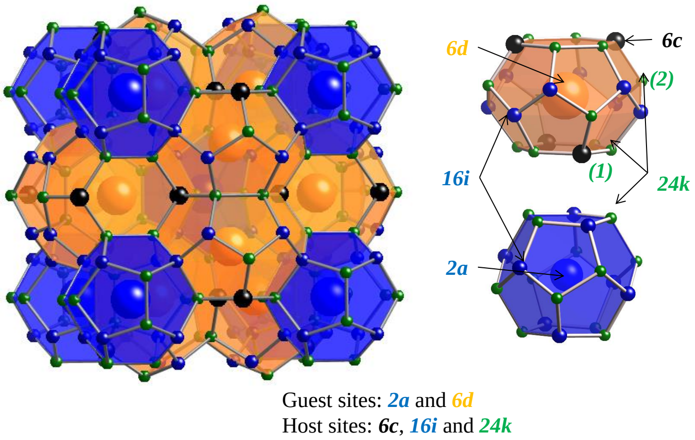

Figure 1.7: Crystal structure of type-I clathrate. Atoms in different sites are indicated by different colors. The two types of cages: dodecahedral cage (blue) and tetrakaidecahedral cage (orange) are picked out as shown on the right side. According to the distance between a guest atom and a host atom, $24k$-site atoms in tetrakaidecahedral cages are classified into two groups: $24k(1)$ on six-member rings and $24k(2)$ which is not on six-member rings. However, the $24k$ atoms in dodecahedral cages are identical.

As described earlier, a dodecahedral cage consists of 12 pentagon faces. The distance between a $2a$-guest atom and the surrounding host atoms are almost uniform, though some distortion might appear on $24k$ and $16i$ sites (fig. 1.7) due to another element substitution. In consequence, the vibration of $2a$-guest atoms are almost uniform and direction independent. On the other hand the cage radii of a tetrakaidecahedral cage are non-uniform and the guest vibrations are direction dependent. The space between the two parallel hexagon faces of a tetrakaidecahedral cage are shorter than the space of the other two dimensions (fig. 1.7). Therefore $6d$-guest atoms have two different types of vibration modes: two degenerate modes parallel to the six-member rings (6d parallel mode) and one mode perpendicular to the hexagon rings (6d vertical mode).

Table 1.1: Atomic sites and their coordinates in type-I clathrates (space group: $Pm\bar{3}n$). The m value for $16i$ site is around 0.185, and the n and q values for $24k$ sites are around 0.31 and 0.12, respectively. These values are not settled for different compounds, which indicates a distortion of the cage. It should be noted that the distortion only happens on $16i$ and $24k$ sites, while the other sites are fixed.

atom	site	x	y	z
G1	2a	0.00	0.00	0.00
G2	6d	0.25	0.50	0.00
H1	6c	0.25	0.00	0.50
H2	16i	m	m	m
H3	24k	0	n	q

The tetrakaidecahedral cage radius, which is defined by the distance between the guest atom and a host atom, are expressed in Figure 1.8 as scaled by their lattice constant a's. It clearly shows the non-uniform situation described above, as four different cage radii, defined in the figure, can be observed. The atoms at hexagon rings ($6c$ and $24k(1)$) are found closer to the cage center in distance than the atoms locating at the other sites ($16i$ and $24k(2)$). The shortest distance of $24k(1)$-$6d$ indicates the strongest repulsive interaction between the two atoms on this two sites. Once guest-off-center behaviors appear [41] (will be described later on), the guest atoms tend to be pushed to other host sites, and thus the off-centered sites are not on the same plane due to the cage symmetry.

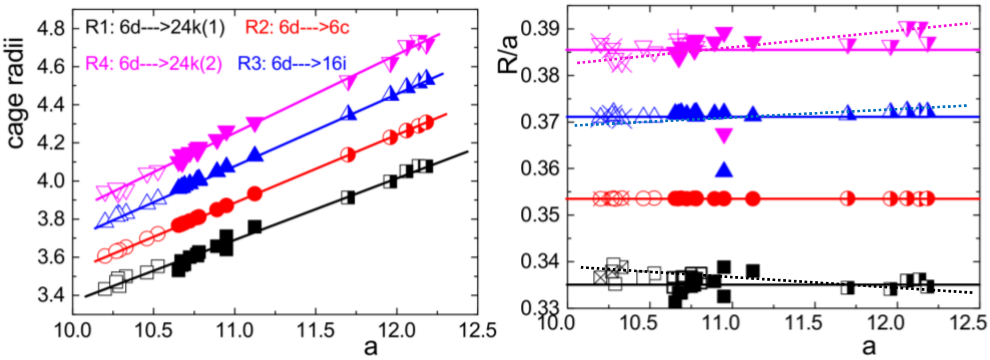

Figure 1.8: The radii of a tetrakaidecahedral cage. The data comes from inorganic crystal structure data base (FindIt). Left: four different radii as scaled by their lattice constants. Right: the ratio of cage radii and their lattice constants as a function of their lattice constants. Legend: empty symbols represent Si-clathrate, filled symbols represent Ge-clathrate and half-filled symbols represent Sn-clathrate; the empty symbols with cross inside are those compounds with the same Si-framework but different guest atoms. Lines are guides for the eyes.

As shown in Figure 1.8, the cage radii increase consistently with the increase of their lattice constants as a result of the similarity of different clathrates. However distortions can be observed on $16i$ and $24k$ sites for different clathrates as shown by the R/a values in Figure 1.8. This is consistent with Table 1.1 that only $6c$ host sites are fixed. There are two comments regarding the R/a values: (1) For clathrates with the same framework (Si-, Ge- or Sn-framework indicated by empty, filled or half-filled symbols, respectively), an enhancement in the size of a guest atom will result in an enhancement in a and a consistent enhancement in $R2$ and $R3$, but R1 increases faster while R4 increases slower. This situation is shown by the symbols with crosses inside for Na_8Si_{46}, K_8Si_{46} and Ba_8Si_{46}. It means that large guest atoms tend to make the tetrakaidecahedral framework a ball, while small guests tend to make the the framework an ellipsoid. This situation can also be found in $Ba_8Ga_{16}Ge_{30}$, $Sr_8Ga_{16}Ge_{30}$ and $Eu_8Ga_{16}Ge_{30}$. (2) As for clathrates with different frameworks (Si-, Ge- or Sn-framework), an enhancement in the size of host atoms will result in an enhancement in a and a consistent enhancement in $R2$; but different from the situation (1), R1 increases slower while R4 and R3 increase faster as indicated by the dotted line. This situation can be found by comparing $Ba_8Ga_{16}Si_{30}$, $Ba_8Ga_{16}Ge_{30}$ and $Ba_8Ga_{16}Sn_{30}$. It means that large host atoms tend to make the framework an ellipsoid while small host atoms tend to make the framework a ball. In summary, large free space inside tetrakaidecahedral cages tends give even larger freedom in the direction parallel to the hexagon faces than in the direction perpendicular to the hexagon faces. Therefore given large free space, guest-off-center behavior might appear in the plane parallel to the hexagon rings (As one shall see in chapter 3, guest-host interaction is also quite important).

Site Occupancy

In ternary clathrates or binary clathrate with vacancies, the host atoms were initially believed randomly distributed over the three host sites, so early studies were mostly emphasized on guest atoms [54]. However some early researchers have already pointed out a preferential occupancy of gallium in $G_8Ga_{16}Ge_{30}$ [55], and recent researches revealed that site occupancy factors play a crucial role in understanding the properties of both host-atoms and guest-atoms [51, 53, 56]. The following description of site occupancy factors by focusing on trivalent elements substituted ternary clathrates is mainly based on the report given by B. B. Iversen, *et al.* [53]. Theoretic calculations made by Blake *et al.* [57] have pointed out that bonds between trivalent elements are energetically not favored. Therefore the maximum trivalent element site occupancy factor (f(III)) can be derived. According to Figure 1.7, there are five restraints, which can be deduced from the bonding characters as we mentioned earlier: (1) $f(\text{III}) \leq 100\%$ at $6c$ sites. $6c$-site atoms can be fully substituted, since there is no direct bond between any two $6c$ atoms. (2) $f(\text{III}) \leq 50\%$ at $16i$ sites. Only half sites can be filled by trivalent element to avoid unfavorable III-III bonds. (3) $f(\text{III}) \leq 50\%$ at $24k$ sites. (4) $f(\text{III}) \leq 100\%$ at $6c$ and $24k$ sites. The sum of the trivalent element occupancies at $6c$ site and $24k$ site should not be more than 100%. (5) $f(\text{III}) \leq 50\%$ at $16i$ and $24k$ sites. These rules give the largest achievable trivalent element content 15, calculated from a structure with 50% occupancy at the $24k$ and $6c$ sites ($3+12=15$). In another word, the avoidance of energetically disfavored III-III bonds gives a different conclusion from Zintl concept which suggests 16 trivalent atoms per unit cell. The confliction may give us a hint to understand why few p type trivalent clathrates have been reported (III-III bond is not favored). Site occupancy factors can be obtained by analysing single-crystal X-ray or neutron diffraction data.

Disorder of Atoms

The atomic disorder in type-I clathrate can be found at both host sites and guest sites. The host disorder is ascribed to the different site occupancy factors of different elements as well as vacancies. While the guest disorder was ignored at beginning and it has been believed that guest atoms are ordered and precisely occupy the on-center positions of cages, until 2000, when Chakoumakos *et al.* pointed out the off-center behavior of Sr atoms inside the tetrakaidecahedral cages of $Sr_8Ga_{16}Ge_{30}$ [54]. The refinement of the single crystal neutron diffraction data revealed the splitting of a 6d-guest site into four 24k-guest sites. The typical compounds showing strong disorder of guest atoms are $G_8Ga_{16}Ge_{30}$ (G = Sr and Eu) and $Ba_8Ga_{16}Sn_{30}$ with off-center displacements of 0.3 Å, 0.40 Å and 0.43 Å, respectively [41, 58]. The disorder of atoms is closely associated with anharmonicity in phonons as well as tunneling states, which will be discussed in details in chapter 4.

General Physical Properties

Thermoelectric properties of intermetallic clathrates have been introduced earlier. The good thermoelectric performance of type-I clathrates is mainly due to the PGEC character of the compounds. Take $Ba_8Ga_{16}Ge_{30}$ (BGG) and $Sr_8Ga_{16}Ge_{30}$ (SGG) as exemples, the PGEC character is shown in Figure 1.9. The low electrical conductivity can be realized by tuning carrier concentrations, while the low thermal conductivity is intrinsic and is mainly determined by the rattling phonons of guest atoms. The characters and important roles of rattling phonons will be described in the next section.

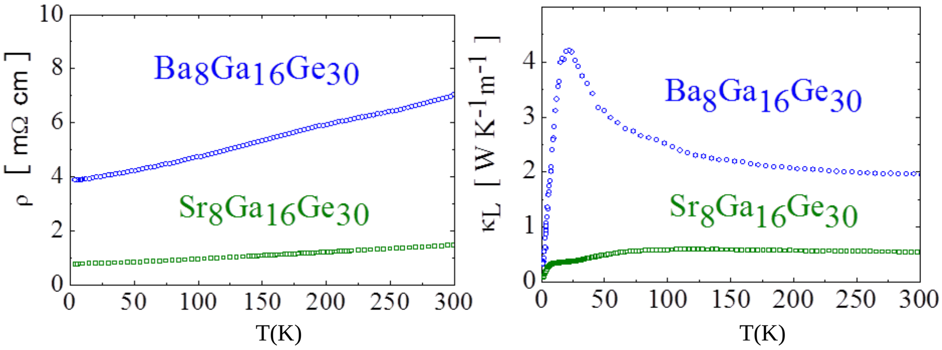

FIGURE 1.9: Illustration of the PGEC character in type-I clathrates: indicated by the low thermal conductivity and low electrical resistivity.

Type-I clathrates are also of great interest for their **superconductivity** behavior [59, 60]. Good superconductors can generally be found in binary clathrates, and the introduction of a third element would lead to a quick disappearance of the superconducting behavior due to the influence of the atomic disorder. It has been suggested that the coupling between rattling phonons and conduction electrons plays the critical role for having superconductivity in type-I clathrates [60, 61].

The **unusual large diamagnetism** in type-I clathrates is interesting as well[62], because it is easy for researchers to recall the ring current story in fullerene [63]. The diamagnetism will be discussed in chapter 6.

1.4 Rattling phonons in materials with cage structures

Rattling phonons are scientifically important for on one hand coupling with conduction electrons, which gives rise to an effective mass enhancement of conduction electrons or superconductivity of conduction electrons [61], on the other hand coupling with propagative phonons, which leads to an enhancement of scattering probability and low thermal conductivity [19, 64]. The role of rattling phonons playing in lowering thermal conductivity is specifically interesting and has been widely and deeply studied in the thermoelectric society. However the phonon scattering mechanism is still not clear and under debate [15, 19, 64, 65]. We will give a brief review of rattling phonons here.

1.4.1 Definition of Rattling

The rattling phenomenon might be first described by A. J. Sievers and S. Takeno [66] in 1965, when they observed a sharp vibration energy peak of Li in KBr:LiBr at low frequencies. The Li atoms occupy K sites but weakly interact with their surrounding atoms and therefore vibrate differently, leading to a phonon peak distinct from the background phonon spectrum. Then W. A. Harrison introduced the rattling concept for Li atoms in his book "Solid State Theory" [67]. The rattling behavior has been universally observed in materials with cage structures, such as $Al_{10}V$-type intermetallide [68], brownmillerite [69], skutterudite [70], pyrochlore [71] and clathrate [19, 72]. Different from the Li-rattlers, the rattlers (guest atoms) in cage compounds are included in a periodic array of cages and can be quantitatively studied.

So far, there is no precise definition of "rattling", and the following description is mainly based on Z. Hiroi *et al.* [61]. As shown in Figure 1.10, a rattler is defined as a local atom, which is weak bonded with the surrounding cage atoms, in another word, it has free space to move, and rattling is therefore defined as a local, anharmonic vibration of a rattler. The interaction between closely packed atoms can be described by parabolic potentials, indicating harmonic vibrations of the atoms. Therefore cages atoms (blue in fig. 1.10) and guest atoms in very small cages (green in fig. 1.10) can be classified as harmonic oscillators. However in an oversized cage, the guest atom (orange in fig. 1.10) vibrates as a rattler, which interact with cage atoms via an anharmonic or quasi-harmonic potential as shown in Figure 1.10. There are generally two characters of a rattler: low vibration frequency and large atomic displacement parameter, in consequence

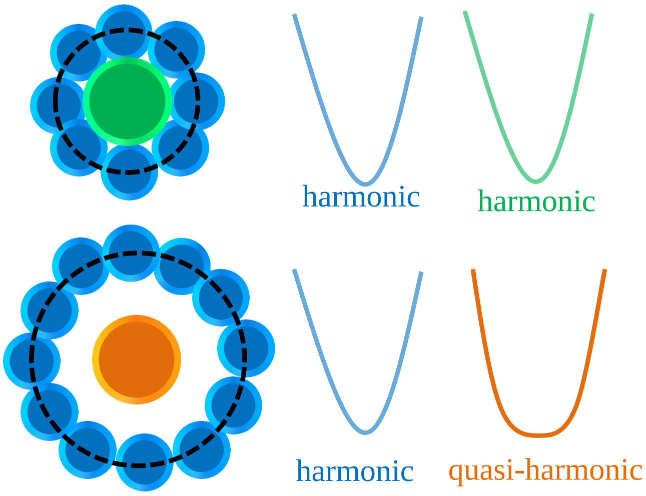

FIGURE 1.10: Schematic illustration of rattling vibrations in cage compounds. Cage atoms and their corresponding potentials are painted with blue color, and guest atoms in big cages and small cages and their corresponding potentials are painted with orange and green colors, respectively. In the small cage, the guest atom and cage atoms are closely packed so that there is no free space inside the cage; while in the big cage, there is a considerable free space so that the guest atom vibrates like a rattler.

of weak bonding environment and large free space of a rattler. In spite of the anharmonicity, rattling can be normally described by a harmonic approximation with the Einstein model, where each rattler is treated as an Einstein oscillator with a characteristic energy ω_E. It should be noted that, for off-centered guest-atoms, the anharmonicity of rattling is even stronger and beyond the description of the harmonic approximation. Although Z. Hiroi *et al.* [61] pointed out that the off-centered guest modes are not rattling modes but "soft modes", many researchers indeed applied "rattling" for the off-centered vibrations [73] and anharmonic models have been introduced to interpret the off-centered rattling [41].

1.4.2 Experimental method

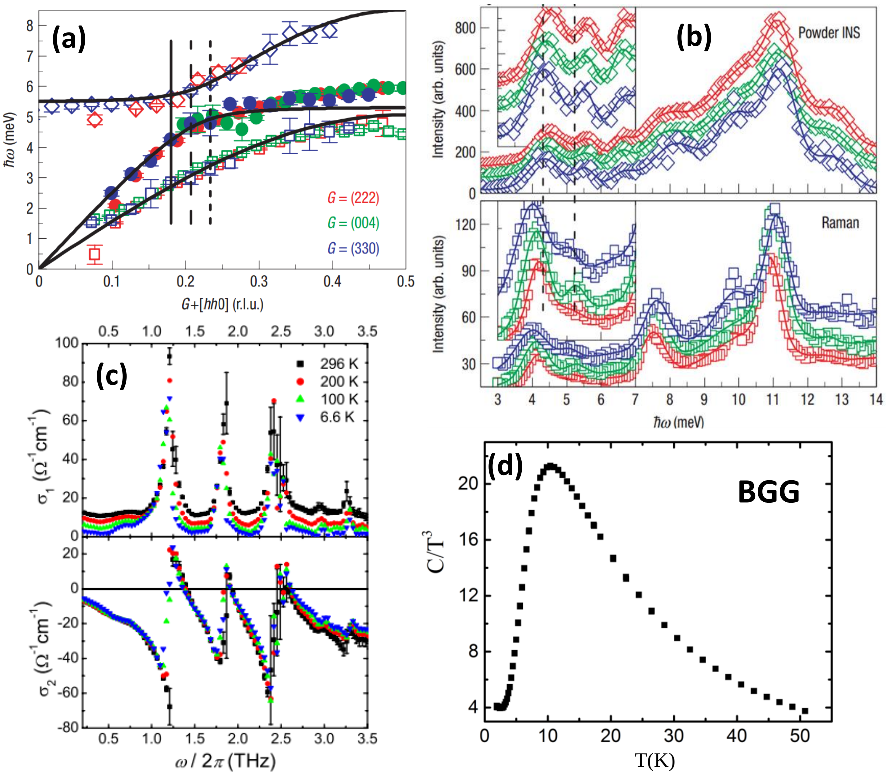

Figure 1.11: Experiment method for detecting rattling phonons in type-I clathrates (take n-type-$Ba_8Ga_{16}Ge_{30}$ as an example). (a) Phonon dispersion relations derived by single-crystal inelastic neutron scattering (INS) measurement [19]. (b) PDOS and raman spectrum derived by powder INS measurement and raman spectroscopy measurement, respectively [19]. (c) Optical conductivity spectrum [74]. (d) Heat capacity (C), plotted as C/T^3 vs. T.

First of all, rattling phonons can be directly observed in phonon dispersion relations, based on inelastic neutron scattering measurement. Figure 1.11 (a) shows the phonon dispersion relations of n-type-$Ba_8Ga_{16}Ge_{30}$ (n-BGG) [19], where the rattling phonon branch avoid crossing the acoustic branches at around 5 meV. Based on the phonon dispersion relations, the low energy excitation of rattling phonons can indeed be described by the Einstein model and shall give rise to a "boson-like peak" in phonon spectrum like in glass system. Figure 1.11 (b), (c), (d) show the boson peaks, appearing in phonon density of states (PDOS), raman spectrum, optical conductivity and heat capacity, respectively for n-BGG [19, 74].

Since this dissertation will focus on heat capacity studies, I would like to introduce more about rattling phonons in heat capacity. According to the Einstein model, the rattling-PDOS($D_R(\omega)$) can be expressed as,

$$D_R(\omega) \;=\; \delta(\omega - \omega_E) \tag{1.18}$$

where ω is the oscillation frequency. The heat capacity of rattlers(C_R) can then be derived as,

$$\begin{aligned} C_R \;&=\; k_\mathrm{B} \int \mathrm{d}\omega \, D_R(\omega) \frac{x^2 e^x}{(e^x - 1)^2} \\ &=\; 3N \, k_\mathrm{B} \, \frac{x_E^2 \, e^{x_E}}{(e^{x_E} - 1)^2} \end{aligned} \tag{1.19}$$

where N is the number of rattlers, k_B is the Boltzmann constant and x can be defined as $x \equiv \hbar\omega/k_B T$, with the following notation, $\hbar$: the reduced Plank constant, T: temperature. x_E is expressed as $x_E = \hbar\omega_E/k_B T$. The rattling heat capacity is shown in Figure 1.12, where there are three prominent characters of the peaks. (1) The intensity of boson peaks decreases very fast as the characteristic energy (ω_E or θ_E) increases. (2) Boson peak in heat capacity is very sharp at extremely low ω_E and gradually becomes broad at elevated ω_E. (3) The peak temperature (T_{peak}) is related with θ_E by: $\theta_E \;\approx\; 4.93 T_{peak}$. More details of boson peaks will be given in chapter 3. It is noted that in actual materials, contributions from conduction electrons and Debye phonons should also be taken into account. In addition, in the case of off-center rattlers, tunneling states can be observed in heat capacity as well (chapter 4) [75, 76].

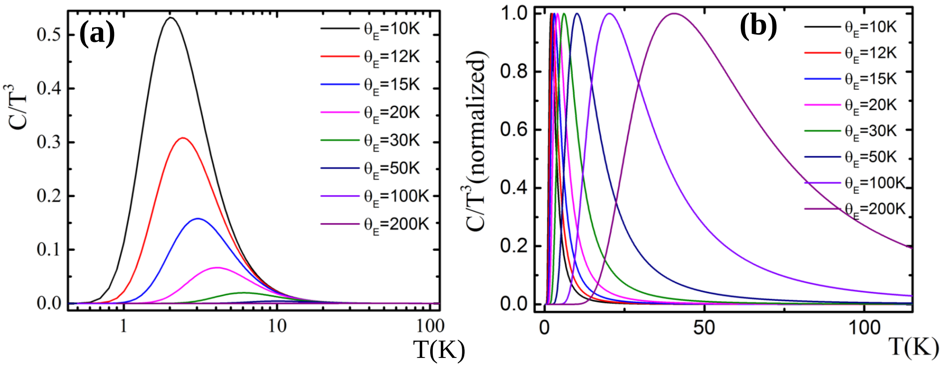

FIGURE 1.12: Heat capacity of rattlers with different characteristic energies θ_E. (a) Boson peaks appearing in the C/T^3 vs. T plot. (b) Boson peaks after adjusting peak-height.

Recently, a new concept–”part-crystalline part-liquid state” has been proposed for thermoelectric energy harvesting [23, 77, 78]. According to this concept, it seems that one alternative way to improve thermoelectric performance is to introduce two or more different structures in one material, where there are at least one strong structure for lattice stability as well as high electrical conductivity and a weak one for low thermal conductivity. Compounds with rattling phonons can be one of the candidates, because the rattler with big ADP values can be regarded as a liquid-like weak structure, which attaches on the strong cage structures. Therefore rattling phonons should be quite important for thermoelectric materials design.

1.5 Purpose and organization of the thesis

This dissertation is aimed at a fundamental study on rattling phonons and the associated thermal and electrical properties in type-I clathrates. We hope the present work serves as an intrinsic understanding of rattling phonons and thus provides guidelines for thermoelectric materials design. In order to achieve this purpose, the dissertation is organized in seven chapters as follows.

Chapter 1 is the introduction of the research background (thermoelectricity), the materials (type-I clathrate) and the physical phenomenon (Rattling) of interest. **Chapter 2** is experimental method, which contains materials syntheses, material characterizations and physical properties measurements. Some analytical methods will also be included in this chapter.

In **chapter 3**, a systematic study on boson peaks appearing in heat capacity at intermediate temperatures (20 K-100 K) in type-I clathrates will be given. It will be shown that all boson peaks could be rationalized in terms of a single unified exponential line for a variety of clathrates by employing a new parameter associated with the freedom of space. The interactions between a rattler and its surrounding atoms (strong covalent structures) are basically van der Waals type weak interactions. The conclusion provides guidelines for understanding the origin of boson peaks in glass system as well as thermoelectric materials design from the view point of rattling phonons.

In **chapter 4**, a systematic study of off-centered rattling indicated by tunneling states at extremely low temperatures (below 1 K) will be given. Tunneling states, which was proposed for glass materials [79], are observed in off-centered clathrate system as well. It will be shown that The low-T linear terms of heat capacity, including the tunneling term and the Sommerfeld itinerant-electron term, are successfully separated through careful measurements of single crystals with various carrier concentrations. The influences of tunneling states to thermal conductivity as well as the effective mass of conduction carriers will be discussed on a basis of the experiment data.

In **chapter 5**, thermal and electrical properties will be studied for nobel metal doped type-I clathrates: $Ba_8M_xGe_{46-x}$ (M = Cu, Ag, Au). The single crystals grown from Sn-flux have high electron mobilities, and their thermoelectric performance will be discussed on a basis of the carrier concentrations and mobilities. **Chapter 6** describes the anomalous diamagnetism in type-I clathrates. Possible reasons of the unusually large diamagnetism, including ring current, structure diamagnetism and imbalanced Langevin diamagnetism and Van Vleck paramagnetism will be discussed on a basis of experimental data.

Chapter 7 concludes the dissertation.

Chapter 2

Experiment Method

This chapter describes the experiment method applied in the present research, and it includes materials syntheses, characterization and physical properties measurements.

2.1 Materials syntheses

Material synthesis is the starting point of materials science, because the quality a compound directly determines the quality of a research. For solid-state crystalline materials, there are several approaches to synthesize a compound, depending on whether it is a poly-crystal or single crystal. The most easy and practical way to prepare a poly-crystalline compound is simple mixing and melting by using a radio-frequency (RF) induction furnace, box furnace or many other types of furnaces. Except for some oxides, the crystal growth generally requires an oxygen-free environment. Single crystal is much more difficult to be prepared, as it is not simple mixing but like building a house, which requires a step by step process along a certain direction. The most common methods for growing single crystals are: flux-growth method, Bridgeman method, Czochralski method, floating-zone method, etc. In our experiment, poly-crystalline clathrates are grown by using a RF-induction furnace [80–82] and single crystals are mainly grown by flux methods [41, 75, 76, 83, 84]. The growth techniques are described as follows.

2.1.1 Poly-crystal syntheses using RF-induction furnace

The great idea of the RF-induction furnace is that it heats an electrical conductor (commonly a metal) by using electromagnetic induction. When an alternating current (AC) goes through an electromagnetic coil, the electric energy will be converted to electromagnetic energy. If an electrically conducting object is put inside the coil, the electromagnetic field then induces an electric current inside the object, and consequently the object will be heated by Joule heating. Figure 2.1 shows an electromagnetic coil and a copper crucible inside the coil. In order to avoid a damage to the crucible, cooling water flows around the system. The crucible chamber is filled with argon gas so as to create an oxygen free environment for crystal growth.

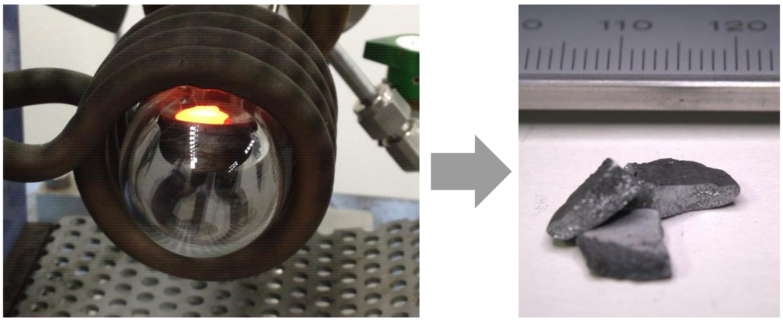

Figure 2.1: Synthesis of a poly-crystal by using a RF-induction furnace.

The process for preparing poly-crystalline clathrates is like this: First, stoichiometric amount of the elements is prepared in a glove box, where oxygen and moisture is limited to 0.1 ppm and 0.5 ppm, respectively (ppm: parts per million). Then the mixed elements are heated and fused in the crucible as shown in fig. 2.1. The melting and boiling state of the mixed elements is kept for several minutes and then the system is gradually cooled down by decreasing the applied current. The heating-cooling process is repeated for at least three time in order to achieve a homogenous compound (one grown compound is shown on the right side of fig. 2.1).

The advantages of RF-induction furnace are: (1) A metal with very high melting point might be melted by using this furnace. (2) One synthesis only takes a short time, so it is an efficient way to explore new compounds. (3) Component ratio of different elements can be easily modified, therefore it is a useful method to prepare different alloys. However, RF-induction furnace can not be applied for melting insulators or some semiconductors as the Joule heating in these materials is rather weak. It is impracticable for elements with low boiling points either, because they will evaporate and their amount decreases. For ferromagnetic elements in powder or small grains, it should be careful to use a RF induction furnace, because these elements might be pulled out from the crucible by an electromagnetic force.

2.1.2 Single crystal growth using flux method

Comparing to poly-crystals, which have a lot of grain boundaries, a single crystal has a perfect lattice structure continuously until the edge of the sample. Therefore it provides the intrinsic properties of a compound and has been applied for fundamental studies in condensed matter physics. Flux-growth is an easy but efficient way to grow single crystals, since no special device is required: a box furnace with temperature and time setting is enough.

The term “flux-method” describes the growth of a crystal out of a flux, which is similar to the growth of a crystal out of a water solution. The lower right corner of fig. 2.2 sketches the growth situation, where a crystal (blue) separates from a flux (pink) inside a sealed quartz tube. There are generally two types of fluxes: one is metal applied for the growth of a semiconductor, the other one is oxide or halogenide applied for the growth of a ionic material. A material selected as a flux should have a relatively low melting point but high boiling point, so that the flux can be in liquid state for a wide temperature range, which is good for crystal growth as well as the separation of a grown crystal and the remained flux. In addition, a flux should not react with or substitute constituent elements drastically, except that the flux itself is one of the components of the target compounds, and the latter flux is called self-flux.

In our experiment, Ga, In, Sn, Al, Zn and Bi are applied as fluxes for growing single crystals of type-I clathrate. Among them, Ga, In, Sn, Zn and Al are applied as self-fluxes to grow $Ba_8Ga_{16}Ge_{30}$ (BGG), $Sr_8Ga_{16}Ge_{30}$ (SGG), $Eu_8Ga_{16}Ge_{30}$ (EGG), $Ba_8In_{16}Ge_{30}$ (BIG), $Ba_8Ga_{16}Sn_{30}$ (BGSn), $K_8Ga_8Sn_{38}$ (KGSn), $Ba_8Zn_8Ge_{38}$ (BZG) and $Ba_8Al_{16}Ge_{30}$ (BAlG) single crystals. In-, Sn-, and Bi-flux are used to grow $Ba_8Cu_xGe_{46}$ (BCG) single crystals, but the framework atoms are partially substituted by the flux atoms (around 1 atom per unit cell) except for Bi. More information about metallic flux growth can be found in Ref. [85], and the growth of a specific compound will be described with more details in each chapter on request. Here I would like to show a brief outline of the flux-growth in our laboratory.

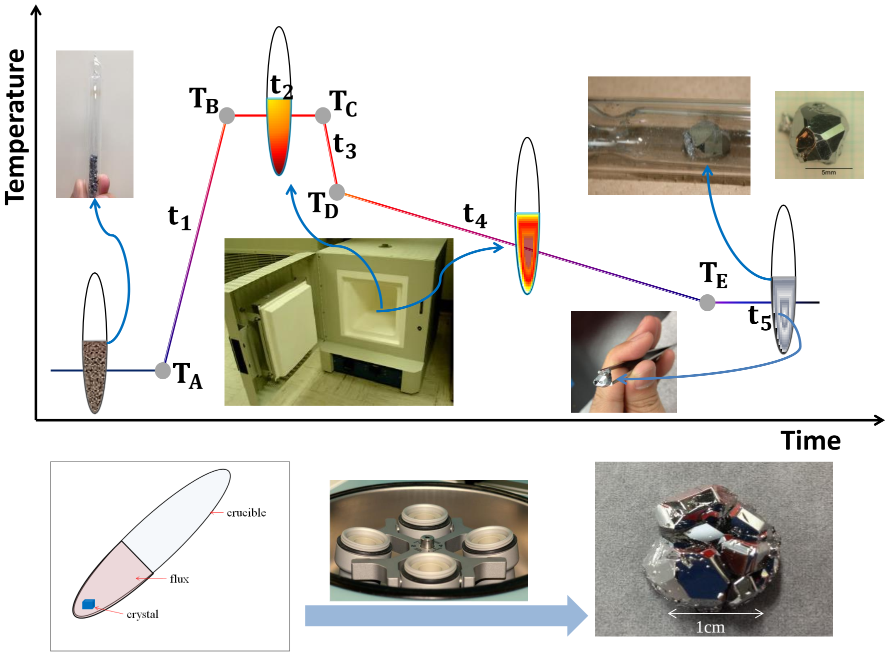

FIGURE 2.2: The syntheses process of clathrate single crystals by using flux-method.

The flux-growth process is shown in fig. 2.2. Firstly, fluxes and stoichiometric amount of elements are sealed in a crucible made from quartz or alumina. The preparation of the elements is made inside a glove box, as described earlier, and the quartz tube is sealed with argon gas or vacuum inside. It should be noted that sealing a quartz tube with vacuum inside is very difficult due to the pressure difference inside and outside the tube. In addition, a neck is usually made on the tube for separating a grown crystal from the fluxes (fig. 2.2).

Secondly, the sealed tube is heated inside a box furnace following a specially designed temperature sequence. The temperature sequence normally have five steps: from t_1 to t_5. (1) t_1 step: The temperature is fast increased to the highest point T_B. Generally speaking, T_B should be a temperature above the melting point of any element inside the tube, however T_B can be lower with the help of the large amount of fluxes. Take type-VIII BGSn as an example, a T_B, equals to 770 K, is much lower than the melting point of Ba. (2) t_2 step: The highest temperature is kept (which means $T_B = T_C$) for several hours for a homogenous mixing of the elements. It shall not take too long time in this step, because the chemical reaction between active elements and the crucible would cause a damage to the crucible and a serious loss of the elements. (3) t_3 step: The temperature is fast cooled down to T_D, which is still above the melting point of the target compound. It takes a short time for the same reason as in the step t_2. (4) t_4 step: The system is cooled down slowly until T_E, which is below the melting point of the target compound. The single crystal is growing during this step, so a slow cooling rate is quite necessary (usually 2 °C/hour). (5) t_5 step: T_E is kept for one day or two days for annealing and centrifugation. The growing processes of different type-I clathrates are summarized in table 2.1.

TABLE 2.1: Growing process of clathrate-I single crystals by using flux method. The unit of temperature is °C, and the unit of time is h. In the flux column, the number in the parentheses is the amount of flux, measured by the number of atoms in one unit cell.

sample	Flux	T_A	t_1	T_B	t_2	T_C	t_3	T_D	t_4	T_E	t_5
BGSn-VIII	Sn(40)	RT	10	490	10	490	-	-	100	390	50
BGSn-I	Sn(40)	RT	10	900	5	900	2	600	100	400	50
KGSn	Sn(40)	RT	10	550	8	550	-	-	100	450	50
BGG	Ga(38)	RT	10	1150	5	1150	5	980	100	680	50
SGG	Ga(38)	RT	10	1150	5	1150	5	780	100	550	50
BZG	Zn(15)	RT	10	1150	6	1150	2	980	100	600	50
BCG-In	In(30)	RT	10	1150	5	1150	5	920	100	650	50
BCG-Sn	Sn(20)	RT	10	1150	5	1150	5	920	100	650	50
BCG-Bi	Bi(20)	RT	10	1150	5	1150	5	920	100	650	50

After the five steps, the grown single crystal are separated from the remained flux by using a centrifugal machine as shown in fig. 2.2. Usually, it is necessary to make a further cleaning on the crystal surface in order to remove the flux completely. The cleaning methods include a mechanical cutting or polishing and a chemical reaction by washing the sample in a diluted hydrochloric acid. More cleaning methods can be found in Ref. [85].

2.2 X-ray diffraction measurements

X-rays have become a powerful tool for detecting the structure of a crystal, since the X-ray diffraction theory was established by Bragg and Laue [86]. According to Bragg's description, a parallel X-ray beam can be reflected by lattice planes of a crystal as shown in Figure 2.3. The reflected X-rays interfere with each other, and only under constructive interferences, reflection spots can be observed in the diffraction image. Bragg summarized the constructive interference conditions by using an equation, which is later called Bragg's law, as shown below:

$$2d\,sin\theta = n\lambda \tag{2.1}$$

where λ is the wavelength of the X-ray, θ is the incidence angle (also called the Bragg angle) with respect to the lattice planes, n is an integer and d is the interplanar distance. It should be noted that the reflection plane, which is determined by the array of atoms in a lattice, is not associated with the crystal surface. According to Bragg's law, diffraction spots are observed depending on d,

θ and n. However, d and n are not experimental parameters, and actually their influences to diffraction spots can be reflected in θ, therefore experimentally, θ is used to scale a diffraction pattern as shown in Figure 2.3.

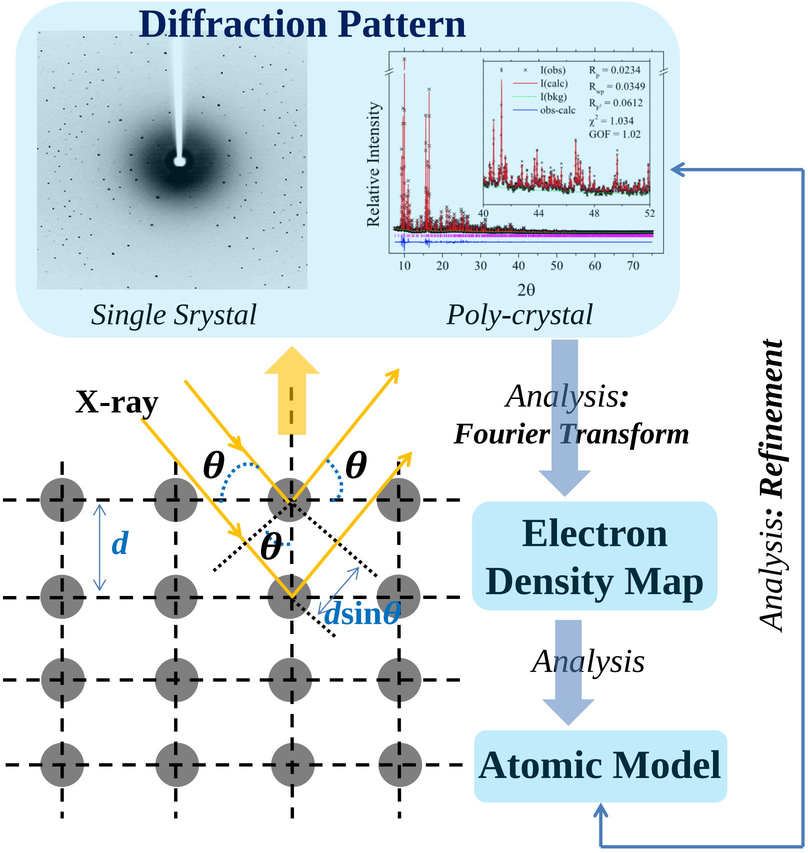

FIGURE 2.3: A schematic for deriving Bragg's equation and the data-analyses process of a X-ray diffraction measurement.

Fourier analysis shows that diffraction spots, which are defined as the so called reciprocal lattice, are related to the real lattice through a Fourier transform. Therefore from a diffraction image, a corresponding electron density map can be derived via Fourier analyses. Then an atomic model can be constructed based on the electron-density distributions. The last step is parameters refinement by comparing the atomic model and the diffraction pattern. Both lattice structure and crystal quality can be obtained in the last step. The data processing procedure is shown in Figure 2.3.

2.2.1 Powder diffraction measurement and analyses

Powder X-ray diffraction (XPRD) measurements are applied for poly-crystals and the powder of single crystals. A diffraction pattern is shown in Figure 2.3 where the intensity is plotted as a function of 2θ. Our experiments were carried out by using the large Debye-Scherrer camera with an imaging plate detector at the BL02B2 beam port of the synchrotron radiation facility at SPring-8. The wavelength of the synchrotron X-ray can be tuned and determined by using a CeO_2 standard, and the applied wavelength was around 0.5 Å. ϕ 0.2 mm glass capillaries, inside which, fine powders were mounted, were used for recording X-ray diffraction patterns. Some of our XPRD experiments were also executed by using a lab facility: Rigaku RINT 2500/PC with the graphite-monochromatized Cu Kα X-ray beams. The Rietveld method within the GSAS package [87, 88] was applied for data analyses.

2.2.2 Single crystal diffraction measurement and analyses

Comparing to XPRD, single crystal X-ray diffraction (SCXRD) is a more powerful tool to determine a crystal structure and indispensable for studying a single crystal. A SCXRD pattern is shown in Figure 2.3, where many diffraction spots can be observed. Some of our single crystal samples were checked at the BL02B1 beam port of the synchrotron radiation facility at SPring-8, while the other samples were checked by a Rigaku R-AXIS single-crystal diffractometer using MoK α radiation.

In the synchrotron radiation facility, the X-ray wavelengths were calibrated to be around 0.35 Å, and the experiments were conducted at 20 K (the lowest achievable temperature in the system) by applying a continuous cryogenic He-flow (XR-HR10K-S, Japan Thermal Engineering Co. Ltd.). A Small single crystal with 10-100 μm in size was picked out and mounted on the top of a sharp glass needle. While in a lab facility (Rigaku), the X-ray wavelength is 0.71075 (MoK α) and the experiments were conducted at room temperature (RT). The sample size is usually larger than 100 μm and can be even more than 300 μm. Nine frames of diffraction images were taken with the oscillation angle (ω) of 10° in each frame. So, in total, it is 90°, which is sufficient for a type-I clathrate with a cubic symmetry structure. Crystal structures were refined by employing a full-matrix least-squares method with WinGX program package [89].

2.3 SEM-EDS characterization

The quality and chemical composition of our samples were checked by Scanning Electron Microscopy with Energy Dispersive X-ray Spectroscopy (SEM/EDS: JEOL, JSM-7800F / Oxford Instruments, X-Max SDD Detector). This is how it works: Electron beams with a energy of 5 keV or 10 keV are applied to polished surfaces or as-grown surfaces of a grown crystal, an inner shell electron of the component elements might be excited and a hole, where the electron was, might be created. An outer shell electron with higher energy may come to occupy the hole, and an characteristic X-ray will be generated. Since the characteristic X-rays of different elements are different, the chemical component of a compound can be determined from the spectroscopy, and the composition ratio can be derived from the spectrum intensity. An example of the EDS spectrum of the $Ba_8Ag_{5.3}Ge_{40.7}$ (BAG) compound grown from Sn-flux is shown in Figure 2.4. According to the spectrum shown in the figure, the formula of the BAG compound is derived to be $Ba_8Ag_{5.0}Ge_{39.5}Sn_{1.1}$, and more detailed discussion on BAG compounds will be given in chapter 5.

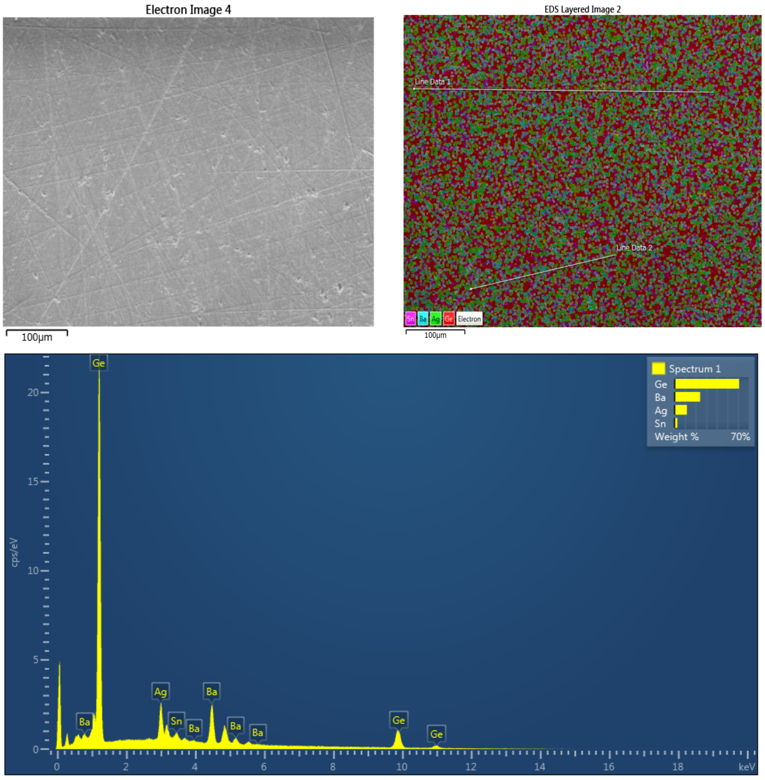

FIGURE 2.4: The SEM image and EDS spectrum of a BAG compound grown from Sn-flux.

2.4 Physical properties measurement

Thermal and electrical properties are mainly measured by using a physical properties measurement system (PPMS: Quantum Design) and magnetic properties are mainly measured by using a Quantum Design superconducting quantum interference device (SQUID: Quantum Design).

2.4.1 Heat capacity measurement

The heat capacity of a compound is defined as,

$$C \equiv \frac{\triangle Q}{\triangle T} \tag{2.2}$$

where $\triangle Q$ is the heat change (absorption or release) and $\triangle T$ is the corresponding temperature change. The measurement method is schematically shown in fig. 2.5 (a), where the whole system is in vacuum. The temperature is measured by the thermometer and the heat source is provided by the heater, which can be controlled as on or off so as to derive the heat change of the system. Usually, the addenda including the platform and grease is measured first, and then the addenda and a sample is measured. The heat capacity of the sample can be obtained by subtracting the first measurement result from the second measurement result.

In actual experiment, selected samples were cut into small pieces with masses from 5 to 30 mg. The size of the samples was made as small as possible to ensure a better homogeneity and the

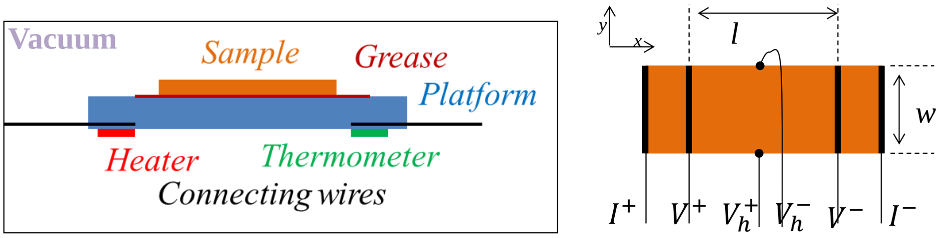

(a) *Heat Capacity Measurement*

(b) *Resistivity and Hall measurement*

FIGURE 2.5: The sketched maps for heat capacity, resistivity and Hall resistivity measurements.

amount of grease was also controlled to be as small as possible so that the background signal could be minimized. The measurements were carried out from 0.36 K to RT by using PPMS equipped with a ^{3}He cryostat.

2.4.2 Resistivity measurement

The electrical resistance of a compound with a regular shape is normally related to the resistivity of the compound by the following relationship:

$$R = \rho \frac{l}{A} = \rho \frac{l}{w \times d} \tag{2.3}$$

where R is the resistance, ρ is the resistivity, l is the length as shown in fig. 2.5, A is the cross section area, w is the sample width as shown in fig. 2.5 and d is the sample thickness. According to Ohm's law, $R = V/I$, where V is the voltage and I is the current. Therefore the resistivity is expressed as:

$$\rho = \frac{V}{I} \frac{A}{l} \tag{2.4}$$

In our experiment, the four probe method is applied as shown in Figure 2.5 (b). The electric current I is applied from I^+ to I^-, and the voltage is measured from V^+ to V^-. In order to minimize the contact resistance, one need to be careful to make electrodes. In our case, gold paste and gold wires were used for making electrodes on the sample surface. The measurements were carrier out from 2 K to 300 K.

2.4.3 Hall resistivity measurement

Hall resistivity measurement is a powerful method to detect the carrier type and carrier density of a compound. According to Figure 2.5, an electric current is applied from I^+ to I^-, and a voltmeter is connected between V_h^+ and V_h^- (V^+ and V^- are vacant now). If a magnetic field which is perpendicular to the sample surface is applied, an additional Lorentz force will be exerted to the conduction electrons/holes. The carriers tend to move to the side until another electric field along y direction is formed and large enough to balance the Lorentz force. According to the balance condition, the Hall coefficient (or Hall resistivity) can be defined as:

$$R_H = \frac{E_y}{j_x B} \tag{2.5}$$

where E_y is the electric field along the y direction, B is the applied magnetic field and j_x is the current density along the x direction. The formula can be modified to be experimental parameters related:

$$R_H = \frac{U_y d}{I_x B} = \frac{R_{yx} d}{B} \tag{2.6}$$

where U_y is the voltage between V_h^+ and V_h^-, d is the thickness of the sample, I_x is the applied electric current and R_{yx} is the measurement resistance. It is easy to find that R_H is nothing but the slope of the linear function between $R_{yx}d$ and B. Then carrier concentrations can be derived as $n = -\frac{1}{R_H e}$.

In our experiment, the sample was polished to be less than 0.2 mm for achieving a high signal to noise ratio, and the measurements were carried out by a magnetic field scan under a fix temperature, ranging from 2 K to 300 K.

2.4.4 Thermoelectric properties measurement

The introduction of thermoelectric properties, including thermal conductivity, Seebeck coefficient and resistivity, can be found in chapter 1. The measurements were carrier out by using the thermal transport option (TTO) of PPMS from 2 K to 300 K. The sample was polished to be in a shape of cuboid, and both four probe method and two probe method were applied for measurements. In the four probe method, both thermal conductivity and electrical conductivity can be precisely obtained, but it is quite difficult to make electrodes. In the two probe method, it is easier to make strong electrodes, but the measurement for thermal conductivity and electrical conductivity is not accurate. The good news is that type-I clathrates are bad thermal conductors, so the influence from the thermal contact resistance is really small, especially at high temperatures; and the resistivity can be measured again by using the four probe method as described earlier. Therefore even two probe method can be well applied for measuring the thermoelectric properties of type-I clathrates.

2.4.5 Magnetic properties measurement

SQUID is a very sensitive magnetometer used to measure extremely subtle magnetic field based on superconducting loops containing Josephson junctions. In our experiment, both temperature (T) dependent magnetization and magnetic field (H) dependent magnetization were measured. In the T dependent measurement, a magnetic field of 5 T and 3 T was applied, respectively, from 2 K to 300 K. The magnetic susceptibility was derived by subtracting the result at 3 T from the result at 5 T, in order that the influence from ferromagnetic impurities can be canceled out. In the H dependent measurement, magnetic field is scanned from -7 T to 7 T at a fixed temperature, ranging from 2 K to 300 K. All the type-I clathrates show a weak diamagnetic susceptibility.

Chapter 3

A Systematic Study on ”Boson Peaks”

According to chapter 1, the rattling of guest atoms gives rise to two features in heat capacity: one is the low temperature excitation peaks, which will be discussed in this chapter, and the other one is the tunneling states of the guests, which will be discussed in the next chapter.

A Brief Abstract

Anharmonicity of phonons, apart from the conventional Einstein- or Debye- mode harmonic phonons, are frequently observed for amorphous or glass-like materials, and these phonon spectrum peaks are called boson peaks. A frontier topic relating to boson peaks revolves around the fact that they can be similarly observed in single crystals with a void of cage structure. Although the origin of the phonon anharmonicity associated with the boson peaks has been the center of scientific debate for many years, a clear understanding has not yet been achieved. In this chapter we show that all quasi-boson-peaks can be successfully rationalized in terms of a single unified exponential line for a variety of clathrates by employing a new parameter associated with the freedom of space. The intrinsic nature of the quasi-boson-peaks is described based on the unified picture with a help of first principles calculations. Although the origin of the boson peaks appearing in glass-like materials is complex to understand due to the missing information on the real structure, the understanding described in the present paper gives important information applicable to other systems. The van der Waals-type guest-host interactions discovered in the present study are consistent with the part-liquid concept and useful for thermoelectric materials design.

3.1 Introduction

Anomalous low energy excitations have frequently been observed in disordered systems including glass-like materials such as amorphous silica at terahertz (THz) frequencies by various experimental methods such as light absorption, x-ray scattering [90], inelastic neutron scattering [91]and Raman spectroscopy [92], dielectric relaxation experiments and heat capacity measurements [93]. These excitation peaks in the THz energy (in an energy level of around 50 K) are generally referred to as boson peaks. The boson peaks involve a certain kind of excess amount of low-energy excitations, and many intriguing physical properties have been reported in a disordered system. For instance, fracture toughness and hardness of materials are difficult to be simultaneously obtained in conventional materials, but such high strength materials can be realized in metallic glasses and reinforced-carbon matrix-composites [94]. The appearance of boson peaks is also known to be associated with anharmonicity in phonons, which presently becomes very important for realization of highly efficient thermoelectric materials [95]. The low-frequency modes observed by the boson peaks are fundamentally very different from those of the long-wavelength plane waves, and unusual phonon physics emerges with an anharmonic phonon density of states (PDOS) versus frequency ($D(\omega) \sim \omega$). A number of models have also been proposed to describe these boson peaks, such as the soft potential model [93], the disordered oscillator model and several others [96–98]. The boson peaks are scientifically intriguing, but their origin is still under debate and it is a priority areas for experimental and theoretical research. [90–98].

Recent front-line studies have focused on a fact that "boson-like peaks" can be observed even in single crystal materials having a cage structure containing endohedral atoms (or guest atoms), such as clathrates, pyrochlores, skutterudites, brownmillerites and $Al_{10}V$-type intermetallides [19, 68–71, 99] (they can be called quasi-boson-peaks). In contrast to the situation of glasses, these cage-structured materials are well categorized as single crystals with high symmetry and the explanation of the origin of the quasi-boson-peaks should be an important target for experimental and theoretical research. This kind of research approach should yield key experiments that provide clues for not only explaining long-lasting questions on the boson peaks associated with the anharmonicity of phonons, but also for obtaining a broader understanding for the nature of boson peaks in a glass-like disordered system. Among the many candidates of single crystal cage-compounds for yielding an intrinsic understanding of the boson peaks, clathrates are expected to be amongst the best, since a variety of cage structure types as well as many kinds of guest atoms from the periodic table starting from alkali metals (A), alkaline earth metals (E) and some rare-earth metals (R) can be synthesized, allowing for a range of free accommodation spaces inside the cages. A typical structure for type-I clathrates, the associated vibration modes of the guest atoms, and their corresponding quasi-boson-peaks in C_p are shown in Figure 3.1.

In order to elucidate the intrinsic nature of the quasi-boson peaks appearing in single crystal clathrates, we employ various approaches for interpretation of our experiments as well as other reported data. In the present report, we show that almost all scattered experimental data for the quasi-boson peaks can successfully be unified in terms of a well-correlated single universal line with an exponential function, by plotting their force constants as a function of a free space parameter newly introduced for the atoms accommodated inside the cage (R_free). The intrinsic nature of the boson peaks can be elucidated on a basis of this new unified relationship. The important interpretations are rationalized from the viewpoint of first principles calculations.

3.2 Experiment method

Single crystals of type-I clathrates, $Sr_8Ga_{16}Ge_{30}$ (SGG), $Ba_8Ga_{16}Ge_{30}$ (BGG), $Ba_8Zn_8Ge_{38}$ (BZG), $K_8Ga_8Sn_{38}$ (KGSn) and $Ba_8Ga_{16}Sn_{30}$ (BGSn), were synthesized by using a Ga, Sn or Zn flux method as introduced in chapter 2 and reported elsewhere [75, 76]. The quality of single

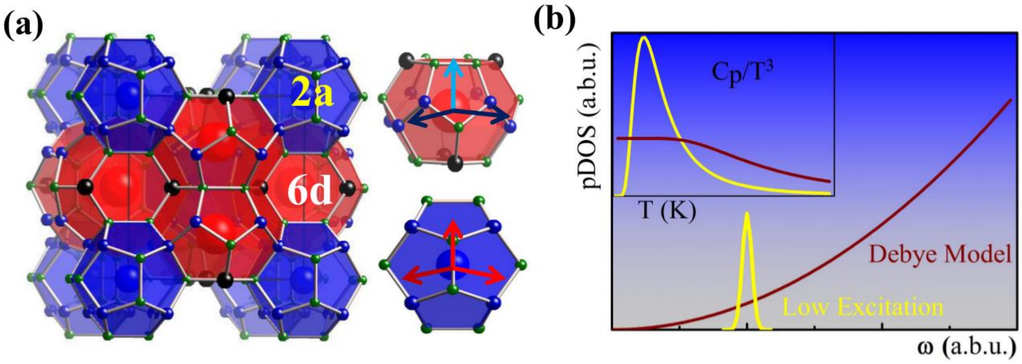

Figure 3.1: Quasi-boson peaks observed in heat capacity C_p for highly symmetric single crystals having a cage structure, where atoms are accommodated. (a) The crystal structure of type-I clathrates, which contains two kinds of cages: 2 dodecahedral (20-) (blue) and 6 tetrakaidecahedral (24-)(red) cages in a unit cell (the same as introduced in Figure 1.7). The vibration modes of guest atoms are schematically shown by arrows with different colors. Red arrows:the vibration modes for three different directions at the 2a site inside 20-cages, light blue arrows: vertical modes to a six-membered ring plane at the 6d sites inside a 24-cage, dark blue arrows: parallel modes to a six-membered ring plane at the 6d-sites inside a 24-cage. (b) A schematic conventional phonon DOS (Debye mode, red) including low energy excitations (yellow) and their corresponding heat capacities (C_p) expressed by $C_p/T^3 - T$ plot.

crystals were confirmed by single crystal X-ray diffraction and electron probe micro-analysis as described in chapter 2. Polycrystal compounds including, $\mathrm{Ba_8Cu_{5.3}Ge_{40.7}}$ (BCG), $\mathrm{Ba_8Ag_{5.3}Ge_{40.7}}$ (BAG) and $\mathrm{Ba_8Ni_4Ge_{42}}$ (BNG), were prepared by using a RF-induction furnace. The quality of these compounds were confirmed by X-ray powder diffraction as previously described [100]. Heat capacity measurements were carried out by using a Quantum Design physical property measurement system (PPMS). The C_p data of $\mathrm{Ba_8Au_{6.1}Si_{39.9}}$ (BAS), $\mathrm{Ba_8Ni_{3.8}Si_{42.2}}$ (BNS), $\mathrm{Ba_8Si_{46}}$ (BS), $\mathrm{Ba_2Sr_6Si_{46}}$ (BSS), $\mathrm{Ba_8Ga_{16}Si_{30}}$ (BGS), $\mathrm{Na_8Si_{46}}$ (NS) and $\mathrm{Sr_8Ga_{16}Si}_x\mathrm{Ge}_{30-x}$ (SGSG) are taken from Refs. [59, 60, 101–104]. Experiment details can be found in chapter 2.

3.3 Results and data analyses

3.3.1 Heat capacity data analyses

Normally, heat capacity at constant volume (C_V) and heat capacity at constant pressure (C_p) are almost the same in solids like clathrates. Therefore, in the framework of harmonic approximation, C_p can be expressed as $C_\mathrm{p} = C_\mathrm{ph}+\gamma\mathrm{T} = C_\mathrm{D}+C_\mathrm{E}+\gamma\mathrm{T}$, where C_D and C_E are the lattice heat capacities (C_ph) contributed from the Debye and the Einstein modes, respectively, and $\gamma\,\mathrm{T}$ is provided by both itinerant conduction carriers as well as tunneling states associated with phonons, as previously discussed [75, 76]. C_D and C_E can be written as,

$$C_\mathrm{D} \;=\; 9N_D\,k_\mathrm{B}\,(\frac{\mathrm{T}}{\theta_D})^3 \int_0^{x_D} dx\,\frac{x^4 e^x}{(e^x-1)^2}, \tag{3.1}$$

$$C_\mathrm{E} \;=\; 3N_E\,k_\mathrm{B}\,\frac{x_E^2\,e^{x_E}}{(e^{x_E}-1)^2}, \tag{3.2}$$

where N_D and N_E are the number of vibration modes for the Debye and the Einstein terms, respectively, and k_B is the Boltzmann constant and θ_D is the Debye temperature. The value of x can be defined as $x \equiv \hbar\omega/k_B T$, with the following notation, $\hbar$: the reduced Plank constant, ω: the oscillator frequency, $x_D = \hbar\omega_D/k_B T$: the Debye cut-off frequency ω_D, $x_E = \hbar\omega_E/k_B T$: the Einstein oscillator frequency ω_E. In a common crystalline material, C_{ph} can be described by the Debye T^3 law at low T's, as C_{E} is negligibly small in such a low T limit. However, in materials with cage structure, an excess amount of additional excitations are observed, which violates the T^3 law and creates quasi-boson peaks at around $10 \sim 20\,\mathrm{K}$ as clearly seen in the C_{p}/T^3 vs. T plot. (shown in Figure 3.2 (a))

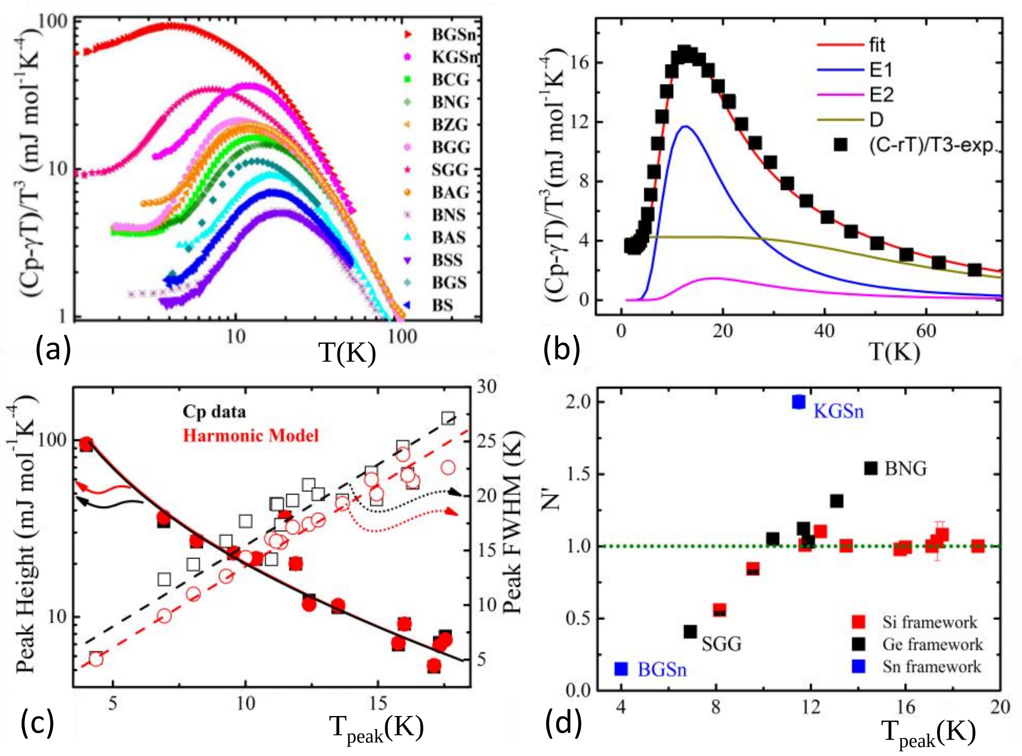

FIGURE 3.2: (a) Experimental data of quasi-boson peaks in C_{p} appearing at around $10\,\mathrm{K}$ in type-I clathrates (The compounds have been described in experiment method). (b) C_{p} data of BCG and the fitting result as described in the text. D represents the Debye model and E1 and E2 represent the Einstein model with two different frequencies ω_{E1} and ω_{E2}, respectively. (c) BP height and full width at half maximum (FWHM), obtained from experimental data in the framework of the harmonic approximation. The curves and dashed lines serve as guides for the eyes. (d) The relationship between the normalized number of 6d parallel modes N' and the peak temperature T_{peak}.

Good fitting can be obtained for the experimental C_{ph} data by applying the Debye and the Einstein models as shown in Figure 3.2. Here, only the 6d parallel modes with the lower excitation energy ω_{E1} and the 6d vertical modes with the higher energy ω_{E2} were considered for the Einstein modes, while the 2a modes were treated in a conventional manner for C_{p} data analyses (see Figure 3.1 (a) for the description of the modes). According to the cage structure, in principle, there are 12 modes in the 6d parallel direction and 6 modes in the 6d vertical direction in a unit cell. Generally, the 6d parallel modes dominate the quasi-boson peaks, while the 6d vertical modes contribute only by less than 10 percent, as can be seen in Figure 3.2 (b). In the actual fitting, we set N_{E2}=6 and left N_{E1} as a free variable. The fitting results are given in Figure 3.2 (c) and (d), and the fitting parameters are summarized in Table 3.1. For most of the compounds, the harmonic models show peak height, full width at half maximum (FWHM) and T_{peak} consistent with the experiment data as shown in Figure 3.2 (c). It is obvious that these harmonic models could describe the C_{p} well for these materials. It should be noted that the peaks of the experiment data are slightly wider than that of the harmonic models, and the differences might arise from a more complex situation in actual materials than what described by the present models using two predominant Einstein frequencies.

The number of the 6d parallel modes N_{E1} normalized as $N' = N_{E1}/12$ is plotted as a relationship with T_{peak} in Figure 3.2 (d). The values of N' are around 1 for almost all compounds with on-centered guest atoms, except for a few compounds of KGSn and BNG showing values of 2 and 1.5, respectively. N' values higher than 1 indicate that the 6d parallel modes are mixed with other modes due to their similar energies, where additional modes are most probably contributed from the acoustic branches near the Brillouin zone boundaries because the acoustic dispersion curve is strongly flattened around these areas. This situation can be schematically shown in Figure 3.3, where N' is larger than 1 for the phonon dispersion relations on the left side (red) and N' equals to 1 for the right side (blue). The above discussions also show that the rattling energies of KGSn and BNG are relatively high comparing with their acoustic phonon energies at Brillouin zone boundaries.

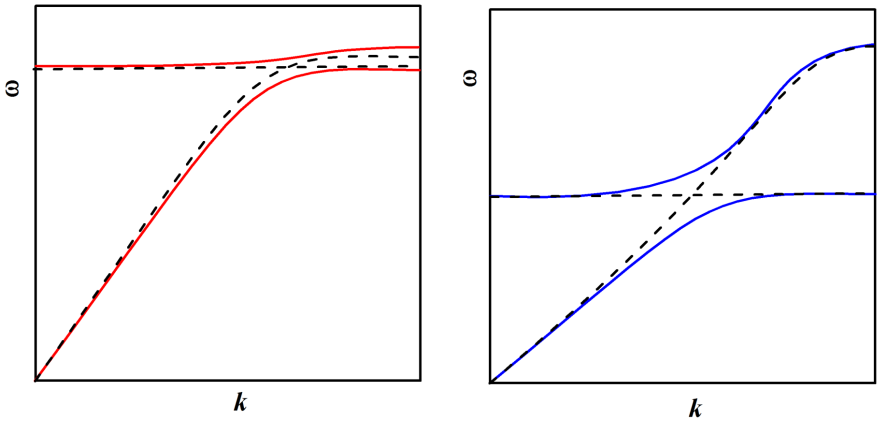

FIGURE 3.3: Rattling phonon modes in phonon dispersion relations. On the left side, a rattling phonon branch crosses an acoustic branch near the Brillouin zone boundary, while on the right side, the crossing is far from the Brillouin zone boundary.

On the other hand, N' is much smaller than 1 for the compounds showing off-centered guest atoms, as in the case of BGSn with $N' = 0.15$ and SGG with $N' = 0.41$. It seems that the reduction in the number of modes frequently happens when the Einstein mode energies become sufficiently low (indicated by T_{peak}) and the phonons becomes more anharmonic. Despite the insufficient understanding on the physical origins of boson peaks, the newly defined parameter N' seems to represent the strength of phonon anharmonicity in a successful fashion. It should be noted, however, that the harmonic model cannot be suitable in principle for BGSn and SGG with strong anharmonicity. Instead, a more complex model, such as the soft potential model should be applied. However, as far as the purpose of the present discussion is concerned, the harmonic fitting is sufficient.

It should be noted that although there might be some errors in the nonlinear fitting to C_{p}, the fitting results are reliable as they are consistent with other experimental data obtained from INS, Raman scattering, X-ray/Neutron diffraction measurements as also listed in Table 3.1.

TABLE 3.1: The fitting parameters, θ_{E1}, θ_{E2}, θ_D and N' for the C_{p} data shown in Figure 3.2 (a). The numbers in parentheses are the x values, corresponding to $Ba_8Au_xSi_{46-x}$ and $Sr_8Ga_{16}Si_xGe_{30-x}$, respectively.

compounds	θ_{E1} (K)	θ_{E2} (K)	θ_D (K)	N'	Ref. θ_{E1} (K)
BS	76	110	372	1.0	71 (R) [72]
BGS	63	107	330	1.1	63 (R) [105], 69 (A) [106]
BAS(6.1)	74	95	326	1.0	73 (C_{p}) [101]
BAS(5.6)	78	84	343	1.0	76 (C_{p}) [101]
BAS(4.9)	79	94	353	1.1	78 (C_{p}) [101]
BAS(4.1)	80	101	358	1.0	79 (C_{p}) [101]
BNS	87	109	399	1.0	91 (A) [102]
BAG	56	83	250	1.1	54 (I) [107] 60 (A) [107]
SGG	33	80	196	0.4	46 (R) [103] 35 (C_{p}) [103]
BGG	50	80	278	1.0	50 (R) [108] 59 (A) [56]
BZG	56	84	280	1.2	56 (I) [109] 62 (A) [110]
BNG	70	85	282	1.5	63 (I) [109] 79 (A) [111]
BCG	62	82	281	1.2	57 (I) [109] 63 (A) [107]
SGSG(30)	60	110	370	1.1	59 (C_{p}) [103]
SGSG(25)	58	112	317	1.0	56 (C_{p}) [103]
SGSG(10)	47	106	241	0.8	46 (C_{p}) [103]
SGSG(5)	40	82	220	0.6	41 (C_{p}) [103]
KGSn	57	90	191	2.0	65 (A) [112]
BGSn	20	75	118	0.2	20 (C_{p}) [41]
NS	106	147	560	1.0	110 (A) [104] 94 (C_{p}) [104]
KS	-	-	-	-	120 (R) [113]
Rb_8Sn_{44}	-	-	-	-	49 (R) [114]
Cs_8Sn_{44}	-	-	-	-	36 (R) [114]
$Rb_8Hg_4Sn_{42}$	-	-	-	-	43 (R) [114]

A: ADP; R: Raman; I: INS

3.3.2 Theoretical calculations

The Gaussian 09 program [115] was used to calculate the vibrational frequencies of the guest atoms inside 24-cages of ASi_{24}, where A is Sr, Ba, Na, K, Rb, Cs, as well as inner gas elements of He, Ne, Ar, Kr, Xe in the framework of a cage cluster model. The structure was optimized using density functional theory (DFT) with Becke's three parameter hybrid [116] correlated with the Lee-Yang-Parr (B3LYP) method [117]. The 6-31G$*$ basis set was used [118] for the atomic numbers not larger than 36 (Kr), while for heavier elements, the LANL2DZ basis set [119] with pseudo potential was used. The calculated vibration (IR) spectrum for BaSi$_{24}$ is shown in Figure 3.4 (a) as an example. The guest modes including the 6d parallel and vertical modes can clearly be differentiated, and there are two degenerate modes in the 6d parallel modes corresponding to the two degrees of freedom parallel to a hexagonal face. The calculations are consistent with the experimental data not only for the number of modes but also for the oscillation frequencies as shown in Figure 3.4 (b). This is a strong evidence that the guest-host interactions are limited inside of a cage, and that the influence from the other atoms outside of the cage is negligibly small. The calculated results of the guest vibration frequencies and the Fc's are summarized in Table 3.2.

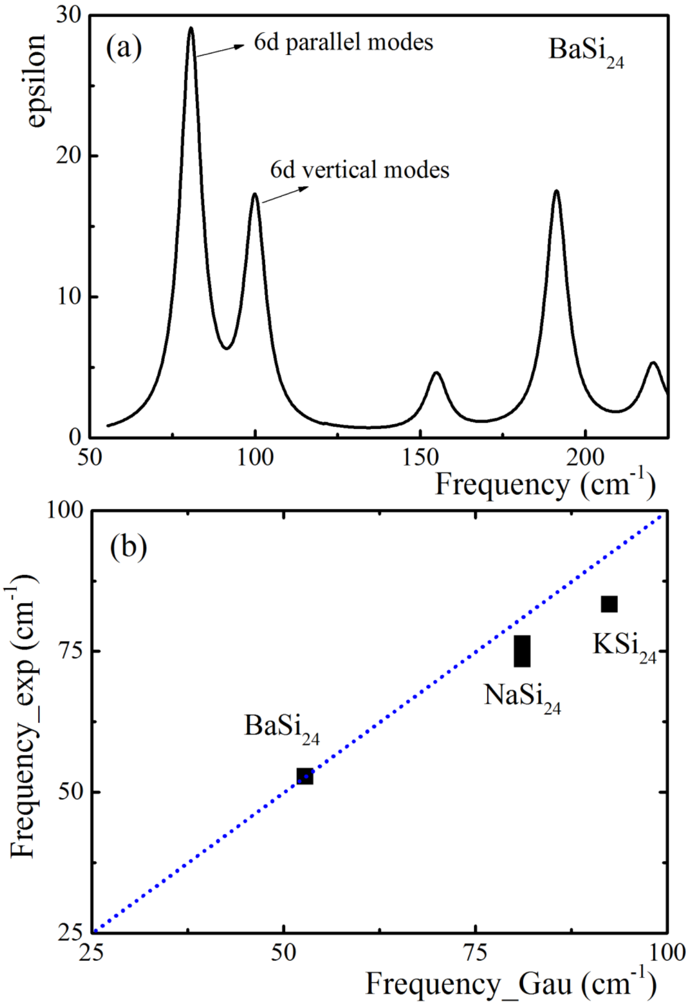

Figure 3.4: Guest vibration modes in tetrakaidecahedral cages. (a) The IR spectrum of BaSi$_{24}$ calculated by the Gaussian 09 code. Two lowest peaks, corresponding to the guest vibrations are displayed. (b) A comparison between the calculations and the experiments. The calculated frequencies are renormalized by the mass of guest atoms, and the experiment data are taken from Table 3.1. The dotted line are a guide for the eyes.

First principles band calculations were made using the Vienna Ab-initio Simulation Package (VASP) program [120]. The PAW type pseudo-potentials [121, 122] and the density functional

Table 3.2: Theoretical calculations of vibration frequencies and corresponding Fc's. The cages from $SrSi_{24}$ to $XeSi_{24}$ are calculated by the Gaussian 09 code, while compounds BS(x) as a function of contraction of cell parameter are calculated by the VASP program.

Name	ω (cm^{-1})	Fc (mDyn/Å)
$SrSi_{24}$	62.7	0.200
$BaSi_{24}$	52.8	0.228
$NaSi_{24}$	81.1	0.088
KSi_{24}	92.5	0.197
$RbSi_{24}$	68.2	0.234
$CsSi_{24}$	60.8	0.258
$HeSi_{24}$	99.1	0.023
$NeSi_{24}$	64.4	0.050
$ArSi_{24}$	82.0	0.158
$KrSi_{24}$	57.3	0.162
$XeSi_{24}$	51.5	0.205
BS(100)	57.3	0.266
BS(99)	61.4	0.306
BS(98)	65.3	0.346
BS(97)	69.2	0.389
BS(96)	72.9	0.431
BS(95)	76.6	0.476
BS(94)	79.4	0.512

(GGA/PBE [123]) were used for description of the electronic states. The plane wave basis set with cut-off energy of 700 eV and $4 \times 4 \times 4$ Monkhorst-Pack k-point meshes were applied to the $1 \times 1 \times 1$ unit cell (X_8Si_{46}). The lattice constant was set to 1.041 nm, which shows the minimum total energy for Ba_8Si_{46} within the above calculation condition. Structure optimization was performed under the bcc symmetry with the convergence criterion with $\Delta E = 1.0$ meV.

3.3.3 Unification of quasi-boson peak energies

The quasi-boson peaks originating from the vibrations of a guest atom in a cage compound are supposed to depend on the space for freedom in the rattler limit and the mass of the encapsulated atom in the harmonic oscillator limit. In order to clarify their features, we tentatively plotted the specific energies of the quasi-boson peaks (θ_E), in units of temperature (K), as a function of either cage radius (R) in Figure 3.5 (a) or mass (m) of an atom accommodated inside a cage in Figure 3.5 (b). Here, the cage radius R is defined as the shortest distance between the center of a cage and the nearest atom residing on the larger host 24-cage (refer to Figure 3.1 (a) and Figure 1.7). As can be clearly seen in Figure 3.5 (a), the quasi-boson peak energies are strongly reduced as the R parameter increases, indicating that they are in the rattler space limit. It is also apparent, at the same time, that the energies depend on the mass of guest atoms as shown by the linear guiding line in Figure 3.5 (b), being indicative of Einstein localization limit. Intriguingly, the kind of atoms constructing the host cage structure seems to have nearly no influence on the quasi-boson peak energies. The experimental fact, deduced from these two fundamental limits, suggests that understanding the origin of the quasi-boson peaks may be less complex than we originally considered.

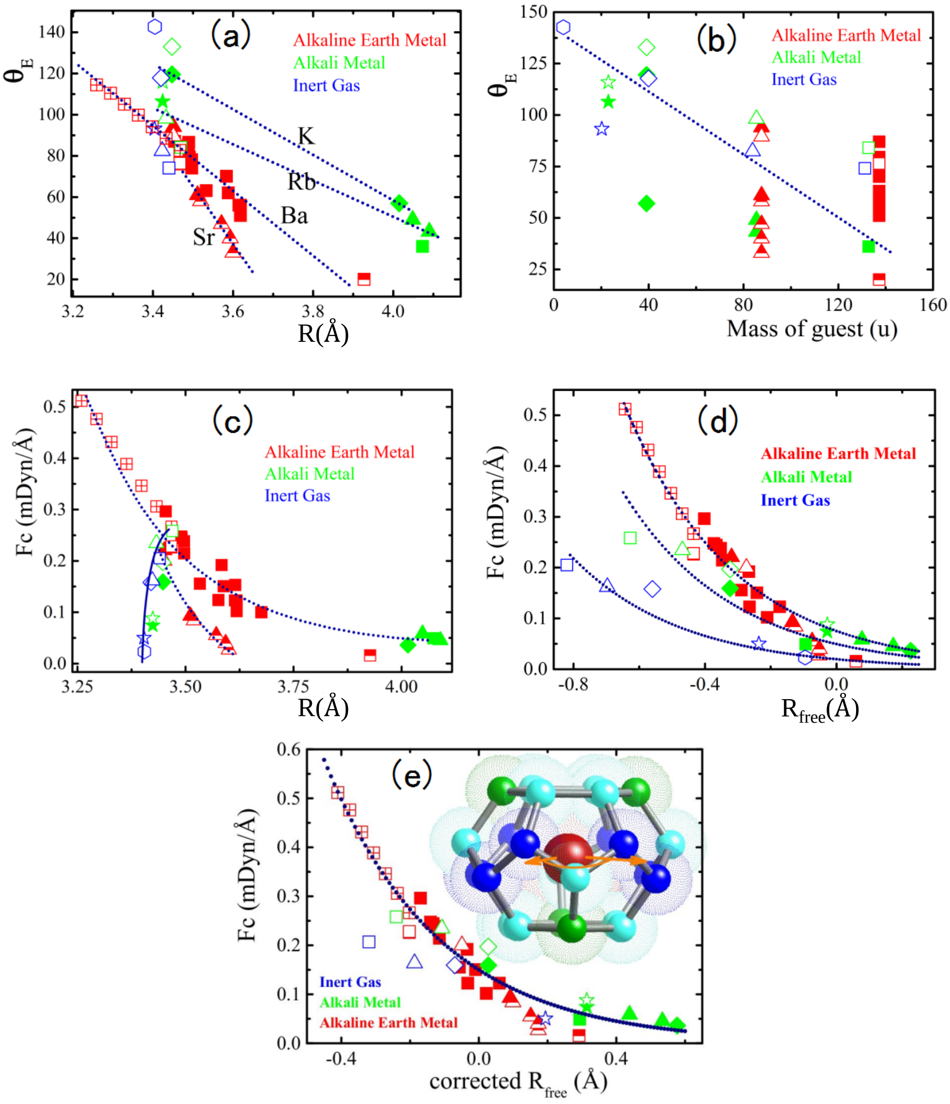

FIGURE 3.5: Quasi-boson peak energies as a function of different parameters. (a) The relationship between θ_E and R. The dotted lines are guides for the eyes. (b) The relationship between θ_E and the mass of the guest elements (m). The dotted line is a guide for the eyes. (c) The relationship between Fc and R. The dotted lines and the solid line serve as guides for the eyes. (d) The relationship between Fc and R_{free}, as defined in the text. The lines are fitting results by employing exponential functions. (e) The relationship between Fc and the corrected R_{free} by applying the radii of the guest atoms evaluated from the first principles calculations. The inset on the top right corner is a 24-cage (Figure 3.1) and the 6d parallel modes, corresponding to the vibration energies, are sketched by two orange arrows. Legends: hexagon: He; star: Ne and Na; diamond: Ar and K; up triangle: Kr, Rb and Sr; square: Xe, Cs and Ba. The empty symbols and the ones with a cross inside: theoretical calculations evaluated by using Gaussian 09 and VASP, respectively. The half filled symbols: compounds showing strong phonon anharmonicity. The data of BAS, BNS, SGSG, K_8Si_{46} (KS), Na_8Si_{46} (NS), Rb_8Sn_{44}, Cs_8Sn_{44}, $Rb_8Hg_4Sn_{42}$ are from Refs. [72, 101–104, 114]. All the data are listed in tables 3.1 and 3.2.

In order to observe clear correlations between the quasi-boson peak energies and the structure, a new parameter associated with the free space (R_{free}) was introduced in place of R. We define the the free space as $R_{\mathrm{free}} = R$-R_{g}-R_{h}, where g and h stand for an accommodated guest and a host-cage atoms, respectively. As for the mass, m of an atom accommodated in a cage can be used in place of the reduced mass ($\mu = Mm/(M+m)$) because the cage framework mass (M, as the sum of a number of atoms residing on a cage) is much larger than m ($M \gg m$). For describing the quasi-boson peak energies, we used the force constant Fc, where the mass (Fc=$(\theta_E)^2 m$) is renormalized under a two-body harmonic oscillator model. Because the space inside the 24-cage, as estimated previously [75], is indeed large, van der Waals type interactions would be dominant between guest atoms and the cage atoms. Tentatively, we employed van der Waals radii (R_{vdw}) given in the literature [124–126] for both R_{g} and R_{h}. The used values are 1.625 Å(Sr^{2+}), 1.802 Å(Ba^{2+}), 1.352 Å(Na^{+}), 1.671 Å(K^{+}), 1.801 Å(Rb^{+}) and 1.997 Å(Cs^{+}) for ions; and 1.40 Å(He), 1.54 Å(Ne), 1.88 Å(Ar), 2.02 Å(Kr), 2.16 Å(Xe), 2.10 Å(Si), 2.11 Å(Ge), 2.17 Å(Sn), 1.87 Å(Ga), 1.39 Å(Zn), 1.4 Å(Cu), 1.63 Å(Ni), 1.72 Å(Ag), 1.66 Å(Au) and 1.55 Å(Hg).

The relationship between Fc and a new parameter R_{free} is shown in Figure 3.5 (d). Interestingly, the experimental data fall into three groups: inert gas (G), alkali metal (A) and alkaline earth metal (E), respectively. The three data sets are fitted well by exponential functions, $F_c = \mathrm{C}\exp(-3\,R_{\mathrm{free}})$, with C equal to $(7.53\pm0.15)\times10^{-2}$ m Dyn/Å for E elements, $(4.97\pm0.43)\times10^{-2}$ m Dyn/Å for A elements and $(1.98\pm0.19)\times10^{-2}$ m Dyn/Å for G elements. A great surprise at this stage is that all three groups were described by exactly the same exponential function of $\exp(-3\,R_{\mathrm{free}})$ with only small differences in the prefactors of C. This is not coincidental and strongly suggests that the three curves might be unified as a single-curve relationship. For achieving such unification of the three lines (for E, A, and G of elements), one could take two different positions. The first position is that the different prefactors have a physical meaning, and they may originate from additional interactions which are not taken into account in the present discussion. The second position is that the van der Waals radii employed in literatures to evaluate R_{free} are not sufficiently suitable parameters for describing clathrate systems that contain cage structures. We show here that the second interpretation is correct and that the ionic interactions, generally considered to be important, exert little influence.

It is important to know that van der Waals interactions should seriously be taken into consideration even in ionic species and a lot of citations are available for such a discussion [126]. In the present paper, the guest atomic radii R_{g} to be applicable to clathrates were theoretically re-evaluated by applying first principle calculations. We calculated electron density contour maps for various clathrates as shown in Figure 3.6. The guest radii were determined by the red contour zone of the electron density map. The values were deduced to be: 1.57 Å (Ba in Ba_8Si_{46}), 1.54 Å (Ba in Ba_8Ge_{46}), 1.40 Å (Sr), 1.61 Å (Cs), 1.44 Å (Rb), 1.32 Å (K in K_8Si_{46}), 1.01 Å (Na), 1.66 Å (Xe), 1.51 Å (Kr), 1.39 Å (Ar), 1.11 Å (Ar), and 1.36 Å (K in KCl). One can see that the radii can be evaluated by the boundary where the wave function shows a sharp change in the electron density map. It should be noted that the evaluation method of the radii using the equivalent electron density contour map can also provide a good conceptual image of the free space inside a cage. It was found as a suprise that all experimental data can successfully be located on a single universal line, when R_{free} is re-evaluated by using the new values of R_{g} as shown in Figure 3.5 (e). The unified exponential curve, $\mathrm{Fc} = 0.15\exp(-3\,R_{\mathrm{free}})$ was successfully deduced from the data, except for only a few compounds with small deviations showing extremely strong phonon anharmonicity,

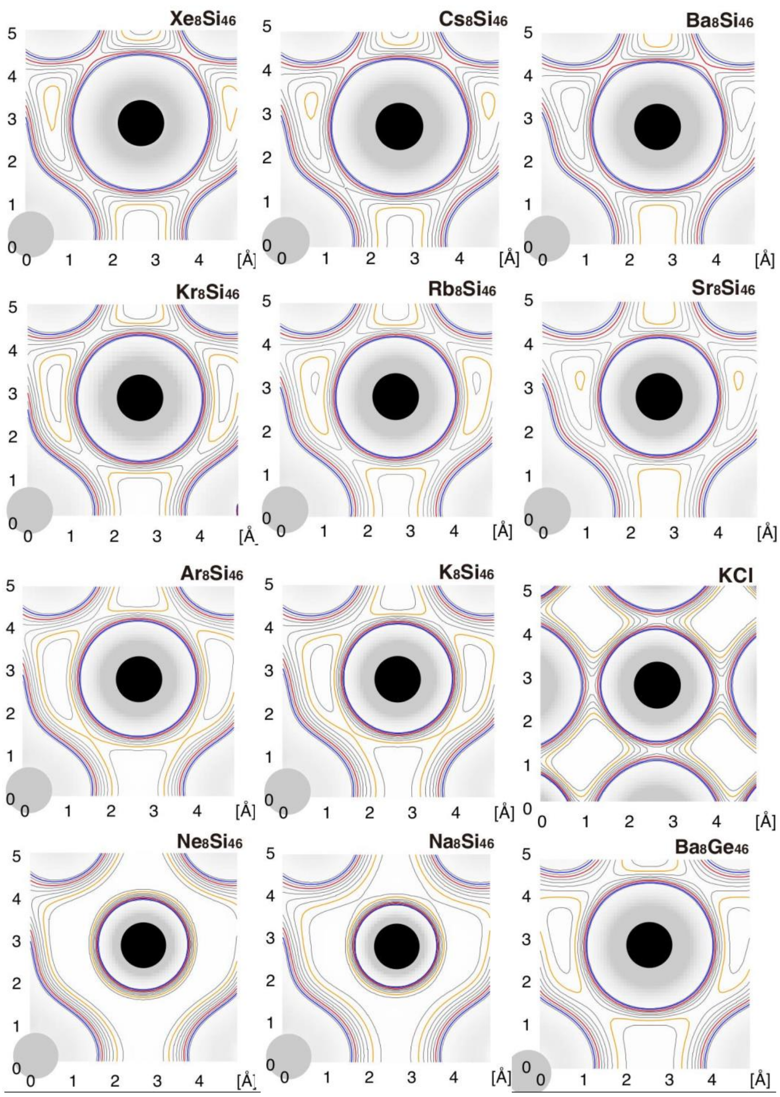

Figure 3.6: The electron density counter maps for guest atoms of various clathrates, A_8Si_{46} (A = Ba, Sr; Cs, Rb, K, Na; Xe, Kr, Ar, Ne) and Ba_8Ge_{46}, in addition to KCl for comparison.

such as $Ba_8Ga_{16}Sn_{30}$ (BGSn), SGG and $Sr_8Ga_{16}Si_xGe_{30-x}$ (SGSG) [103], shown by half filled symbols in Figure 3.5 (e).

This unified exponential relationship gives the following important messages on the quasi-boson peaks: (1) The most important interaction for contributing to the quasi-boson peaks in clathrates is the weak repulsive van der Waals interactions created by the cage. It is shown later that the anharmonic terms resulting from these repulsive terms is unexpectedly much smaller than the harmonic terms. (2) Neither Coulomb ionic nor covalent bonding interactions provide large influence on the quasi-boson peaks. This is a little bit contradictory to the previous reports, but can be justified by first principles band calculations. (3) These conclusions are strongly indicative of the fact that broken or lowering in symmetry of a cage caused by weak guest-host interactions is very crucial for yielding the large anharmonicity in phonons appearing at low temperatures. The conclusion of (1)-(3) are actually essentially important factors in glass-like materials. The large freedom in space solely is not sufficient and broken or lowering symmetry is essential for creating quasi-boson peaks providing extremely low energies accompanied by large anharmonicity of phonons. Given lower symmetry as well as sufficient space of the guest atoms, hidden ionic and/or covalent attractive force interactions emerge at low temperatures, where the guest atoms are at the same time off-centered [75, 76]. Lower symmetry as well as disorder can be created by the rearrangement of the atoms residing on the host cage, and therefore some ternary-component clathrates shown by the half filled symbols in Figure 3.5 (e) display a tendency towards strong phonon anharmonicity with much lower Fc even though R_{free} is not the largest among the clathrates studied here.

3.4 Interpretations and discussions

3.4.1 Interpretations by ab initio & first principle calculations

It has been described so far that the quasi-boson peaks, arising from the atomic vibrations with large freedom inside a cage, can be interpreted as a consequence of the weak van der Waals replusive interactions between the guest atoms and the host cage atoms. Now we provide an important justification by first principles calculations and a potential model based on van der Waals interactions.

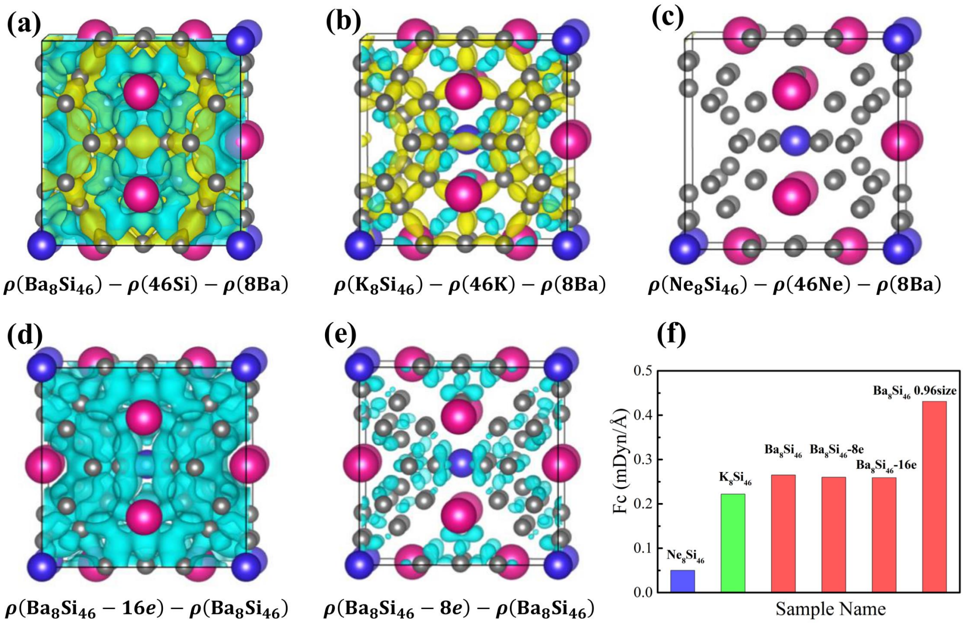

Figure 3.7: Electron density difference maps and the corresponding Fc, calculated by using the VASP code. Red and blue spheres represent the guest atoms at non-equivalent sites. Gray ones represent Si atoms. (a)-(c): Charge redistribution with the introduction of guest atoms in $\mathrm{Ba_8Si_{46}}$, $\mathrm{K_8Si_{46}}$ and $\mathrm{Ne_8Si_{46}}$, where the blue region is electron decreased and the yellow region is electron increased. (d),(e): Difference in spatial charge density (electron decreased region) between positively charged (+8 and +16) and neutral systems. (f) A comparison of the calculated Fc.

In order to judge how we should consider ionic interactions, we made two types of calculations by using the VASP code [120]. First we calculated the electron density distribution and the guest vibration frequencies for $\mathrm{Ne_8Si_{46}}$, $\mathrm{K_8Si_{46}}$ and $\mathrm{Ba_8Si_{46}}$. The electron density difference maps in one unit cell are shown in Figure 3.7 (a)-(c), and the Fc estimated for the 6d parallel modes (Figure 3.1) are shown in Figure 3.7 (f). These calculations provide important information as to how extent the ionic states of divalent (Ba^{2+}), monovalent (K^+) and zero-valent (Ne^0) guest atoms affect the interaction strength. At first glance, electron is transferred from the guest atoms to the host cage frameworks as can be visualized in Figure 3.7 (a)-(c) by blue (electron decreased) and yellow (electron increased) regions. For instance, one electron or two electrons are transferred from K or Ba to the Si_{46} cage network in the case of Ba_8Si_{46} and K_8Si_{46}, respectively, while negligible electron transfer was detected for Ne_8Si_{46}. Meanwhile, the calculated Fc's, which are quantitatively in good agreement with the values used in Figure 3.5, become smaller from Ba to K and to Ne, as can be seen in Figure 3.7 (f). It can be imagined that the guest valences may have some influence on the guest-host interactions; however, this conclusion is not correct as we shall see in the following paragraph.

We performed additional calculations supposing a different situation in order to clarify the charge influence. Eight or sixteen electrons were hypothetically removed from the Si_{46} cage network in Ba_8Si_{46} in the first step. Structure optimization with constraint of the same lattice parameter shows no significant displacement of atoms in the both systems. The electron density difference and the corresponding Fc were calculated for $Ba_8Si_{46}(-16e)$ and $Ba_8Si_{46}(-8e)$, respectively as shown in Figure 3.7 (d),(e) and (f). Almost the same maps were obtained with $\sum |LUMO + i|^2$ (i =0 to 3 for "-8e" and i =0 to 7 for "-16e") of the neutral Ba_8Si_{46}. Strikingly, the frequencies of the guest vibrations have a negligible dependence on these hypothetical charge variations, as shown in Figure 3.7 (f). These calculations clearly demonstrate that the Coulombic ionic interactions do not provide significant contributions to the quasi-boson peaks. Actually, according to the electron density maps shown in Figure 3.8 (a)-(c), the free space becomes larger from Ba to K and to Ne. Therefore the different Fc's shown in Figure 3.7 (f) should be ascribed to the free space of the guest atoms associated with van der Waals radii rather than their charge valences.

For further understanding, we calculated the Fc when the lattice of Ba_8Si_{46} is hypothetically contracted up to $0.94a$, where a is the cell parameter. The electron density map of Ba_8Si_{46} with $0.96a$ is shown in Figure 3.8 (d) as an example. Importantly, the Fc evaluated by the first principles band calculations under a hypothetical high pressure can be on the unified line in a fairly good fashion as shown in Figure 3.5 (e). This fact also supports our interpretation that the potential inside a cage can predominantly be controlled by the repulsive van der Waals interactions between a guest atom and the cage framework and that ionic interactions indeed make little contribution.

3.4.2 Theoretical modeling

The energy potential in a system consisting of two atoms, which interact with each other via van der Waals repulsive and attractive interactions, can be described by using a modified Morse potential [127] given by $V(r) = ae^{-nb(r-r_e)} - ane^{-b(r-r_e)}$, where r is the distance of the two atoms, r_e is their equilibrium distance; n, a and b are free parameters with $n \gg 1$ for creating a stable potential. The first and the second terms correspond to the repulsive and the attractive interactions, respectively. Given a situation in which two identical atoms are located in a host cage framework separated by a distance of $2R$ (the radius of a cage is R) and a guest atom is located on the line connecting these two cage atoms as shown in Figure 3.9 (b), the total potential

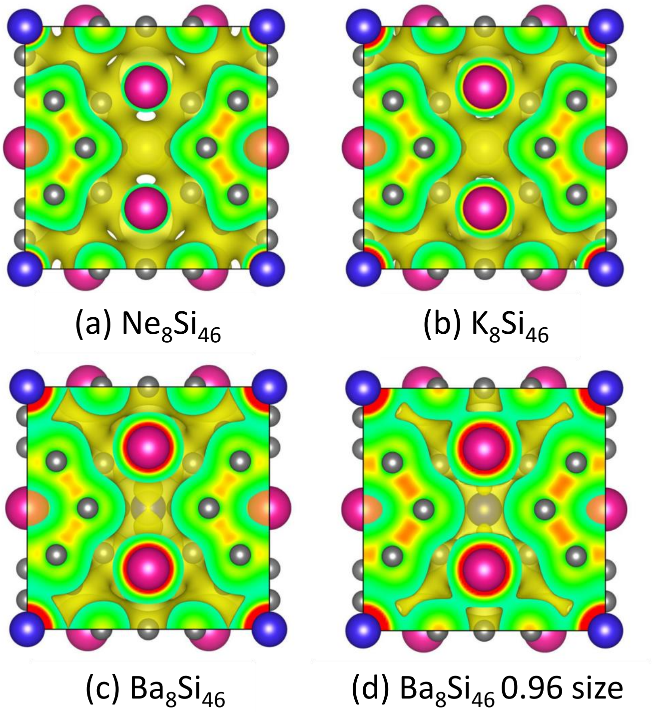

FIGURE 3.8: Electron density maps, calculated by VASP for Ne_8Si_{46}, K_8Si_{46} (KS), Ba_8Si_{46} (BS) and BS with $0.96\,a$, where a is the lattice constant. A section map is overlaid on an isosurface map. Red and blue spheres represent the guest atoms at non-equivalent sites. Gray ones represent Si atoms.

$V_t(r)$ inside a cage can be described as

$$\begin{aligned} V_t(r) &= V(R+r) + V(R-r) \\ &= ae^{-nb(R+r-r_e)} - ane^{-b(R+r-r_e)} \\ &\quad + ae^{-nb(R-r-r_e)} - ane^{-b(R-r-r_e)} \end{aligned} \tag{3.3}$$

According to eq. (3.3), the first and the second derivatives of $V_t(r)$ are,

$$\begin{aligned} V_t^{'}(r) \;=\; & -anbe^{-nb(R+r-r_e)} + anbe^{-b(R+r-r_e)} \\ & + anbe^{-nb(R-r-r_e)} - anbe^{-b(R-r-r_e)} \end{aligned} \tag{3.4}$$

$$\begin{aligned} V_t^{''}(r) &= an^2b^2e^{-nb(R+r-r_e)} - anb^2e^{-b(R+r-r_e)} \\ &\quad + an^2b^2e^{-nb(R-r-r_e)} - anb^2e^{-b(R-r-r_e)} \end{aligned} \tag{3.5}$$

In the case that a guest atom is located at the center of a cage, r is equal to 0 and then we have

$$V_t(R) \;=\; 2a(e^{-nb(R-r_e)} - ne^{-b(R-r_e)}) \tag{3.6}$$

$$V_t^{'}(R) \;=\; 0 \tag{3.7}$$

$$V_t^{''}(R) \;=\; 2anb^2(ne^{-nb(R-r_e)} - e^{-b(R-r_e)}) \tag{3.8}$$

Equation (3.7) shows that either a potential minimum or a maximum appears in the center of a cage. When $V_t^{''}(R) > 0$, the central position becomes a potential minimum and stable. In order to have such an on-center condition, R should satisfy the following relation:

$$R < R_c = r_e + \frac{\ln(n)}{nb - b}. \tag{3.9}$$

On the other hand , when R is larger than R_c ($V_t^{''}(R) < 0$), the central position becomes a potential maximum and the guest atom moves towards the cage side until it reaches a stable off-center position. Since most of the type-I clathrates have on-centered guest atoms except for a few compounds like BGSn, SGG and SGSG, which show strong anharmonicity in the phonon modes, the condition of R less than R_c can be realized. Based on the model described above, Fc can be described by the second derivative $V_t^{''}(R)$ in the framework of the harmonic approximation,

$$\mathrm{Fc} = 2anb^2(ne^{nbr_e}e^{-nbR} - e^{br_e}e^{-bR}) \tag{3.10}$$

In principle, r_e can be estimated as R_h+R_g. According to eq. (3.10), if r_e is fixed to be constant, i.e., R_h+R_g does not largely vary, Fc exponentially decrease as R increases under the condition that $ne^{nbr_e}e^{-nbR} \gg e^{br_e}e^{-bR}$. This can actually be exemplified by the dotted lines in Figure 3.5 (c) for Ba and Sr inclusion clathrates, respectively. On the other hand, in the case of the same cage with little variation in R, Fc should increase exponentially as r_e increases. This situation can be seen by the solid lines in Figure 3.5 (c) for the Si clathrates with different guest atoms. In order to achieve a unified relationship for the quasi-boson peaks appearing in clathrates, we introduced a new parameter associated with the space freedom in a cage with the definition of R_fee=R-R_h-R_g as described earlier. According to the definition of r_e, R_free should equal to R-r_e, and consequently the general expression of Fc using the new parameter R_free becomes

$$\begin{aligned}\mathrm{Fc} &= 2anb^2(ne^{-nbR_\mathrm{free}} - e^{-bR_\mathrm{free}}) \\ &\cong 2an^2b^2e^{-nbR_\mathrm{free}},\end{aligned} \tag{3.11}$$

where we suggest $ne^{-nbR_\mathrm{free}} \gg e^{-bR_\mathrm{free}}$. Actually, we have shown earlier (Figure 3.5 (e)) that all Fc values of the quasi-boson peaks in type-I clathrates can be correlated by a single unified exponential function, although clathrates showing off-entered guest atoms give a little bit lower Fc. It should be noted that the second term in eq. (3.11) also gives a negligible contribution, and therefore, Fc can safely be expressed by the first term, $\mathrm{Fc} = 2an^2b^2e^{-nbR_{free}}$. When the expression of Fc is compared with the fitting result in Figure 3.5 (e), $\mathrm{Fc} = 0.15\exp(-3\,R_\mathrm{free})$ is available, and one can evaluate nb=3 Å^{-1} and a=8.33 μDyn Å=52.1 meV.

We tested how the model described in the present paper is applicable to the observed experimental data as shown in Figure 3.9 (a). The critical radii (R_C) are compared with the cage radii (R) and they are plotted as a relationship with n for BS, BGG and BGSn. According to Figure 3.9 (a), even for the smallest n, R<R_C. This is indicative of the fact that type-I clathrates can in principle be classified as guest on-centered compounds as we discussed earlier.

The above situation can also be displayed as in Figure 3.9 (b), where the cage size (2R) varies from 6.5 to 8.5 Å. It is clear from this figure that the potential strongly depends on the cage size. When the cage becomes smaller, the potential becomes sharper, while the cage becomes larger, the potentials becomes soft and flat by ending up with a symmetric two-well potential as shown in the lower right corner of Figure 3.9 (b). However, it should be kept in mind that R experimentally determined for type-I clathrates is always smaller than R_c of the model described

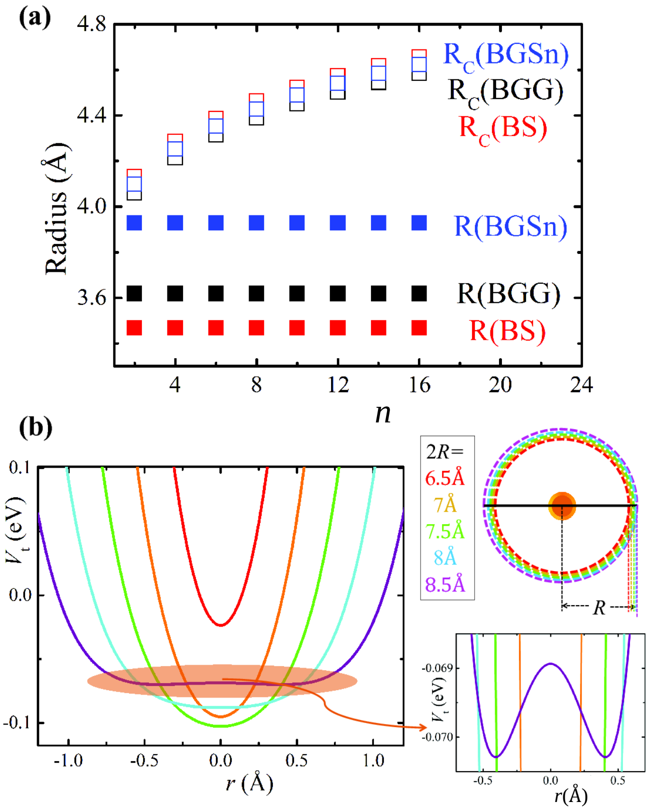

FIGURE 3.9: A simulation based on the Morse potentials (a) The comparison between the critical radii (R_C), calculated by eq. (3.9) and the cage radii (R). (b) The potential simulated according to eq. (3.3). The top right corner shows the configuration in the potential model, where a guest atom is on the center and the cage atoms are on the two sides. The cage size ($2R$) varies from 6.5 to 8.5 Å. r_e is set as 3.67 Å, corresponding to the situation of BGSn, and n is set as the minimum value of 2. The picture at the lower right corner shows an off-centered potential when the cage radius becomes larger than R_c.

above, and therefore the space found in clathrates is not large enough to allow the appearance of off-center positions. In order to understand the off-centered situation, the space factor solely is not sufficient, a lower symmetry becomes quite important as well. Typical good examples are comparisons between BGG and SGG, as well as between KGSn and BGSn. In the former case, besides the large free space of Sr inside the cage, it has also been reported that the cage structure of the two compounds is different due to the interactions between the guest atoms (Ba or Sr) and the atoms residing on the cage [51, 83], and therefore off-centered Sr can be realized in SGG, while Ba is located in the center of the cage for BGG. In the latter case, an off-centered situation can only be observed for BGSn but not for KGSn, although both clathrates have a similar cage in size with each other. Previous report showed in the latter case that the difference originates from the arrangement of the cage atoms [41, 112]. It is also important to point out that asymmetry of the two-well potential is essential for the tunnelling described by Anderson [75, 76, 79].

3.5 Summary

We showed that the excitation energies of all quasi-boson peaks, which are experimentally observed in clathrates with cage structures, can surprisingly be unified as one single exponential line using a new space parameter (R_{free}) associated with the freedom of motion of atoms inside the larger 24-cage. A model based on the van der Waals repulsive term explained the intrinsic nature for the single exponential relationship between the quasi-boson peak energies and the structural factors. Discussions were made on a basis of both experimental data and theoretical calculations, and it was clarified, being contrary to the previous reports, that Coulombic ionic and/or covalent interactions are not significantly important on the energy scale of the quasi-boson peaks. Actually, in a glass system, the emergent boson peaks are suggested to be associated with localized phonons, originating from defect-like structures [98, 128], which is indicative of the very important role of the symmetry broken of the system that emerges statically or dynamically depending on the chemical and physical environmental conditions. The influence of the broken and lowered symmetry gradually becomes evident at low temperatures [79]. Although the origin of the boson peaks appearing in glass-like materials is complex to understand due to the missing information on the real structure, the understanding described in the present paper is very general and provides important information. It deserves to note that the van der Waals-type weak interactions, which lead to the quasi-boson peaks, are consistent with the recent part-liquid concept [23, 77, 78] and should be useful for thermoelectric materials design.

Chapter 4

Tunneling States and Phonon Anharmonicity

A Brief Abstract

A systematic study on the anharmonicity of phonons is made for single crystal type-I clathrates: n-type $Ba_8Ga_{16}Ge_{30}$ (n-BGG), p-type $Ba_8Ga_{16}Ge_{30}$ (p-BGG), n-type $Sr_8Ga_{16}Ge_{30}$ (n-SGG), n type $K_8Ga_{16}Sn_{30}$ (n-KGSn) and n type $Ba_8Ga_{16}Sn_{30}$ (n-BGSn) based on their heat capacity C_p at extremely low temperatures (T) down to 360 mK. The low-T linear terms ${}^{obs}\gamma T$ of C_p, including the tunneling-term of the atoms accommodated in the host cages ($\gamma_{ph}T{=}\alpha T$) and the Sommerfeld itinerant-electron term ($\gamma_e T$), are successfully separated through careful measurements of sigle crystals with various carrier concentrations. The values of the minimum density of anharmonic potentials are deduced from α to be 0.12 ± 0.24 for n-KGSn, 0.47 ± 0.24 for n-BGG, 1.9 ± 0.8 for p-BGG, 6.0 ± 0.9 for n-SGG, 10.9 ± 0.7 for n-BGSn in the unit of $\times 10^{15}\mathrm{cm}^{-3}$. The effective mass ($m^*/m_0$) is determined from γ_e to be 1.01±0.25 for n-BGG, 1.20±0.19 for p-BGG, 1.68±0.24 for n-SGG, 1.86±0.54 for n-KGSn and 2.05±0.48 for n-BGSn in the unit of free electron mass m_0, and the electron-phonon interaction strength can be evaluated from these values. It is shown that both the thermal conductivity (κ) and the electron-phonon interaction strength (λ) agree well with the α parameters deduced from C_p. The differences in κ known between n- and p-BGGs are ascribed to the influence of defects at the crystallographic 6c sites, which are clearly indicated by magnetic susceptibility measurements. This is very different from the situation in the other clathrates. The influence of the anharmonicity of phonons on thermoelectric power factor is highlighted from the view point of m^* as well.

4.1 Introduction

Intermetallic clathrates, first reported by Cros et al. [31], are a class of compounds characterized by cage-like polyhedral hosts composed mainly of the IV^{th} group elements such as Si, Ge, or Sn with alkali metal or alkaline-earth metal elements accommodated inside the cages as guest atoms. A detailed introduction of clathrates can be found in chapter 1. A typical structure, same as in Figure 1.7, is shown again here in Figure 4.1, where the guest atoms reside in both the two small dodecahedra and the six larger tetrakaidecahedra in one unit cell. This particular structure is known as a Type-I clathrate. One of the most intriguing issues in type-I clathrates is their outstanding thermoelectric performances, which they achieve thanks to the exceptionally low thermal conductivity (κ) as reported earlier [129, 130]. This originates from the rattling motion of the guest atoms, which produces relatively low energy and low dispersive phonons [19], which strongly scatter the acoustic phonons, leading to a suppression of κ. The low κ and excellent electrical transport performance make clathrates similar to a conceptual ”phonon glass electron crystal: PGEC” [131]. Therefore, these materials are considered to be useful for thermoelectric energy conversion from the viewpoint of their high figure of merit $ZT{=}S^2(\sigma/\kappa)T$, where S is the Seebeck coefficient, σ the electrical conductivity and T the temperature. Consequently, the driving phonon anharmonicity associated with the anomalous motions of the endohedral atoms (guest atoms residing inside the cage) is of great interest and has been widely studied [41, 51, 58, 73, 76, 132–136].

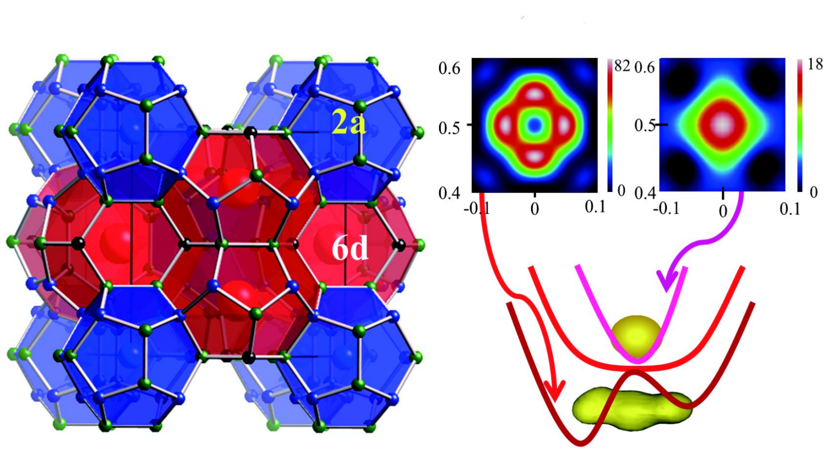

FIGURE 4.1: The typical structure of type I clathrate (left); dodecahedral cages (blue) with 2a endohedral atom sites, and tetrakaidecahedral cages (red) with 6d endohedral atom sites are shown. Electron density maps of the guest atoms with off-centered mode around the 6d sites and on-centered mode at 6d sites, visualized by the inverse Fourier transformation from single crystal X-ray diffraction data (refined by WinGX [89]), are schematically shown in the upper right (the unit of the axis is lattice constant). The atomic coordinates, occupancies, and isotropic displacement parameters are summarized in Table 4.1. A sketch of typical on-centered and the off-centered potentials is also shown (lower right).

Apparent evidences for anomalous vibrations have been observed by X-ray and neutron diffraction measurements on $A_8Ga_{16}Ge_{30}$ (AGG; A=Ba, Sr and Eu) and BGSn single crystals [41, 58, 132]. A general trend has been recognized in clathrates so far that the suppression of κ increases with increasing cage size, indicating that the ionic radius of the element endohedrally residing in the larger tetrakaidecahedra (Figure 4.1) is crucial for controlling anharmonicity of the phonons. This relationship has been experimentally observed in a variety of clathrates including $Ba_8Ga_{16}Ge_{30}$ (BGG), $Sr_8Ga_{16}Ge_{30}$ (SGG) [58], and $Ba_8Ga_{16}Sn_{30}$ (BGSn) [41]. The off-center displacement of the endohedral elements, which can be used as a qualitative indicator for the strength of anharmonicity, was deduced to be 0.3Å, 0.4Å and 0.43Å for A=Sr and Eu in AGG's and *Ba* in BGSn, respectively. This is in contrast to the case of Ba in BGG, which shows an on-centered position and nearly harmonic phonons [76, 132]. Further detailed experiments on the anharmonicity of phonons have recently been made by Raman spectroscopy [135], low-T heat capacity [76] (C_p), optical conductivity [73], NMR [51, 133, 134], and ultrasonic sound [136]. Theoretically, the soft potential model (SPM), which has been introduced to glass systems [137] for interpreting the linear temperature (T) evolution of C_p, is generally employed. An additional theory based on electric dipoles has also been suggested recently [138].

In the Ge system, it has been noted that κ varies significantly between n- and p-BGGs [139]. n-BGG shows a crystal-like normal κ with a peak at a low temperature before approaching zero at T=0, while the evolution of κ in p-BGG shows a suppressed, glass-like behavior as a function of T. Similarly, BGSn shows a very large phonon anharmonicity as well as extremely low κ among clathrates, whereas $K_8Ga_8Sn_{38}$ (KGSn) displays a crystal-like behavior in κ despite a similarly large host cage structure [41, 112]. Obviously the relative size of the cage compared to the ionic radius of an encapsulated atoms (Ba^{2+}: 0.161 nm and K^{+}: 0.164 nm, refer to [140]) can merely be a qualitative indicator in the type I clathrates. Although off-centered displacement of the elements accommodated inside the cages can be a parameter indicative of anharmonicity of phonons [41, 58, 132], it is difficult to discuss the anharmonicity quantitatively.

It has been reported that the linear-T dependent phonon terms (αT) in C_p deduced from low-T C_p experiments can provide important parameters needed in order to interpret the anharmonicity of phonons quantitatively [79, 93, 141]. However, as well known in amorphous-like disordered metallic systems, the difficulties for evaluating anharmonicity of phonons using C_p arise from the fact that T-linear terms (${}^{obs}\gamma T$) of the low-T C_p include contributions from both phonons (αT) and itinerant electrons ($\gamma_e T$). In this case, we must separate the terms from each other to accurately evaluate the α values. Since these electric T-linear terms of the Sommerfeld $\gamma_e T$ are also observed in type-I clathrate systems, this becomes a very serious problem in interpreting the C_p data in the case of Ge and Sn clathrates. In order to solve the problem, we have recently demonstrated that, by using high quality single crystals with various carrier concentrations, the phonon and the electric terms can be separated successfully, and the electron-phonon interaction strength λ can also be evaluated from the effective mass (m^*) enhancement as in the case of BGG and SGG [76]. This method allows for a reliable quantitative understanding on the phonon anharmonicity in clathrate systems.

In the present work, we have made careful systematic studies on the Ge and Sn clathrates by employing the experimetal technique described above, in order to build a systematic, quantitative picture of the phonon anharmonicity in the type-I clathrates. The total linear T-dependent ${}^{obs}C_p$ is successfully evaluated for the Ge and Sn clathrates by including the phonon anharmonicity term (α T), as described by a two-level tunneling model [79, 141] where α is quantitatively proportional to the density of states of the anharmonic tunneling potential, as well as the Sommerfeld itinerant electron term ($\gamma_e T$). Detailed discussions not only on the important physical parameters of the number of anharmonic potential minima to be deduced from α but also on the electron-phonon interaction strength to be evaluated from γ_e are systematically made. The source of the phonon anharmonicity in p-BGG is also deduced from magnetic susceptibility measurements. We ascribe it to the defects on the crystallographic 6c sites, which represents a situation drastically different from that of the other type I clathrates. The contributions of phonon anharmonicity to the thermoelectric power factor will also be discussed based on the estimated values of α and m^*.

4.2 Experiment method

Single crystals of type I clathrates including n- and p-BGG, n type BGSn (n-BGSn), n type SGG (n-SGG) and n type KGSn (n-KGSn) samples were prepared by a self-flux method using Ga or Sn as introduced in chapter 2 and also as reported elsewhere [41, 83, 112, 142]. The crystal quality was checked by single crystal X-ray diffraction measurements at the BL02B2 beam port of the high-energy factory at SPring-8. n-KGSn was checked by a Rigaku R-AXIS single crystal diffractometer using MoKα radiation. Crystallographic data of n-BGSn and n-KGSn, obtained from the refinement of the single crystal X-ray diffraction data, are summarized in Table 4.1. A powder X-ray diffractometer and an electron probe micro-analyzer (EPMA) were also used to confirm the quality and the homogeneity of the crystals. The selected samples were cut into small pieces with masses from 5 to 30 mg for heat capacity measurements. The size of the samples was made as small as possible to ensure better homogeneity. Measurements were carried out from 0.36 to 3 K by using a Quantum Design physical properties measurement system (PPMS) equipped with a ^3He cryostat. After heat capacity measurements, the carrier type and the density of carriers were determined by Hall coefficient measurements of the same specimens. Magnetic susceptibilities of these samples were measured using a Quantum Design superconducting quantum interference device (SQUID) in the 2-300 K range.

TABLE 4.1: Fractional atomic coordinates, site occupancies, and isotropic atomic displacement parameters U_{eq} at 20K for n-BGSn and at 300K for n-KGSn, obtained from single crystal x-ray diffraction analyses (With wR_2 0.038 and 0.029 for the n-BGSn and the n-KGSn, respectively; and lattice parameter, 11.6653(1) Å for the n-BGSn and 11.9685(1) Å for the n-KGSn.)

atom	site	x	y	z	occupancy	U_{eq}
				n-BGSn		
Ba1	2a	0	0	0	1	0.0066(4)
Ba2	24k	0.244(7)	1/2	-0.044(9)	0.25	0.0282(8)
Ga1/Sn1	6c	1/4	0	1/2	0.68(1)/0.319(1)	0.0096(4)
Ga2/Sn2	16i	0.184(0)	0.184(0)	0.184(0)	0.344(1)/0.656(1)	0.0070(1)
Ga3/Sn3	24k	0	0.312(4)	0.118(2)	0.276(1)/0.724(1)	0.0076(7)
				n-KGSn		
K1	2a	0	0	0	1	0.0289(1)
K2	6d	0	1/2	1/4	1	0.0830(2)
Ga1/Sn1	6c	1/4	0	1/2	0.60(4)/0.40(4)	0.0173(4)
Ga2/Sn2	16i	0.182(9)	0.182(9)	0.182(9)	0.06(5)/0.94(5)	0.0147(2)
Ga3/Sn3	24k	0	0.314(1)	0.117(9)	0.14(5)/0.86(5)	0.0152(2)

4.3 Results and discussions

4.3.1 Low-T heat capacity data and its analytical approach

In order to interpret the C_p data showing anharmonicity of phonons in clathrates, we generally employ a typical analytical method, dividing the situations into the following two cases: (1) The guest on-centered clathrates (n-BGG, n-KGSn etc.) and (2) the guest off-centered clathrates (n-SGG, n-BGSn, etc.).

In the case of (1), the guest atoms accommodated in the center of the host cages are generally weakly bound to the cage constituent elements. Therefore the harmonic Einstein modes with specific oscillation frequencies of ω_E's were suggested to describe the motions of the guest atoms, in addition to the harmonic Debye modes with the density of states of $\mathrm{D}(\omega)=9\mathrm{N}\omega^2/\omega_D^3$ due to the lattice phonons of the cage. However, the excitation energies of such Einstein modes are reported [53] typically in the range of 60-110 K, higher than those of the low energy anharmonic rattling phonons created by the multi potentials inside a cage. These modes generate boson-like peaks at around $10 \sim 20K$ when C_p/T^3 is plotted as a function of T, as we described in chapter 3. Therefore, when examining C_p data at extremely low Ts (below 3K), one will find that the influences of the boson peaks associated with the Einstein modes become negligible. A typical example can clearly be seen in the case of the fundamental n-BGG type-I clathrate, where two types of Einstein modes (corresponding to the crystallographic 2a and 6d sites) are taken into consideration (Refer to chapter 3).

On the other hand, in the case of (2), the anharmonic vibrations of the guest atoms play an important role in the thermal excitation dynamics and their contribution gradually becomes dominant at low T. Such anharmonicity in phonons generally accompanied by the off-center behavior of the guest atoms is greatly evident in the larger tetrakaidecahedral cage as schematically shown in Figure 4.1, but no analytical models has thus far been able to provide a perfect quantitative description of the phonon anharmonicity. The lower right portion of Figure 4.1 schematically sketches the energy potentials created inside a tetrakaidecahedral cage. As the endohedral atoms move from an on-centered position to an off-centered position, their vibrations will change from harmonic to anharmonic.

Nowadays, anharmonic potentials as described in the former paragraph are recognized as essential for detailed data analyses in the case of clathrates. The importance of the low energy excitations (below 1K) via thermal hopping and tunneling among the local potential minima has been pointed out experimentally [73, 135] and theoretically [79, 137, 138]. The Soft Potential Model (often abbreviated as SPM) is one of the simplified models previously employed in order to describe such anharmonic potentials [137], and some empirical approaches based on SPM have recently been employed to fit the data for clathrate systems [76].

While both the free space inside the cage and the degree of off-centering of the guest atom provide good qualitative measures for phonon anharmonicity, theoretical models continue to fall short of a quantitative description. As illustrated by some past experiments [112, 136], a number of exceptions may also exist where the presence of free space inside the cage does not correlate well with anharmonicity in phonons. However, the T-linear phonon term (αT) in C_p, which can be separately obtained from the experimental ${}^{obs}\gamma T$ data, can provide important information about the density of potential minima associated with tunneling [76, 79, 141], making it a quantitatively strong measure for evaluating the phonon anharmonicity in clathrates [76]. One can refer to Appendix B for the derivation of T-linear dependent C_p (αT) due to tunneling states. Other physical parameters, such as κ and the effective mass m^*, which are strongly affected by the phonon anharmonicity, can well be correlated with the α values estimated in the present experiments as will be described later. It is noted that other experiments such as NMR [51, 134] and Seebeck coefficient measurements [58, 139] and Raman spectroscopy [135] do not provide quantitative estimates of phonon anharmonicity directly as the low T heat capacity measurements do.

In conventional metals exhibiting low phonon anharmonicity, it is generally accepted that C_p is well described at low Ts as the sum of the Sommerfeld $\gamma_e T$ term for itinerant conduction electrons and the Debye T^3 term for phonons. n-BGG can be interpreted under the same harmonic phonon framework if one additionally considers the Einstein phonon modes arising from the anomalous vibrations of atoms inside the cage as explained earlier. On the other hand, in n-SGG the effects of anharmonic phonons, associated with the anomalous vibrations of the off-center encapsulated atoms, are evident from the deviation of C_p from a harmonic crystal behavior at low energy scales [76]. We have previously reported that T-linear α values resulting in low κ in clathrates can be evaluated separately when the carrier concentration is changed [76]. In the present paper, we will apply this approach to develop a systematic, quantitative understanding of the relationship between the phonon anharmonicity and the physical properties for type I clathrates.

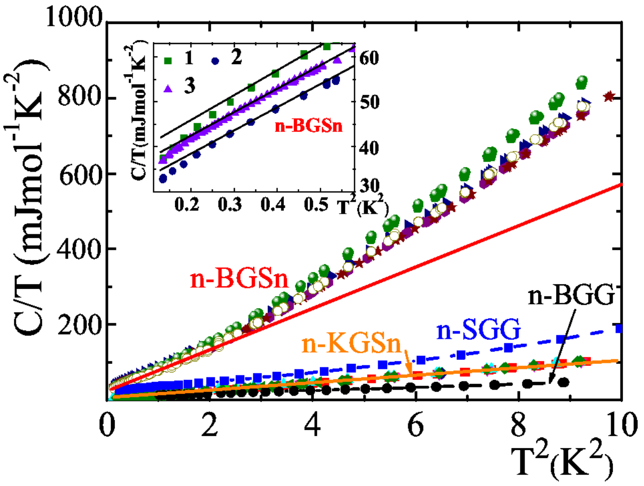

FIGURE 4.2: C_p/T-T^2 is plotted from T dependent specific heat data for n-BGG, n-SGG, n-BGSn, n-KGSn. The data for n-BGG and n-SGG are reproduced from our previous work [76]. Straight lines illustrate the linearity of the data, and the inset shows the deviation from the linear plot observed below $0.6\,K$ for n-BGSn. The data of n-BGSn was fitted below $1K$ using $C_p = {}^{obs}\gamma T + DT^3$ as described in the text. The fitting gives the parameter ${}^{obs}\gamma$.

In order to separate the electron- (γ_e) and the phonon- (α) terms in C_p we employed our previous method [76], using prepared single crystals with various carrier concentrations for p-BGG, n-KGSn and n-BGSn in order to produce a survey of various type-I clathrates complementary to the analysis of n-BGG and n-SGG reported earlier. Our experimental data on C_p for n-BGG [76] previously reported, as well as for n-KGSn prepared for the present experiments, shows good examples of harmonic potentials with an on-centered mode, and therefore a linear-T dependence of C_p/T vs. T^2 is observed in the low T regime of interest as seen in Figure 4.2. Consequently, reliable analyses of C_p data are possible at temperatures below 3 K. On the other hand, in n-BGSn the guest atoms are known to be off-centered as shown in Table 4.1, resulting in anharmonic phonons which create large deviations from the conventional harmonic solid behavior. The situation can be compared to that of n-KGSn, which shows a clear T-linear dependence from low T to high T. This is contrary to the simple assumption that its anharmonicity will be similar to that of n-BGSn based on the similar ionic radii of K^+ and Ba^{2+}. This point has also been noted in the previous work [41]. Importantly, the stoichiometry and the distribution of the elements in the host cages are largely different between n-KGSn and n-BGSn as reported previously [41, 112] and also can be seen in Table 4.1.

We tentatively applied our previous empirical approach based on the SPM analytical model, as described earlier, to the C_p data of n-BGSn, but were unfortunately unable to reach a satisfactory result. This implies that the anharmonic potential created in the Ga-Sn polyhedra of n-BGSn is somewhat different from that in Ge clathrates, and thus that the SPM we employed previously cannot well describe the anharmonic potential created in n-BGSn. Consequently, we used an alternative analytical approach by focusing on the C_p data measured at low Ts (shown in Figure 4.2) as: C_p = $(\alpha+\gamma_e)$T + DT^3+o(T^4), where the first terms are the T-linear dependent contributions of the conduction electrons (γ_e) and phonons (α) via tunneling [79, 141], the second term is the low-temperature T^3 dependent term of the Debye phonons, and the third higher order term arising from the anharmonicity of phonons, quickly approaches zero at temperatures below 1 K, as can be seen in Figure 4.2. The term for the Einstein modes appears above 3 K, as explained earlier, and has a negligibly small contribution at the low Ts considered. One can see in the following discussions that this expansion of C_p is sufficiently accurate to give a reasonable linear fitting (C_p/T vs. T^2) below 1 K.

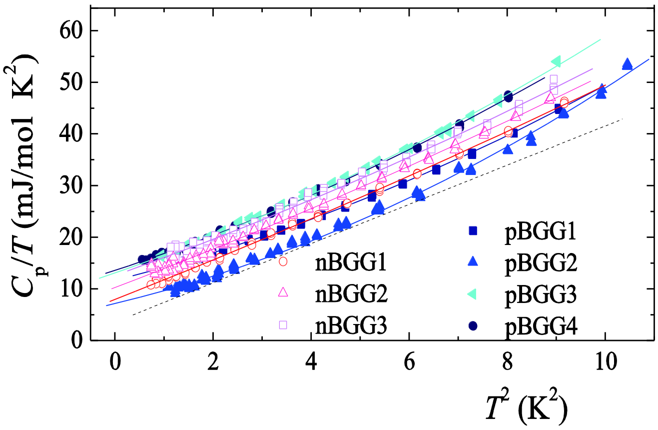

FIGURE 4.3: C_p/T-T^2 is plotted for n- and p-BGGs. The solid lines show fitting results using a high expansion in the middle temperature regime as employed for n-BGG and n-SGG in our previous paper [76]. The dashed lines serve as guides for the eyes.

The final analyses on n-BGSn and n-KGSn with various carrier numbers were made in the extremely low-T limit. On the other hand, for p-BGG showing clear but small phonon anharmonicity in C_p (shown in Figure 4.3 in comparison with that of n-BGG), the same method used previously [76] based on the SPM was applied for the data fitting. The fitting parameters ${}^{obs}\gamma$ for n-BGG, p-BGG, n-SGG, n-KGSn and n-BGSn were summarized in Figure 4.4. In the framework of a free electron model, the value of γ_e can be expressed by the equation of γ_e =

$k_B^2 m^*(3\pi^2 n)^{1/3}/(3\hbar^2)$, where k_B is the Boltzmann constant, $\hbar$ is the reduced Planck constant, m^* is the effective mass of conduction electrons, and n is the carrier number. Therefore, one can separate the phonon-associated α and the itinerant-electron γ_e terms from the experimental values ${}^{obs}\gamma=\alpha+\gamma_e$, because the former is independent of the carrier number.

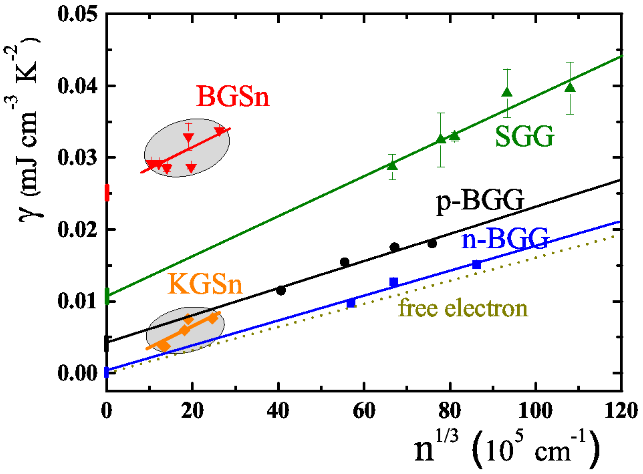

FIGURE 4.4: The ${}^{obs}\gamma$ values are shown as a function of $n^{1/3}$ for n-BGSn, n-KGSn, BGG (n and p) and n-SGG. The data of n-BGG and n-SGG refers to our other work [76]. For comparison the dotted line, calculated from free electron model, is plotted. The straight lines show a linear extrapolation of the experimental data to n=0.

Using the carrier numbers (n) obtained from the Hall coefficient measurements at 2K, we plotted the dependences of the apparent total ${}^{obs}\gamma$ values, estimated from the linear part as described earlier, on $n^{1/3}$ in Figure 4.4. The experimental data for p-BGG, n-KGSn and n-BGSn were included together with the data for n-BGG and n-SGG reported earlier. One can evaluate the α values from the intercepts by extrapolating the lines showing T-linear dependence and the γ_e values from the slopes. From α we see that n-BGSn shows the largest anharmonicity in this series of type-I clathrates, while the anharmonicity of n-KGSn is negligible. Although Ba^{2+} and K^+ cations have similar ionic radii of 0.161 nm and 0.164 nm, respectively [140], and the host cages are composed of similarly sized Ga-Sn frameworks, n-BGSn is guest off-centered and n-KGSn is on-centered [41, 112]. The present results, as well as the earlier reports, clearly indicate that the phonon anharmonicity is strongly associated with the off-centered displacement of the encapsulated elements, but the free space in the cage is not the key reason alone. It is noted that there are no good theoretical models for clathrates which quantitatively model the relationship between the structural parameters for off-center displacement of the atoms inside the cage, with regards to the phonon anharmonicity. The variation in carrier concentration of these clathrates is strongly restricted by the Zintl phase, and therefore in principle the stoichiometry cannot differ greatly from the charge-neutral composition. Although the variations in carrier number for p-BGG, n-KGSn and n-BGSn were limited to a narrower range than those of n-BGG and n-SGG (Figure 4.4), we believe that the essential statements on α and m^* described below still hold despite any minor errors caused as a result.

Because disorder of elements within the cage framework results in inhomogeneity even for single crystal clathrates, we used samples as small as possible to evaluate the intrinsic physical characteristics, as described in the experimental section. As can be seen in Table 4.2, α values were

TABLE 4.2: The values of m^*, α and the minimum density of tunneling states n_0 for the clathrates considered (See the text and also Appendix B for details). The data of n-BGG and n-SGG are included from literature [76].

Sample	$m^*(m_0)$	α $(\times 10^{-4} mJcm^{-3}K^{-2})$	n_0 unit cell^{-1}
n-BGG	1.01±0.25	10.6±5.3	0.0006±0.0003
p-BGG	1.20±0.19	42.4±18.6	0.0024±0.0011
n-SGG	1.68±0.24	135.4±20.1	0.0074±0.0011
n-KGSn	1.86±0.54	2.8±5.6	0.0002±0.0004
n-BGSn	2.05±0.48	246.8±15.6	0.0175±0.0011

estimated from the intercepts in Figure 4.4. From these α values, one can estimate the density of potential minima by employing either the tunneling model introduced by Anderson, or the model introduced by Nakayama. In Anderson's model, α =$(1/6)\pi^2 \mathrm{k}_B^2 P_0$, where P$_0$ denotes the density of states (DOS) of tunneling states (See Appendix B for more details). The Sommerfeld γ_e can also be estimated from the slope of the plots in Figure 4.4, and from this m^* was deduced and the values are listed in Table 4.2. It is shown later that both the thermal conductivities and the electron-phonon interaction strengths are quantitatively in good agreement with the α parameters deduced from the present experiments.

4.3.2 Measurement-time dependent heat capacity

One intriguing point in the C_p/T vs. T^2 plot is the fact that a small but unambiguously evident deviation from the linear fitting can be observed in the experimental plots below ca. $0.6K$, as shown in the inset of Figure 4.2. This phenomenon is frequently seen in amorphous materials [143]. A similar deviation can also be observed within experimental accuracy for n-SGG, although the deviation is much smaller than the present case of n-BGSn as shown in Figure 4.5 (a) and (b). We exclude the influence from the background signal of the measurement by comparing the data of a sample (BGSn) and the addenda as shown in Figure 4.5 (d). The addenda shows a rather weak influence to the measurement result, and the nonlinear behavior should be an intrinsic property of the sample.

In general, two possible reasons for such a deviation should be considered : (1) unexpected long-time relaxation between the two potential minima in the tunneling model [143] or (2) "Kapitza resistance/thermal boundary resistance" [144] as documented in the PPMS manual [145]. However, given that we did not observe a similar deviation at low T for any other clathrate compounds with on-centered guest atoms, such as n-KGSn shown in Figure 4.5 (c), the first explanation seems more likely.

According to the PPMS manual, our samples were further checked by changing the measurement time from 1 time-constant up to 6 time-constants as shown in Figure 4.6 (a) (the time constant is determined by the temperature rise of the sample in measurement: See PPMS manual for more details). Different from the situation in the PPMS manual [145], which shows a disappearance of the linear deviation by applying 2 time-constants for the measurement time, the nonlinear

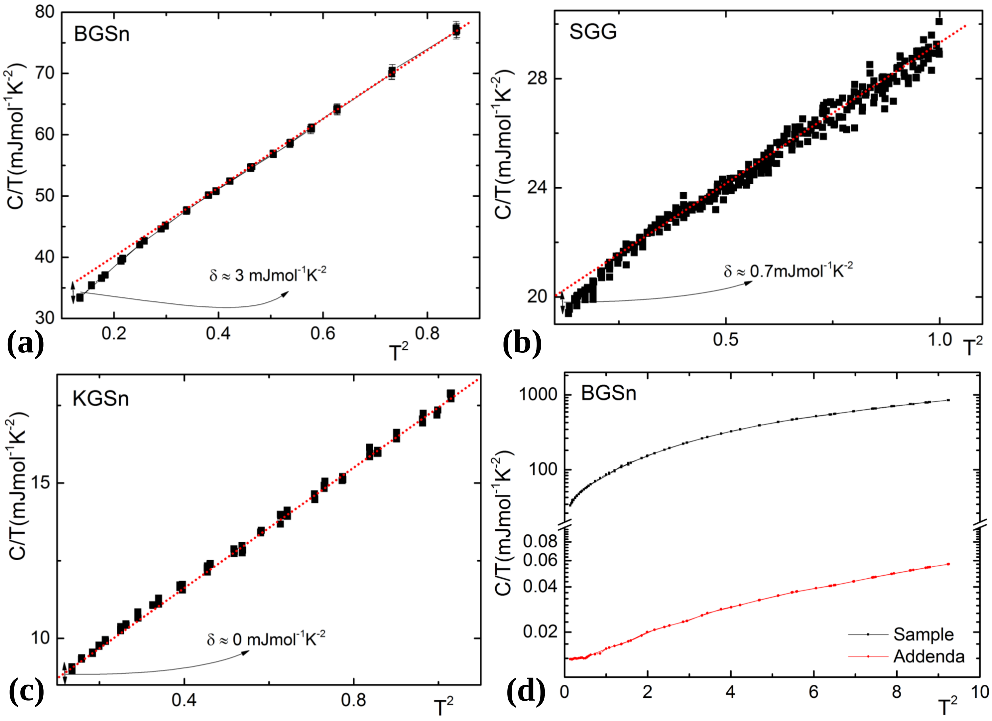

FIGURE 4.5: T-nonlinear dependency of the heat capacity of tunneling states below 0.6 K. (a) The deviation of the linear fitting from the experiment data (δ) is about 3 mJmol^{-1}K^{-2} for BGSn at 0.36 K. (b) The δ is about 0.7 mJmol^{-1}K^{-2} for SGG at 0.36 K. (c) The δ is zero for KGSn. (d) A comparison between the measurement data of a BGSn sample and the background addenda. The nonlinear behavior can not be attributed to the addenda.

behavior still exists in our experiment even under a measurement time of 6 time-constants. The situation can also be revealed in Figure 4.6 (b), where the red symbols can not go back to the linear line even under a long-time measurement. However the influence of the measurement time is obvious and can not be ignored as shown in fig. 4.6 (c). It seems that heat capacity increases as measurement time increases, and a relationship between C/T and the actual measurement time (t) is shown in Figure 4.6 (d).

According to the standard tunneling model [79, 146], an approximation for $C_{TS}(T,t)$ is derived as:

$$C_{TS}(T,t) \approx \frac{\pi^2}{12} k_B^2 T P_0 \ln(66.24 A T^3 t) \tag{4.1}$$

where A is a constant and the other parameters can be found in the Appendix B. Based on eq. (4.1), the data shown in fig. 4.6 (d) are fitted by a natural logarithm function. The good fitting indicates that the time-dependent model, applied for amorphous solids, works well for BGSn compounds.

4.3.3 Phonon anharmonicity and the inner space of the cage

As discussed, the anharmonicity of phonons is generated by anomalous motions of the encapsulated atoms, and therefore the free space of the cage is a very important factor in determining the anharmonicity of phonons. This situation has been confirmed by a number of studies on clathrates [41, 135]. It is quantitatively shown in the present studies that α of n-KGSn is not

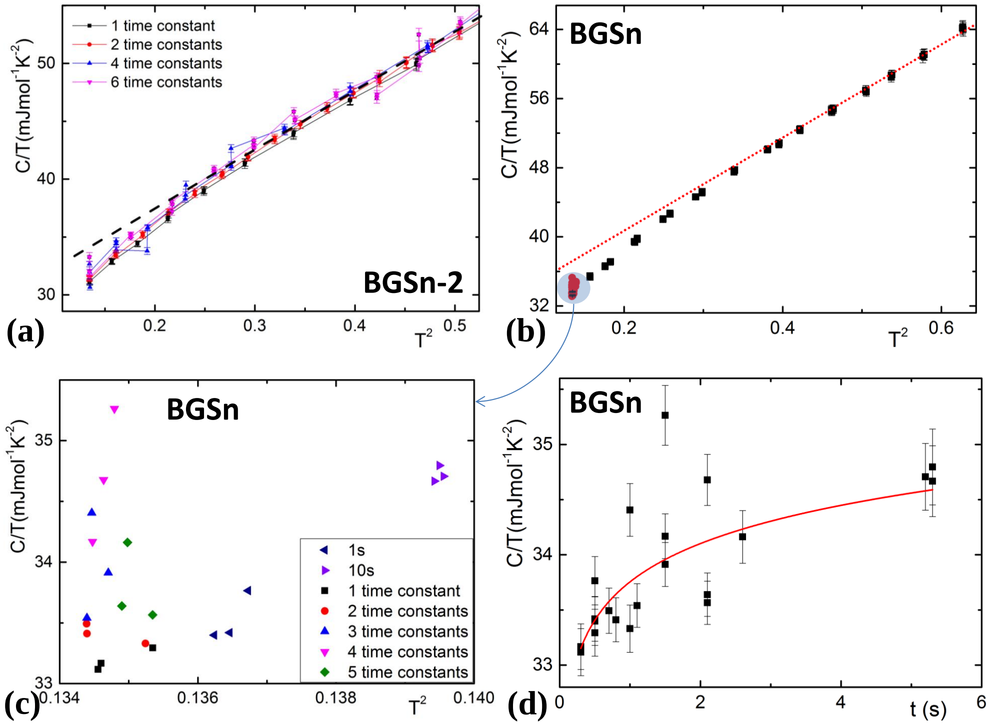

FIGURE 4.6: Measurement-time dependent heat capacity of tunneling states. (a) Heat capacity measurement with different measurement times for a BGSn sample. The linear deviation still exists even for long-time measurement. (b) This figure is consistent with fig. 4.5 (a). The measurement data at around 0.36 K with different measurement times are shown by red symbols and enlarged in the figure (c). (d) The relationship between C/T and the actual measurement time (t).

as large as that of n-BGSn, although the ionic radii of the endohedral atoms as well as the size of the Ga-Sn cage are similar to each other. In addition, it has been pointed out that p-BGG exhibits a larger anharmonicity than n-BGG, although the crystal structures of both BGG clathrates are not dissimilar with each other. In order to understand this point more clearly, the relationship between α, κ_L (κ_L's at 20 K are taken from references [41, 58, 112]) and the free space in the tetrakaidecahedron cages (R_{free}), is shown in Figure 4.7. R_{free} is calculated using a similar method to previous reports [41], although our definition varies slightly. In the previous work [41], the cage radius (R$_{cage}$) has been defined as the distance between the 6d guest site and the 24k host sites, which are not on the hexagonal cells. In the present manuscript, we used the average distance in the three dimension between 24k and 6d sites as R$_{cage}$. This was made because the 24k sites of the larger tetrakaidecahedron above and below the guest atoms are located at the corners of hexagon cells, and importantly the distance between two hexagons is much smaller than the size of the other two dimensions inside the cage and thus the atoms on the hexagonal cells also create a limit on the free space. We used the following values for our calculations: $R_{\mathrm{cage}}(\mathrm{SGG}) = 3.664$ Å and $a(\mathrm{SGG}) = 10.724$ Å (reference [54]). For r_{guest}, we chose the ionic radii of the guest atom in a high coordination environment: $r_{\mathrm{Sr}} = 1.44$ Å, $r_{\mathrm{Ba}} = 1.61$ Å and $r_{\mathrm{K}} = 1.64$ Å [140]. It should be noted that, we didn't use van der Waals radii for r_{guest} as we did in chapter 3, because it is more convenient to compare with previous works, and van der Waals radii give a same conclusion. The average covalent radii of the atoms forming the host cage were used for r_{host}: $r_{\mathrm{Ge}} = 1.22$ Å, $r_{\mathrm{Sn}} = 1.41$ Å and $r_{\mathrm{Ga}} = 1.26$ Å. In the case of the cage consisting of both Ga and Ge, r_{host} was assumed to be $r_{\mathrm{Ge}} = 1.22$ Å, as covalent radii of Ga and Ge are not dissimilar. For the Ga-Sn host cage, the average covalent radius was calculated as r_{host} according to the site occupancies shown in Table 4.1. For general reference we also listed the values used in the previous report [41], in the figure captions. It is important to note that the final conclusion does not change, regardless of which evaluation method for R_{free} is used.

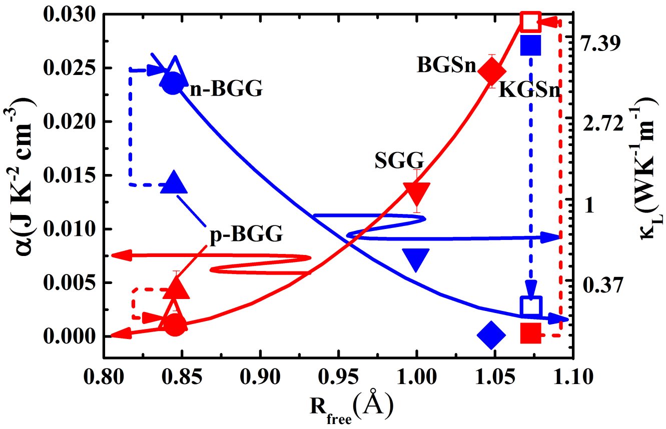

Figure 4.7: The α (due to tunneling states) and the κ_L(the data at $20K$, taken from references [41, 58, 112]) values are plotted vs. R_{free} for different types of clathrates. Different markers correspond to each clathrate. Circles: n-BGG, up-triangles: p-BGG, down-triangles n-SGG, diamonds: n-BGSn, and squares: n-KGSn. The closed marks are from the experiment data, while the open ones are sketched to illustrate the exceptional case of p-BGG and n-KGSn, which do not match the blue and red trend curves (the curves serve as guides for the eyes). R_{free} was evaluated as described in the text. For reference, the R_{free} values evaluated in the previous report [41] are listed: 1.34 Å for n- and p-BGG, 1.49 Å for n-SGG, 1.51 Å for n-BGSn and 1.61 Å for n-KGSn.

Although both α and κ_L seem to vary regularly with R_{free} (Figure 4.7), some of clathrates, such as n-KGSn and p-BGG, show large deviations from the general trend observed. One of the most likely comprehensive explanations would be that the anharmonic potentials inside the host cage may be created by the rearrangement of Ga residing in the cage structure, as has been suggested in an earlier study [83, 112]. This explains the harmonic potential of n-KGSn if we assume that the Ga atoms in n-KGSn reside in higher symmetry positions than those in n-BGSn. This might be caused by the weaker covalent interactions of Ga with alkali metals than those with alkaline earth metals. The geometrical symmetry of Ga atoms residing on the cage and the off-centered displacement of the accommodated atoms should be closely associated with how strongly Ga^- interacts covalently with either Ba^{2+} or K^+. In the case of p-BGG, the reason for the deviation is somewhat different. We note firstly that a large number of defects have been observed in p-BGG by X-ray diffraction [132] and NMR spectroscopy [51]. The situation can be seen more definitely by the temperature dependent magnetic susceptibilities of various n- and p- BGGs shown in Figure 4.8.

All samples in the present research show diamagnetic susceptibilities due to the large diamagnetic terms associated with Landau core-diamagnetism [62, 147]. While recent crystallographic studies on BGSn (both n and p type) have also reported the presence of defects [148], it is apparent that the susceptibilities of n-BGSn, n-KGSn and n-BGG are nearly temperature independent, while p-BGG shows an extremely strong Curie paramagnetic behavior. Assuming the smallest possible spins (S=1/2) to be magnetically detectable, a defect spin number of (0.0062 ± 0.0001)/lattice was estimated for p-BGG samples. A similar phenomenon in Ba_8Ge_{43} reported by our earlier

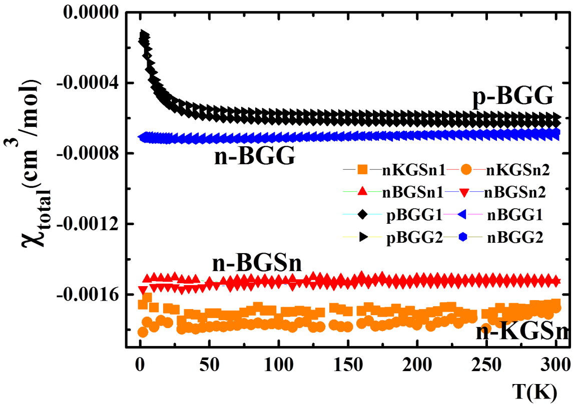

FIGURE 4.8: The magnetic susceptibility of n-BGSn, n-KGSn, and n- and p-BGGs.

studies [62] also suggests that unpaired spins can arise from the defects in the host cage. Our estimate from the magnetic measurements provides a lower bound on the number of defect spins, due to the fact that the formation of non-magnetic nonbonding orbitals at the 6c site in a lattice creates defects that can be magnetically-silent electron pairs involving the electrons donated by the Ba atoms [62]. The local position of these defects on the Ga-Ge cage structure will lead to a lower symmetry, showing potentials with stronger anharmonicity. Therefore, the geometry of the host cage structure can be the key to understand the origin of the anharmonic potentials in type-I clathrates and strongly modified during the crystal growth.

Taking into account the above description on the anharmonic potentials in the host cage structure, they could be greatly influenced by the interactions between the positively-charged accommodated atoms and the negatively-charged Ga atoms in the host cage. Similarly, the defects in the cage will also exert a large influence on the cage rearrangement. It would be very reasonable to think that the cage structure can be strongly modulated via such interactions between the cationic guest elements and the anionic Ga atoms residing on the cage or via the vacancies existing on the cage. Photoemission spectroscopy [83], NMR [51], and combined X-ray and neutron diffraction studies [148] have highlighted this point.

We will now quantitatively discuss the density of anharmonic potential minima within the framework of Anderson's tunneling model in a two-level system, using the α values determined in the present study. The density of states of the potential minima P_0 can quantitatively be related to the α values by $\mathrm{P}_0 = 6\alpha\ /(\pi^2 k_B^2)$ (Refer to Appendix B). By using our experimental values of α, the values of P_0 were calculated to be 7.9 ± 0.5 for n-BGSn, 4.33 ± 0.64 for n-SGG, 1.36 ± 0.6 for p-BGG, 0.34 ± 0.17 for n-BGG and 0.09 ± 0.18 for n-KGSn in the unit of $\times 10^{34} mJ^{-1}cm^{-3}$. According to Anderson, P_0 is assumed to be constant from the zero energy $\varepsilon = 0$ to at least the cut-off energy generally around ϵ=10 K (See Appendix B for more details). By applying the cut-off energy, we can obtain the minimum number of the potential minima per volume n_0 to be 10.9 ± 0.7 for n-BGSn, 6.0 ± 0.9 for n-SGG, 1.9 ± 0.8 for p-BGG, 0.47 ± 0.24 for n-BGG and 0.12 ± 0.24 for n-KGSn in the unit of $\times 10^{15} cm^{-3}$. These values were converted to the values per unit cell, and we listed them in Table 4.2. It is noted that the estimated number of the tunneling states is very close to the number of defects evaluated by the temperature dependent magnetic susceptibility for p-BGG. The important message given by these quantitative analyses is that the evaluated values are extremely small considering the six tetrakidecahedral cages in a lattice. A similar comment can also be found in the original paper by Anderson et al. [79] in a glass system, where the number of the calculated potential minima is found to be much smaller than expected from the number of oxygen atoms liberated in amorphous silica. In the framework of Anderson's two level system (TLS) based on Schottky heat capacity (Refer to Appendix B), asymmetric two potential minima as well as a moderate barrier hight between them are responsible for the linear-T dependence of C_p. Therefore, the contributions of the potential minima with equivalent or quasi-equivalent energy levels are not fully involved in the evaluation. Due to the high symmetry of the host cage structure, we expect a large number of potential minima with equivalent energy levels to be created in the type-I clathrates. This could be one of the important reasons that a much smaller number of potential minima than an the expectation ones were evaluated by Anderson's TLS model.

4.3.4 Phonon anharmonicity and physical parameters

In order to illustrate the influences of the anharmonicity of phonons on physical parameters, the relationship between lattice thermal conductivity κ_L, α, and m^* is depicted as a three dimensional plot in Figure 4.9. The values of α and m^* are shown in Table 4.2. A quantitatively strong dependence of m^* on α is seen in the data, as illustrated by the blue dashed line. In the case of clathrates, electron correlation is weak and the system can be categorized as an electron-phonon (e-ph) system, where the enhancement of m^* can be described by the e-ph interaction parameter [149] λ: $m^* = m_0(1 + \lambda_{e-ph} + \lambda_s)$, where, λ_{e-ph} is the e-ph term and λ_s is the spin fluctuations associated with the quasi-particle mass enhancement [150]. The last term is considered to be less important for clathrates in the present work and therefore the phonon anharmonicity might exert a large influence on m^*. When off-centered anharmonic potentials are created as shown in Figure 4.1, strong anharmonicity, due to the oscillatory anomalous motions of the atoms inside the cage, will be provided to the harmonic lattice phonons. Such phonon anharmonicity is considered to exert a large influence on the electron-phonon coupling strength via the scattering between the less-dispersive phonons lying low in energy, lattice acoustic phonons and conduction electrons. This is consistent with a recent NMR study on BGSn [134]. At the same time, the accommodated atoms show a quantum tunneling phenomena among the anharmonic potential minima created inside the cage, indicated by the αT term of C_p. Consequently it is reasonable that both m^* and α correlate strongly with phonon anharmonicity, as illustrated in Figure 4.9

It has already been discussed that κ_L can be suppressed efficiently by the phonon anharmonicity via the scattering of acoustic phonons, and this can be well supported by the good correlations between κ_L and α in Figure 4.9. In this discussion we used the κ_L values estimated at 20 K, taken from references [41, 58, 112]. It is noted that the results obtained below 1K, by using T linear analyses in the present paper, is consistent with the results obtained from higher temperatures analyses by including higher order T terms as reported previously [76]. This indicates that the phonon anharmonicity does not change greatly from low temperatures to the higher temperatures. The diffraction measurements have also pointed out that the off-center behavior of the guest atoms inside the large cages holds in a similar fashion from low to higher temperatures [148]. This suggests that the anharmonic potentials created in type I clathrates are very different from what can be observed in type III clathrates such as $Ba_{25}Ge_{100}$, in the latter case, one can see a large change in the thermal vibrational motions of the guest atoms [82]. Although the strength of

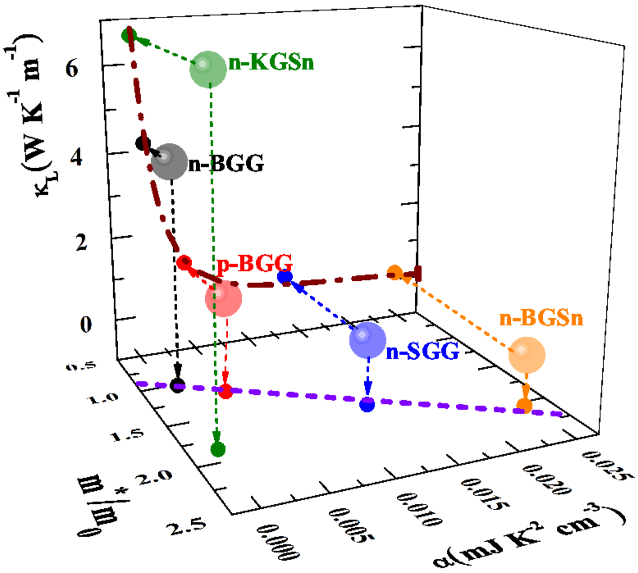

FIGURE 4.9: A three dimensional figure showing the relationship between α, κ_L (the data at $20K$ are taken from references [41, 58, 112]), and m^*. The dash-dotted and dashed curves serve as guides for the eyes.

phonon anharmonicity, indicated by α, is estimated below a few Kelvin in the present experiments, the discussion on the anharmonic potentials could be valid to relatively high temperatures, for example at $20K$.

4.3.5 Effective mass and thermoelectric parameters

As described in the present paper, thermoelectric clathrates are categorized as a electron-phonon system having relatively strong e-ph interactions compared to conventional materials. Consequently, when one considers the thermoelectric power factor of $P = S^2\sigma$ (the electronic part of ZT), where $P = \frac{(\pi^{4/3} k_B^4 T^2 \mu (m^*)^2)}{(3^{4/3} e \hbar^4 n^{1/3})}$ with the carrier mobility of μ in the framework of an effective mass approximation, ZT will be influenced by the square of m^*. Keeping in mind, however, that m^* and μ are typically not independent of one other, this enhancement by m^* is an upper limit estimate for an e-ph system. Furthermore, it is noted that this discussion is only valid for a specific metallic regime in clathrates with $\kappa_L \gg \kappa_e$. When the carrier number n becomes very small, the clathrates generally undergo a metal-semiconductor transition. On the other hand, if the carrier concentration becomes very large, a break down of the important thermoelectric condition in clathrates $\kappa_e \gg \kappa_L$ occurs.

4.4 Summary

In order to understand the anharmonicity of phonons in clathrates and the e-ph interactions, a systematic study on type I clathrates was made using low-T heat capacity. The total linear-T terms at low T in $C_{\rm p}$ were successfully separated into two parts: the anharmonic phonon $\alpha\,$T and the electronic γ_eT terms, and m^*'s were evaluated from the γ_e values. The nature of anharmonic phonons was quantitatively discussed by employing the α values determined in the present experiments. Defects are experimentally shown to play an important role in the caes of p-BGG, the situation of which is different from that of other clathrates. Based on the quantitative discussion in the present work, the rearrangement of Ga^- residing on the host cage and the defects created in the host cage frameworks, which are sensitive to the interactions with the guest rattlers, were identified as the key factor in determining the anharmonic potentials in clathrates.

Chapter 5

Thermoelectric Properties of Transition Metal Containing Clathrate

Our discussions so far in chapter 3 and chapter 4 were mainly emphasized on the rattling phenomena and the associated phonon properties in type-I clathrates. In this chapter, both thermal and electrical properties will be discussed on a basis of the thermoelectric performance of the rattling-system.

A Brief Abstract

Single crystals of the noble metal containing clathrates, $Ba_8M_{5.3}Ge_{40.7}$ (M = Cu, Ag, Au), are synthesized by using a Sn-flux method. The crystals are checked by X-ray single-crystal and powder diffraction measurements as well as SEM-EDS measurements, and the data analyses show that a small amount Sn, around 1 atom per unit cell, is included in the crystal. The crystal quality is also confirmed by the high electrical mobility of these compounds, especially Cu containing clathrates, which show a value of 18.5 cm^2/Vs at 300 K. Both Hall resistivity and Seebeck coefficient (S) measurements show that all the flux-grown compounds are n-type(electron-type). The "phonon-glass electron-crystal" (PGEC) concept is revealed by the high electrical conductivity (σ) and low thermal conductivity (κ) of the single crystals. The rattling phonon modes are detected by heat capacity measurements, and they they play a key role in the PGEC concept, as on one hand they suppress the heat conduction, while on the other hand exert little influence on electrical conduction. Our discussion, based on the carrier concentration as well as carrier mobility dependent thermoelectric parameters (S, σ and PF), show that single crystal is favored for achieving high thermoelectric performance in clathrate-system.

5.1 Introduction

Intermetallic clathrates are classified as a type of the conceptual "phonon-glass electron-crystal" (PGEC) materials [3] and have been widely studied for thermoelectric applications [3, 25, 151]. A detailed introduction of clathrates, including the structure, formation and physical properties can be found in chapter 1. In the clathrate family, type-I clathrate is most widely concerned due to its stability and the variety of species. The most striking point in type-I clathrate is the rattling phonon modes of the guest atoms, because they can suppress heat conduction efficiently while exert little influence on electrical conduction. Therefore, it is the rattlers that enable clathrates to be a candidate of PGEC-compound. Discussions concerning rattling phonons have been made in details in chapter 3 and chapter 4.

However only rattling phonons do not guarantee clathrate a good thermoelectric material, the thermoelectric performance, which is expressed by the figure of merit, $ZT = \frac{S^2\sigma}{\kappa}T$, still needs to be optimized for real applications. Here S, σ and κ stand for Seebeck coefficient, electrical conductivity and thermal conductivity, respectively. Although the highest ZT reported in type-I clathrates is 1.35 at 900 K ($Ba_8Ga_{16}Ge_{30}$) [25], most clathrates show ZT values below 0.5. On phonon aspect, κ can be further lowered by increasing the anharmonicity of the rattling motions, the typical examples are $Ba_8Ga_{16}Sn_{30}$ (BGSn), $Sr_8Ga_{16}Ge_{30}$ (SGG) and p type $Ba_8Ga_{16}Ge_{30}$ (BGG) [41, 75, 84, 95]. It is noted that nano-structuring, widely applied in other systems for suppressing heat conduction [16–18], does not work well in clathrate system [152], in another word, phonon scattering due to rattling phonons is dominant in the scattering process.

On electron aspect, the most common optimization way is via tuning carrier concentration (n), because S, σ and the thermal conductivity contributed from electrons (κ_e) are all strongly dependent on n, as described in chapter 1. The Zintl phase concept provides an access to modify carrier density by deviating the stoichiometric ratio of component elements. Electrical properties can also be modified by changing carrier mobility (μ) and effective mass (m^*), etc. [111]. Provided a perfect crystal, the electrical parameters in ZT: S, σ and κ_e are basically determined by the electronic band structures, where the information of n, μ and m^* is included. It is expected in type-I clathrate that the electronic band characters can be modified by substituting the cage atoms with transition metal elements (TM), and it has been widely tested [53, 107, 111, 151, 152]. The highest ZT achieved in TM containing clathrates is 1.2 at 1000 K [151], slightly smaller than the highest value in BGG. It has been reported that, comparing with Ga-substitution (in the case of BGG), TM-substitution could reduce the disorder of cage atoms and lead to a relatively high carrier mobility [153]. A simple comparison concerning the disorder of cage atoms between TM-clathrate and Ga-clathrate can be described as follows. We take $Ba_8Cu_{5.3}Ge_{40.7}$ (BCG) and BGG as examples. In the case of $Ba_8Cu_{5.3}Ge_{40.7}$ (BCG), the 6c sites (Figure 1.7) are occupied by 5.3 Cu and 0.7 Ge, while 16i and 24k sites are occupied only by Ge atoms [107], on the other hand, in the case of BGG, 6c, 16i and 24k sites are occupied by both Ga and Ge atoms, respectively. It is obvious that the cage of BCG is more ordered than that of BGG. Taking the above descriptions into account, in order to maximize the ZT in clathrate system, TM-substitution is an important approach.

Noble metal containing clathrates, $Ba_8M_{5.3}Ge_{40.7}$ (BMG: M = Cu, Ag, Au), are of great interest among TM-clathrates [107, 152, 154–159] because of their stability and the adjustable solubility of M. The maximum solubility of M is close to the number of 6c sites, and therefore BMG is expected to have a relatively ordered cage framework and high electrical mobility. However, most reported BMG are poly-crystals and the grain boundaries limit the carrier mobility and thus limit the thermoelectric performance via $ZT \propto \frac{m^{*3/2}\mu}{\kappa_L}T$ [3]. Only $Ba_8Au_{5.3}Ge_{40.7}$ (BAuG) single crystals grown by the Bridgeman method have been reported [152]. The difficult point for growing a BMG single crystal is that the useful self-flux method, successfully applied for BGG, SGG, BGSn, etc., can not be used, because none of the component elements could serve as a flux. In the present research, for the first time, we grow BMG single crystals by using a simple Sn-flux method. The grown single crystals are characterized by SEM-EDS measurements, X-ray diffraction measurements and physical properties measurements, and The crystal structures, physical properties and thermoelectric properties will be discussed based on the experimental data. We will especially focus on the carrier density and mobility dependent thermoelectric properties, and come to the conclusion that high quality single crystal is more favored for achieving high thermoelectric performance in clathrate system.

5.2 Experiment method

The basic principles of experiment were given in chapter 2. This section only describes how each experiment is conducted.

5.2.1 Crystal growth with flux method

According to chapter 2, single crystals of BMG are grown out of Sn/In/Bi fluxes by following a specially designed temperature sequence (table 2.1). In this dissertation, we only focus on Sn-flux and leave In- and Bi- fluxes without further discussions. There are generally two approaches in our experiment: a two-step process and a one-step direct process. In the former case, poly-crystals of BMG are synthesized by a RF-induction furnace as the first step and then single crystals are grown out of the mixture of the poly-crystals and Sn-flux at appropriate temperatures (table 2.1). In the latter case, stoichiometric amount of Ba, M and Ge and an excess amount of Sn are directly mixed and sealed in a quartz tube, and single crystals are grown by following a same temperature sequence mentioned above. It is noted that the grown crystals using the two methods are not dissimilar to each other, however we prefer the one-step process because the two-step process consumes more Ba due to oxidation. Our collaborators J. Xu *et al.* have made a study on the BCG compounds grown from the two-step process [160], so we mainly focus on the one-step process in this chapter. The grown single crystals of BMG are shown in Figure 5.1

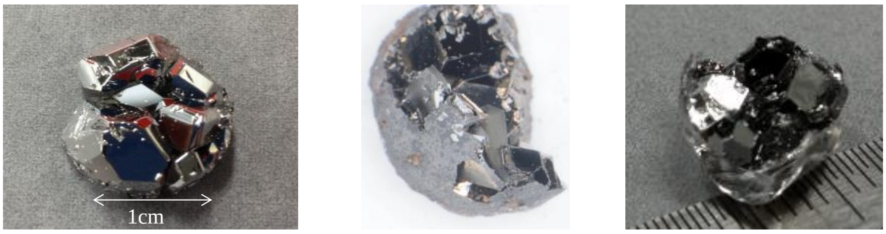

$Ba_8Cu_{5.3}Ge_{40.7}$ +Sn-flux

$Ba_8Ag_{5.3}Ge_{40.7}$ +Sn-flux

$Ba_8Au_{5.3}Ge_{40.7}$ +Sn-flux

FIGURE 5.1: The grown single crystals of noble metal containing clathrates, BMG, where M = Cu, Ag, Au.

5.2.2 Microstructure Analysis

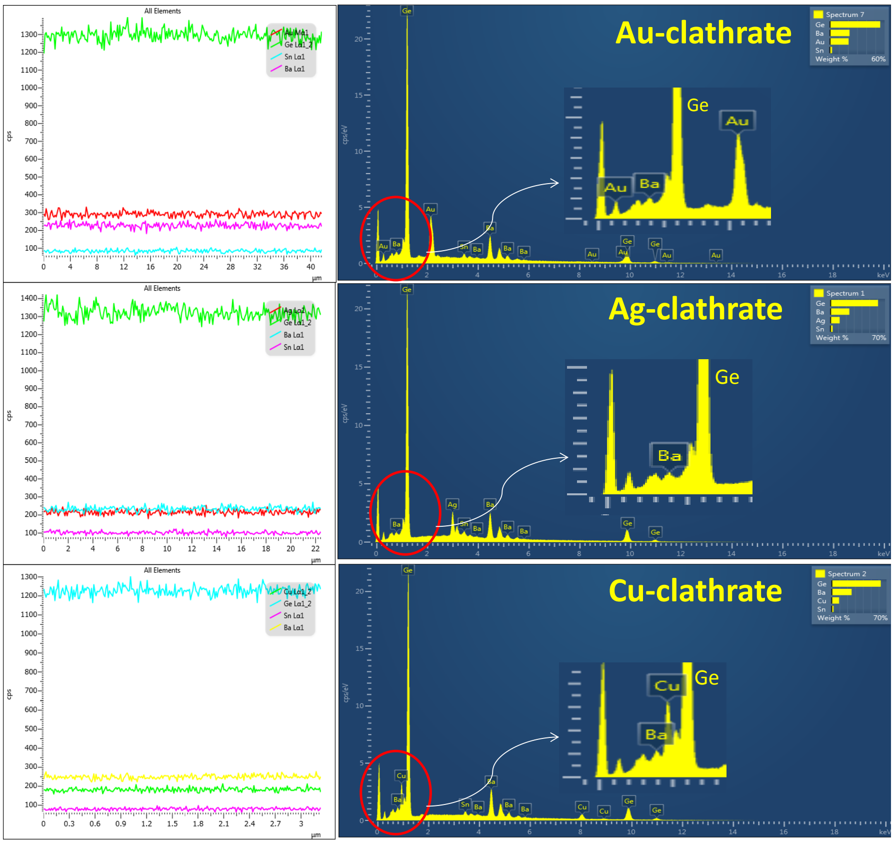

FIGURE 5.2: The EDS spectra of noble metal containing clathrates, BMG.

The crystal quality and homogeneity were checked by SEM-EDS measurements as described in chapter 2. Figure 5.2 shows the line-scan results and the EDS spectra of BMG. A small amount of Sn is observed, and it is homogeneously distributed in the crystals. We will confirm that Sn is not a impurity but a component element by using X-ray diffraction measurements. The uniform intensities of different elements along a scanned line indicate that the single crystals are of good quality. The composition ratios can be derived from the EDS spectra and they will be discussed later on.

5.2.3 X-ray diffraction measurement

The crystal quality was confirmed by using both X-ray powder and single crystal diffraction measurements. Detailed description of the facilities as well as the measurement process can be found in chapter 2. The X-ray powder diffraction patterns of BMG are shown in Figure 5.3. The data analyses reveal that the grown crystals are single phase and homogenous. It is noted that no Sn impurity peak is observed, in another words, the Sn, detected by EDS, is one component of the compounds. Single crystal X-ray diffraction measurements on selected small single crystals of BMG show beautiful diffraction spots. Data analyses as well as the derived crystal structure information will be given in the next section.

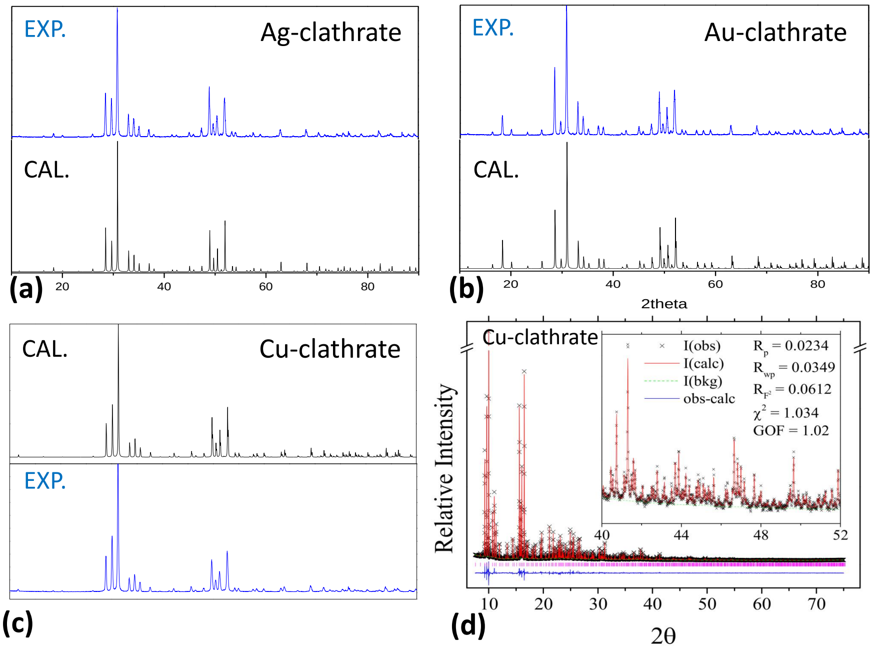

FIGURE 5.3: The X-ray powder diffraction patterns of noble metal containing clathrates, BMG. (a)-(c) A comparison between experimental data and theoretical calculations for Ag, Au and Cu containing clathrates, respectively. The experiment data were collected by using Rigaku SmartLab X-ray diffractometer. (d) The X-ray diffraction pattern of BCG, collected by using the synchrotron radiation facility at SPring-8 and analyzed by using the Rietveld method within the GSAS package [160].

5.2.4 Physical properties measurement

Heat capacity measurements were carrier out on selected compounds of BMG with mass ranging from 10 mg to 40 mg from 0.36 K to 70 K by using PPMS equipped with a ^{3}He cryostat. Electrical resistivity and Hall resistivity were measured on the same specimen by using the resistivity option of PPMS from 2 K to 300 K. For Hall resistivity measurement, the magnetic field is scanned from -9 T to 9 T or from 9 T to -9 T and the sample is polished to be thinner than 0.2 mm. Carrier density and mobility can be derived from the electrical transport measurements. Thermoelectric properties were measured by using the thermal transport option (TTO) of PPMS from 2 K to 350 K. For convience, two-probe method was applied for measurements. Although the thermal contact resistance does not exert big influences on thermal conductivity measurement, because BMG compounds have very high thermal resistivity, the electrical contact resistance exerts huge influences on electrical conductivity measurement. In order to correct the electrical resistivity, it was measured again by using a four-probe method via the resistivity option of PPMS at the same temperature range.

5.3 Results and Discussion

5.3.1 Chemical Composition and Crystal Structure

According to the EDS spectra shown in Figure 5.2, the unit cell formulas of BMG are derived to be: $Ba_8Au_{5.3}Ge_{39.2}Sn_{1.1}$, $Ba_8Ag_{5.0}Ge_{39.5}Sn_{1.1}$ and $Ba_8Cu_{6.4}Ge_{38.5}Sn_{0.9}$ for BAuG, BAgG and BCG, respectively. For BAuG and BAgG, the formulas are reasonable as they are consistent with the n-type carriers, which are determined by Hall resistivity measurements and Seebeck coefficient measurements. However the formula for BCG is not reasonable, as according to Zintl phase, 6.4 Cu in one unit cell would lead to a p-type compound, but experiment data show that BCG is an electron-type compound (we shall see it later on). In order to clarify the discrepancy, we synthesized several poly-crystals of BCG with the amount of Cu ranging from 4.5 to 6 in one unit cell. The poly-crystals are checked by X-ray powder diffraction measurements as well as EDS measurements. The nominal compositions and the compositions determined by EDS measurements are listed in Table 5.1. It is clear that there is an error in determining the amount of Cu in BCG by using the EDS spectra and the analytical method provided. The most possible reason of the error may come from the overlap of Cu peaks with the peaks of other elements in EDS spectra. This situation can be revealed in Figure 5.2, where Cu L_α peak is overlapped with Ba M and Ge L_α peaks at around 1 KeV. In the case of BAuG and BAgG, Au/Ag peaks do not overlap with other peaks, and therefore a better estimation can be achieved. By careful analyses, the formula of BCG are finally determined to be $Ba_8Cu_{5.1}Ge_{40.2}Sn_{0.7}$ [160], which is consistent with the WDS results reported else where [161].

TABLE 5.1: The nominal compositions and the compositions determined by EDS measurement for poly-crystalline compounds of BCG.

	Ba	Cu	Ge
nominal (1)	8	4.5	41.5
EDS (1)	8	6.1	39.9
nominal (2)	8	5	41
EDS (2)	8	6.2	39.8
nominal (3)	8	5.3	40.7
EDS (3)	8	6.3	39.5
nominal (4)	8	6	40
EDS (4)	8	6.4	39.6

The X-ray single crystal diffraction data were analyzed by using WinGX program [89], and the atomic parameters of BMG are shown from Tables 5.2 to 5.4 for BCG, BAgG and BAuG, respectively. The BCG single crystal grown by a two-step process gives a similar result [160]. According to the atomic occupancies shown in the tables, the unit cell formula are derived to be: $Ba_8Cu_{3.84}Ge_{41.75}Sn_{0.41}$, $Ba_8Ag_{4.98}Ge_{40.04}Sn_{0.98}$ and $Ba_8Au_{5.25}Ge_{39.77}Sn_{0.98}$ for BCG, BAgG and BAuG, respectively. The results of BAgG and BAuG are consistent with the EDS results, while the result of BCG is very different from the EDS result. We ascribe the discrepancy to

Table 5.2: Fractional atomic coordinates, site occupancies, and isotropic (U_{eq}) and anisotropic (U_{ij}) atomic displacement parameters at RT for BCG, obtained from single crystal x-ray diffraction analyses (With residuals: R = 0.023 for all data and wR_2 = 0.042 and a lattice parameter: a = 10.7456(8).)

atom	site	x	y	z	occupancy	U_{eq}
Ba1	2a	0.000	0.000	0.000	1	0.0089(3)
Ba2	6d	0.250	0.500	0.000	1	0.0350(3)
Cu1/Ge1	6c	0.500	0.250	0.000	0.64/0.36	0.0109(7)
Ge2	16i	0.183(2)	x	x	1	0.0076(2)
Ge3/Sn3	24k	0.314(5)	0.119(9)	0.000	0.983/0.017	0.0088(2)

atom	U_{11}	U_{22}	U_{33}	U_{23}	U_{13}	U_{12}
Ba1	0.0089(3)	U_{11}	U_{11}	0.000	0.000	0.000
Ba2	0.0228(5)	0.0412(4)	U_{22}	0.000	0.000	0.000
Cu1/Ge1	0.0092(7)	0.0143(9)	0.0092(7)	0.000	0.000	0.000
Ge2	0.0076(2)	U_{11}	U_{11}	-0.0010	U_{23}	U_{23}
Ge3/Sn3	0.0086(3)	0.0095(3)	0.0085(3)	0.000	0.000	0.0012(2)

Table 5.3: Fractional atomic coordinates, site occupancies, and isotropic (U_{eq}) and anisotropic (U_{ij}) atomic displacement parameters at RT for BAgG, obtained from single crystal x-ray diffraction analyses (With residuals: R = 0.023 for all data and wR_2 = 0.051 and a lattice parameter: a = 10.8905(3).)

atom	site	x	y	z	occupancy	U_{eq}
Ba1	2a	0.000	0.000	0.000	1	0.0062(6)
Ba2	6d	0.250	0.500	0.000	1	0.0400(7)
Ag1/Ge1	6c	0.500	0.250	0.000	0.83/0.17	0.0100(7)
Ge2	16i	0.183(2)	x	x	1	0.0063(5)
Ge3/Sn3	24k	0.307(2)	0.116(7)	0.000	0.959/0.041	0.0092(5)

atom	U_{11}	U_{22}	U_{33}	U_{23}	U_{13}	U_{12}
Ba1	0.0062(6)	U_{11}	U_{11}	0.000	0.000	0.000
Ba2	0.0316(1)	0.0443(9)	U_{22}	0.000	0.000	0.000
Ag1/Ge1	0.0074(8)	0.0150(1)	0.0074(8)	0.000	0.000	0.000
Ge2	0.0063(5)	U_{11}	U_{11}	-0.0012	U_{23}	U_{23}
Ge3/Sn3	0.0086(7)	0.0090(7)	0.0101(7)	0.000	0.000	0.0011(4)

TABLE 5.4: Fractional atomic coordinates, site occupancies, and isotropic (U_{eq}) and anisotropic (U_{ij}) atomic displacement parameters at RT for BAuG, obtained from single crystal x-ray diffraction analyses (With residuals: $R = 0.022$ for all data and $wR_2 = 0.046$ and a lattice parameter: $a = 10.8462(3)$.)

atom	site	x	y	z	occupancy	U_{eq}
Ba1	2a	0.000	0.000	0.000	1	0.0044(3)
Ba2	6d	0.250	0.500	0.000	1	0.0348(4)
Au1/Ge1	6c	0.500	0.250	0.000	0.875/0.125	0.0083(2)
Ge2	16i	0.183(3)	x	x	1	0.0040(3)
Ge3/Sn3	24k	0.308(8)	0.118(2)	0.000	0.959/0.041	0.0055(3)

atom	U_{11}	U_{22}	U_{33}	U_{23}	U_{13}	U_{12}
Ba1	0.0044(3)	U_{11}	U_{11}	0.000	0.000	0.000
Ba2	0.0236(6)	0.0404(5)	U_{22}	0.000	0.000	0.000
Au1/Ge1	0.0049(3)	0.0151(4)	0.0049(3)	0.000	0.000	0.000
Ge2	0.0040(3)	U_{11}	U_{11}	-0.0011	U_{23}	U_{23}
Ge3/Sn3	0.0053(4)	0.0059(4)	0.0052(4)	0.000	0.000	0.0008(3)

the similar atomic form factors of Cu and Ge, which may give rise to big errors in the atomic occupancy analyses. It should be noted that the lattice parameters of BMG grown by Sn-flux are larger than the lattice parameters of BMG compounds grown by other methods [152, 156, 160], because in the former case big Sn atoms are included inside the crystal lattices.

5.3.2 Electrical Transport Properties

The electrical resistivities of BMG compounds are shown in Figure 5.4 (a) from 2 K to 350 K. BCG and BAgG show low resistivities as well as metallic conduction behaviors, while BAuG shows a relatively high resistivity and a semiconducting behavior. Hall resistivity measurements show that all the BMG compounds in the present study are n-type. Carrier concentrations, derived from Hall coefficients, are shown in Figure 5.4 (b) from 2 K to 300 K. The comparison of resistivity (ρ) as well as carrier concentration (n) among BMG compounds indicate that ρ is mainly controled by n, and the free electron model, where $\rho = \frac{m^*}{ne^2\tau}$, works well for these compounds. Here m^* is the effective mass and τ is the relaxation time of conduction electrons.

According to Figure 5.4 (a) and (b), electron mobilities ($\mu = 1/ne\rho = \frac{e\tau}{m^8}$) are derived as shown in Figure 5.4 (c) and (d). BCG shows the highest electron mobility, while the values of BAgG and BAuG are smaller; the differences may partially come from τ and partially come from m^* as one shall see it later on (table 5.6). The temperature dependent mobilities indicate that the conduction electrons are mainly scattered by phonons in the case of BCG and BAgG, while in BAuG, ionized impurity scattering seems to be more important especially at low temperatures. It should be noted that the electron mobility of BCG here (18.5 cm^2/Vs at 300 K) is much higher than the values reported previously for the poly-crystals of BCG (less than 10 cm^2/Vs at 300 K) [111], and the electron mobility of BAuG is consistent with a previous report on BAuG single crystal grown by the Bridgman method [152].

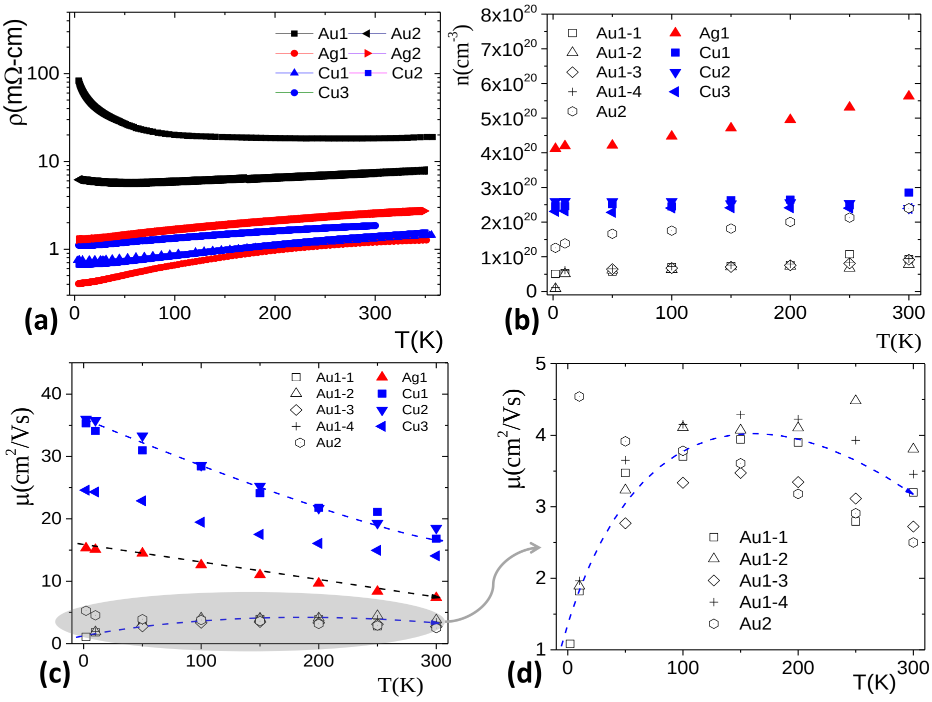

FIGURE 5.4: Electrical transport properties of BMG single crystals grown by Sn-flux. (a) Electrical resistivity. (b) Carrier concentration. (c) Electrical mobility. (d) Electrical mobility of BAuG. The Cu, Ag and Au, written on the figures, stand for BCG, BAgG and BAuG respectively (it should be applied for the subsequent figures as well). The dashed curves serve as guides for the eyes.

5.3.3 Heat Capacity

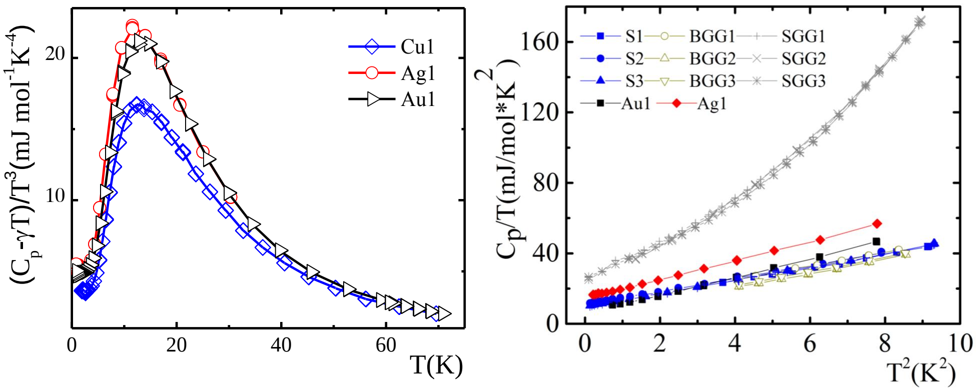

FIGURE 5.5: Heat capacity data of BMG single crystals. Left: $(C_p - \gamma T)/T^3$ vs. T plot, where γT is the temperature linear dependent heat capacity contributed from conduction carriers or tunneling states. Right: C_p/T vs. T^2 plot below 3 K. For comparison, the data of BGG and SGG are also included [75, 76].

The heat capacity data of BMG compounds are shown in Figure 5.5. The rattling phonon modes are detected by the boson peaks in the $(C_p - \gamma T)/T^3$ vs. T plot as shown in the figure. By applying a combined Einstein and Debye model as we did in chapter 3, the heat capacity data can be well fitted. The fitting parameters are shown in Table 5.5. θ_{E1} describes the guest vibration modes parallel to the six member ring inside tetrakaidecahedral cages (Refer to fig. 1.7) and θ_{E2}

describes the perpendicular vibration modes. The guest atoms inside dodecahedral cages are treated as Debye oscillators in the fitting. One shall refer to chapter 3 for more details of the analytical method. The fitting based on a harmonic model indicates that the BMG compounds do not show large anharmonicity of the rattling motions, and this is consistent with the X-ray single crystal diffraction measurement results that guest atoms are on-centered (See tables 5.2 to 5.4). The harmonic situation can also be revealed by the heat capacity data below 3 K as shown on the right side of fig. 5.5. Unlike SGG, which shows strong phonon anharmonicity (due to tunneling states: refer to chapter 4 for details), BMG compounds are similar to BGG and show a harmonic-like behavior.

Table 5.5: Debye (θ_D) and Einstein (θ_E) temperatures for fitting the heat capacity data of BMG compounds.

Sample	θ_{E1}	θ_D	θ_{E2}
BAuG	56	250	81
BAgG	54	248	90
BCG	58	284	95

Temperature linear dependent heat capacities (γT) are observed in fig. 5.5 (Right side), as indicated by the non-zero intercepts. At this temperature range, C_p can be simply expressed as: $C_p = \gamma T + DT^3$, where DT^3 is the heat capacity described by the Debye T^3 law. Linear fittings were made on the data of BMG compounds and the fitting parameters γ and D are listed in Table 5.6. The values of γ_{free-e}, calculated by using free electron model: $\gamma_{free-e} = k_B^2 m_e (3\pi^2 n)^{1/3}/(3\hbar^2)$, are also listed in the table for comparison. Here k_B is the Boltzmann constant, $\hbar$ is the reduced Planck constant, m_e is the free electron mass, and n is the carrier concentration. Effective mass (m^*) is obtained by using γ/γ_{free-e} and the values are listed in table 5.6 as well. As mentioned earlier, effective mass influences electron mobility, here we show that there is indeed a good correspondence between the m^* listed in table 5.6 and the μ shown in fig. 5.4 (c). The effective mass enhancement in BMG compounds may result from e-ph interactions.

Table 5.6: The parameters of the linear fitting on the C_p/T vs. T^2 data of BMG compounds. Some other calculated parameters are also included as described in the main text. The units of γ and D are mJ mol^{-1}K^{-2} and mJ mol^{-1}K^{-4}, respectively.

Sample	γ	γ_{free-e}	m^*	D	θ_D (K)	v_{ph} (m/s)
BAuG1	5.07	2.47	2.05	–	–	–
BAuG2	5.50	2.70	2.04	5.20	258.1	2624.3
BAuG3	8.78	–	–	6.64	237.9	2416.7
BAgG1	14.74	9.17	1.61	5.30	256.5	2613.9
BCG1	10.14	7.74	1.31	3.63	291.0	2934.3
BCG2	11.27	7.90	1.43	3.60	291.8	2942.4
BCG3	9.81	7.29	1.24	3.71	288.9	2913.1

5.3.4 Thermoelectric Properties

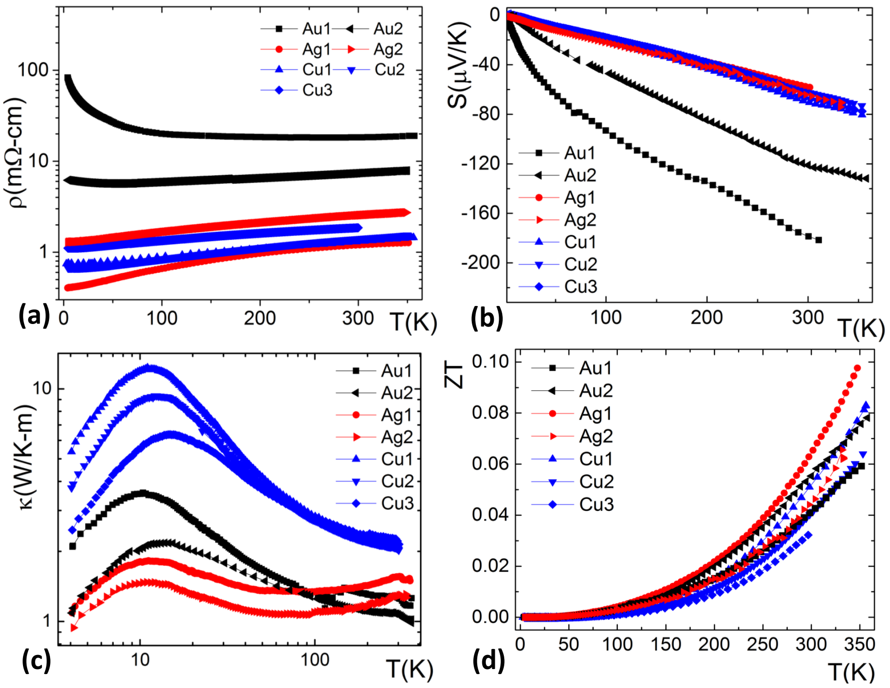

FIGURE 5.6: Thermoelectric properties of BMG single crystals from 2 K to 350 K. (a) Electrical resistivity. (b) Seebeck coefficient. (c) Thermal conductivity. d The figure of merit, ZT.

The thermoelectric properties of BMG compounds from 2 K to 350 K are shown in Figure 5.6. Seebeck coefficient measurement results show that all BMG are n-type compounds, it is consistent with the Hall resistivity measurement result. Similar to electrical resistivity, Seebeck coefficient is also controlled by carrier concentration. According to eq. (1.16), Seebeck coefficient depends on m^* as well. All BMG compounds show low thermal conductivities (κ's) as a consequence of the rattling phonon modes. The κ's of BAgG and BAuG are even lower than that of BCG. Radiation losses are observed at higher temperatures and the different heights of low temperature peaks within a same species of compounds may be caused by the thermal contact resistance of the two-probe measurements or come from the influence of grain size or a secondary phase as pointed out by Aydemir *et al.* [101]. It should be noted that thermal contact resistance does not influence the measurement results much at high temperatures as shown in Figure 5.6 (c). It should also be noted that, even under two-probe measurement, the low temperature peaks in κ are higher than the data reported elsewhere [107]. This indirectly points out that our single crystals are of high quality. The ZT values are shown in Figure 5.6 (d) and they should be around 1.5 times higher at 350 K if the radiation losses were corrected.

The thermal conductivity is composed of electron contributions (κ_e) and phonon contributions (κ_L). κ_e can be derived by the Wiedemann-Franz Law, $\kappa_e = LT\sigma$ as described in chapter 1. κ_L and κ_e of BMG compounds are shown in Figure 5.7 (a) and (b), respectively. It is clear that the heat conduction is dominant by phonons in BMG clathrates. In order to know more about the phonon transport information, we expand κ_L according to a simple model: $\kappa_L = \frac{1}{3}Cl_{ph}v$, where C is the heat capacity, l_{ph} is the phonon mean free path, and v is the sound speed. Since C and κ_L have been experimentally obtained and v can be estimated by, $v = (\frac{V}{6\pi^2 N})^{1/3}\frac{k_B}{\hbar}\theta_D$

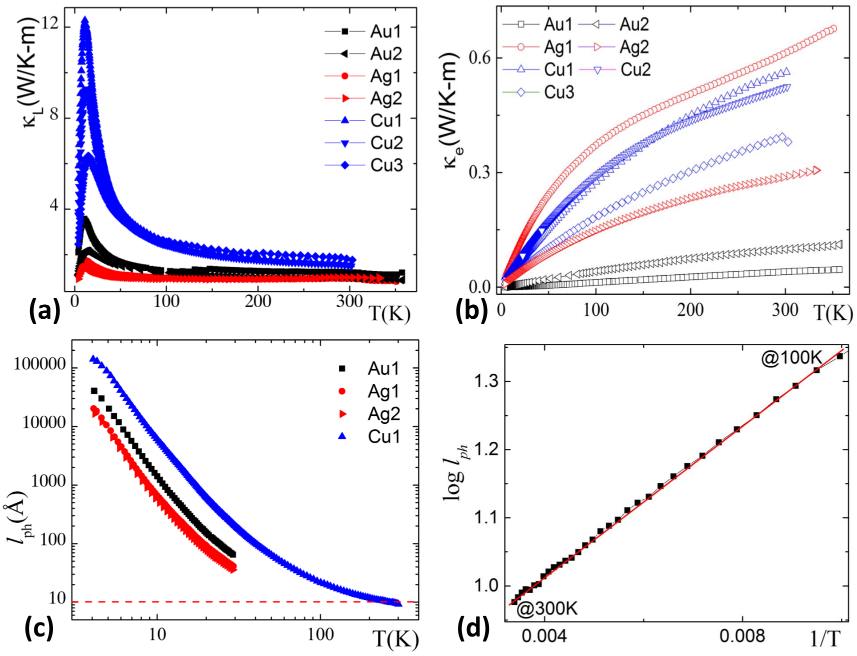

Figure 5.7: Thermal conductivity and phonon mean free path (l_{ph}) of BMG single crystals. (a) Lattice thermal conductivity (κ_L). (b) Thermal conductivity contributed from conduction electrons (κ_e). (c) Phonon mean free path. The dashed line shows the lattice constant of a BCG compound. d The phonon mean free path of a BCG compound, plotted as logl_{ph} vs. $1/T$. The red line is a guide for the eyes.

(the values are shown in table 5.6), the phonon mean free path can be derived. Here V is volume and N is the number of Debye oscillators in the given volume. It should be noted that the θ_D in Table 5.6, obtained below 3 K, is consistent with the θ_D in Table 5.5, obtained at higher temperatures and we applied the former values for estimation. l_{ph} is shown in Figure 5.7 (c) as a function of temperature. BAgG and BAuG have shorter l_{ph} than BCG does, and it may result from the lattice disorder created by mass and atomic radii fluctuations of the cage atoms. As shown in Figure 5.7 (d) logl_{ph} is linearly related to $1/T$ from 100 K to 300 K, which indicates that the Umklapp process of phonon-phonon scattering dominant the phonon transport at high temperatures.

The relationships between thermoelectric parameters and the corresponding electron densities as well as electron mobilities for BMG compounds are shown in Figure 5.8. In Figure 5.8 (a), electron mobility is plotted as a relationship with carrier concentration. The single crystals of BCG in the present work show very high mobilities, comparing with the data of BGG and BCG-poly-crystals [111]. BAgG and BAuG show lower mobilities due to their large effective mass of conduction electrons. In Figure 5.8 (b), Seebeck coefficient is plotted as a function of carrier concentration. S decreases as n increases, which is consistent with eq. (1.16). BAgG and BAuG show slightly higher Seebeck coefficients due to their large m^*'s. Thermoelectric power factor, which is expressed as $PF = S^2\sigma = \pi^{4/3}k_B^4T^2m^{*2}\mu/e\hbar^4 3^{4/3}n^{1/3}$ in the framework of an effective mass approximation, is shown in Figure 5.8 (c) and (d) as a relationship with n and μ, respectively. The data shown in the figures give us the following important conclusions. (1) In BMG-clathrate system, large m^* is favored for having better thermoelectric performance, regardless of the consequent low μ. This situation is exemplified by BAgG and BAuG compounds. (2) In clathrate system, increasing μ via improving crystal quality is favored for having high

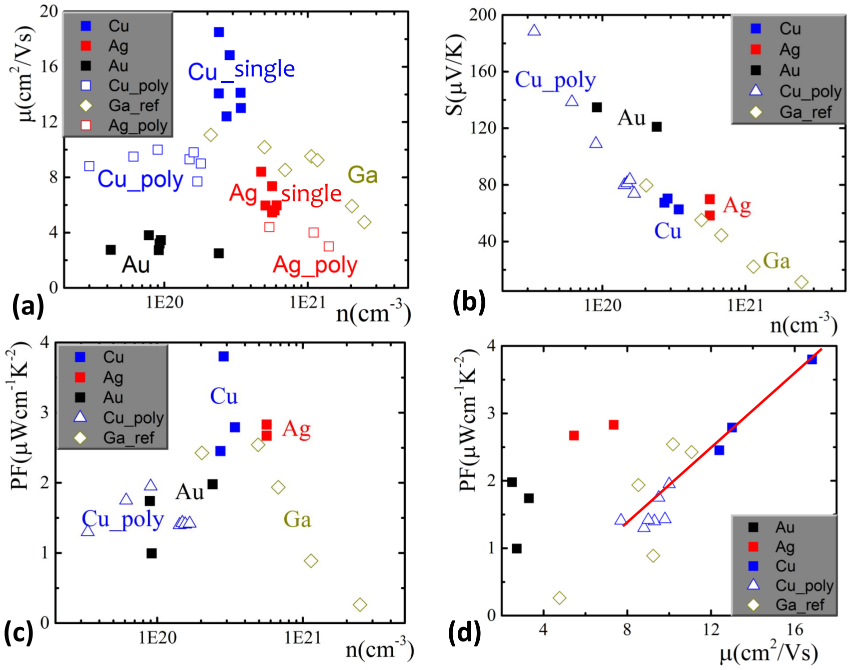

Figure 5.8: (a) The relationship between μ and n. (b) The relationship between § and n. (c) The relationship between power factor (PF) and n. (d) The relationship between PF and μ. The red line is a guide for the eyes. The data of BGG, BAgG-poly-crystals and BCG-poly-crystals are taken from Refs. [111, 156].

thermoelectric performance. This situation can be shown by the red line in Figure 5.8 (d) for the BCG and BGG, which have similar carrier concentrations. In practice, it is difficult to control effective mass within one compound, the first conclusion should be applied only for searching new materials with large m^* for thermoelectric applications in clathrate-system. While the second conclusion can be actually applied, and we suggest that high quality single crystals are very important for achieving high ZT values in clathrate-system.

5.4 Summary

Single crystals of noble metal clathrates, BMG (M = Cu, Ag, Au), were successfully synthesized by using a Sn-flux method. We showed that the crystals are of high quality by using single crystal X-ray diffraction measurements, SEM-EDS measurements, and physical properties measurements. A small amount of Sn was revealed as a component of the grown crystals mainly in 24k sites. Effective mass was derived from heat capacity data below 3 K. Hall resistivity and Seebeck coefficient measurements showed that the single crystals are all n-type compounds. BCG showed a high mobility of 18.5 cm^2/Vs and a high power factor of 3.8 μWcm^{-1}K^{-2} at 300 K. By comparing with previously reported data, we concluded that high mobility and large effective mass are favored for achieving high thermoelectric performance in clatharte-system, and high quality single crystals are very important.

Chapter 6

Anomalous Diamagnetism in Type-I Clathrates

This is the last topic of the present thesis, and we are going to describe an interesting but non-thermoelectricity related issue in this chapter. We hope that the present chapter could contribute to a better understanding on thermoelectric clathrates.

A Brief Abstract

Magnetic susceptibility and Hall coefficient are measured for a serials of clathrate compounds: $Ba_8Ga_{16}Ge_{30}$, $Sr_8Ga_{16}Ge_{30}$, $Ba_8Ga_{16}Sn_{30}$ (both type I and type VIII), $Ba_8Ga_{16}Si_{30}$ and Ba_8Ge_{43} from 2 K to 300 K. An extra diamagnetic susceptibility of around -7.5×10^{-4} cm^3/mol is obtained for these compounds (except for Ba_8Ge_{43}) at 300 K, in addition to the contributions from atomic cores and conduction electrons. The additional diamagnetism, which is larger than the core diamagnetism, was previously suggested to be contributed from the conceptual ring current because of the structural similarities of clathrates and graphite. However, several evidences, including the cage size independent susceptibility and the abnormally large extra diamagnetic susceptibility of Ba_8Ge_{43}, reaching around -15×10^{-4} cm^3/mol at 300 K, indicate that the ring current concept is insufficient. Possible reasons are addressed, including the imbalance between the Langevin diamagnetism of valence electrons and the Van Vleck paramagnetism as well as the large electron orbits around the rattlers under large space. Theoretical calculation is expected to verify this viewpoint.

6.1 Introduction

As described in chapter 1, type-I clathrates are featured by cage structures with guest atoms accommodated inside the cages. The unique structure grants the material a variety of excellent properties, which have been described in chapter 1 and discussed in details from chapter 3 to chapter 5. One of the curious issues in this series of compounds consisting of polyhedral units with their faces shared (fig. 6.1) is whether the diamagnetism associated with ring current generally known for aromatic molecules exist also in clathrate compounds [63, 81, 159].

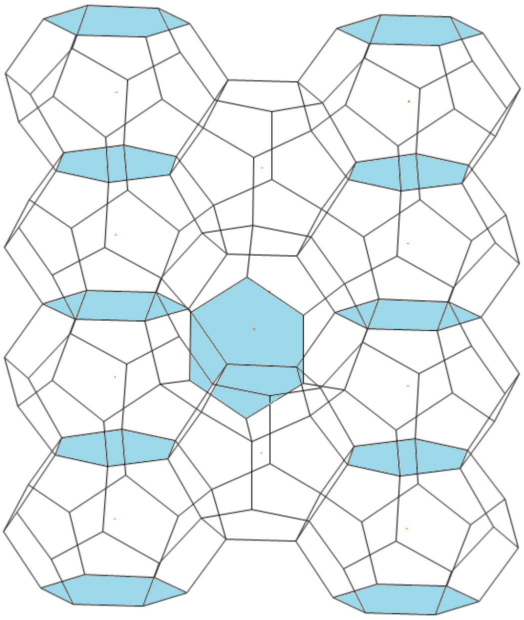

Figure 6.1: Cage frameworks of type-I clathrate. It is basically the same as fig. 1.7, but only frameworks are shown here. The six-member rings on polyhedra are painted with a blue color.

In principle, the diamagnetism of a semiconductor like clathrate is only a common physical phenomenon, and it attracts few interests in the physical society. However in clathrate-system, it has been reported that there was an anomaly in diamagnetism, which could not be interpreted by the atomic addition rule [162–164]. The first report regarding the extra diamagnetism in clathrates was made by Christian Cros *et al.* [164], and the conceptual "ring current" (RC) was suggested to play a similar role in clathrates as in C_{60}, graphite and benzene, etc. Later on, S. Paschen *et al.* also applied the RC concept to interpret their experiment data [44], and T. Rachi *et al.* tried to evaluate the RC diamagnetism of clathrates by using the modified Pauling's formula [162]. Nevertheless, no one could provide a clear interpretation of RC or an evidence that RC indeed exists in clathrates so far. There are two main difficulties: (1) RC in aromatic molecules or carbon networks are created by those unpaired delocalized π-electrons in planar structures; however such π-electrons and planar structures can not be found in clathrates. Only six-member rings, indicated by the blue color in Figure 6.1 can be observed in clathrates. (2) No appropriate theoretical model can be applied for RC in clathrate system. Therefore the research regarding RC in clathrate-system becomes a challenge and quite interesting

The diamagnetism due to RC should be considered as a special case, in addition to that, there are generally two ways to consider the diamagnetism of a semiconductor: electron band approach and chemical bond approach. Although the empirical chemical bond description over simplifies the electronic structure of a solid, it avoids the computational difficulties of band theory and provides a practical method for magnetic susceptibility data analyses [165, 166]. S. Hudgens *et al.* have successfully applied this method to interpret the diamagnetic susceptibility (χ) of tetrahedral semiconductors (C, Si, Ge etc.) [166]. They expressed the χ as:

$$\chi_{total} = \chi_{core} + \chi_{valence} + \chi_{van-vleck} \tag{6.1}$$

where χ_{core} is the contribution from atomic cores, $\chi_{valence}$ is the Langevin-like valence electron contributions, and $\chi_{van-vleck}$ is the Van Vleck paramagnetic contributions. By applying this formula, it is easy to understand why $\chi_C = -6.0\times10^{-6}\text{cm}^3\text{mol}^{-1} < \chi_{Si} = -3.12\times10^{-6}\text{cm}^3\text{mol}^{-1}$, even though silicon has both larger χ_{core} and $\chi_{valence}$ [166]. The chemical bond approach may be similarly applied in the clathrate-system as well, however no such a study has been made.

In this chapter, we investigate the magnetic properties of a serials of clathrate compounds: $Ba_8Ga_{16}Ge_{30}$ (BGG), $Sr_8Ga_{16}Ge_{30}$ (SGG), $Ba_8Ga_{16}Sn_{30}$ (BGSn: both type I and type VIII), $Ba_8Ga_{16}Si_{30}$ (BGSi) and Ba_8Ge_{43} (BG) from 2 K to 300 K. Our results show that ring current might not be responsible for the "large" diamagnetism of clathrates for the first time, and we suggest that the chemical bond approach may be a good candidate to understand the experiment data. We expect a theoretical calculation to confirm this conclusion.

6.2 Experiment method

Single crystals of BGG, SGG and BGSn samples were synthesized by using the self-flux method as described in previous chapters and reported literatures [41, 83, 142]. BGSi single crystals were obtained from our collaborators, and BG-poly-crystals were prepared by using the RF induction furnace as described in chapter 2. The quality of single crystals were checked by single crystal X-ray diffraction measurements at BL02B2 beam port in the high-energy factory of Spring 8, and the diffraction data were refined by using WinGX [89]. Poly-crystals were checked by X-ray powder diffraction measurements using Rinaku RINT2500/PC system, with the graphite monochromatized Cu $K\alpha$ radiation. A small amount of Ge impurity was observed in BG compounds. Magnetic susceptibility was measured by using the magnetic properties measurement system (MPMS SQUID: Quantum Design) from 2 K to 300 K under a magnetic field of 2 T and 5 T, respectively for each sample. Magnetic field dependent magnetization was also measured from -5 T to 5 T at 300 K. Hall coefficient measurement was performed by using the resistivity option of PPMS (Quantum Design) at 2 K, 10 K, 50 K, 100 K, 150 K, 200 K, 250 K and 300 K. The compounds in the present study are all n-type. Refer to chapter 2 for more details of the experiment process.

6.3 Results and discussions

Carrier concentration (n) were obtained from Hall resistivity measurement, and the carrier concentrations in the present study are almost temperature independent. The values of n at 300 K for different clathrate compounds are shown in Table 6.1 for evaluating the magnetic susceptibility contributed from conduction carriers ($\chi_{carrier}$).

Figure 6.2 shows the experiment data of temperature dependent magnetic susceptibilities for selected samples. The influence of possible ferromagnetic impurities was removed via: $\frac{M(5T)-M(2T)}{5T-2T}\frac{A}{m}$, where M is the intensity of magnetization, A is the molar mass of a clathrate compound, and m is the mass of a measurement sample. It is shown that different samples of the same species have almost same magnetic susceptibilities, revealing that the diamagnetism is an intrinsic property of clathrates. The susceptibility shown in the figure is almost temperature

Table 6.1: Magnetic susceptibilities of type-I clathrate compounds at 300 K. The unit of n is cm^{-3}, the unit of m^* is m_0, the unit of lattice constant a is nm and the unit of susceptibility is 10^{-4} cm^3/mol.

Sample	n	m^*	a	$\chi_{carrier}$	χ_{total}	χ_{core}	χ_{extra}
BGSi	4.03×10^{21}	1	1.055	1.65	-9.82	-3.65	-7.82
BGG-1	4.31×10^{19}	1.01	1.080	0.392	-12.3	-5.30	-7.35
BGG-2	1.81×10^{20}	1.01	1.078	0.632	-12.0	-5.30	-7.35
BGG-3	1.20×10^{20}	1.01	1.079	0.551	-12.1	-5.30	-7.30
BGG-4	3.20×10^{20}	1.01	1.078	0.765	-11.9	-5.30	-7.38
BGG-5	2.99×10^{20}	1.01	1.078	0.748	-12.3	-5.30	-7.75
BGG-6	6.41×10^{20}	1.01	1.078	0.964	-12.1	-5.30	-7.76
BGSn(I)-1	1.60×10^{18}	2.05	1.170	0.470	-15.2	-8.00	-7.67
BGSn(I)-2	3.60×10^{18}	2.05	1.171	0.616	-15.3	-8.00	-7.90
BGSn(VIII)-1	3.36×10^{19}	1	1.159	0.447	-13.9	-8.00	-6.32
BGSn(VIII)-2	3.31×10^{19}	1	1.160	0.444	-13.9	-8.00	-6.35
SGG-1	2.95×10^{20}	1.68	1.074	1.62	-10.3	-4.58	-7.32
SGG-2	5.34×10^{20}	1.68	1.074	1.97	-10.1	-4.58	-7.51
SGG-3	8.17×10^{20}	1.68	1.074	2.28	-10.2	-4.58	-7.87

independent, except for the data of type-VIII BGSn and SGG. In the case of type-VIII BGSn, a small Curie-like temperature dependent susceptibility is observed due to localized spins, similar to the situation of p-type BGG shown in fig. 4.8. For SGG, the magnetic susceptibility is almost linearly dependent on temperature. This situation has been observed in NMR measurement [51], and it was ascribed to the temperature dependent chemical shift. The small variation of the data for different sample of the same species is possibly caused by different carrier concentrations or experimental errors.

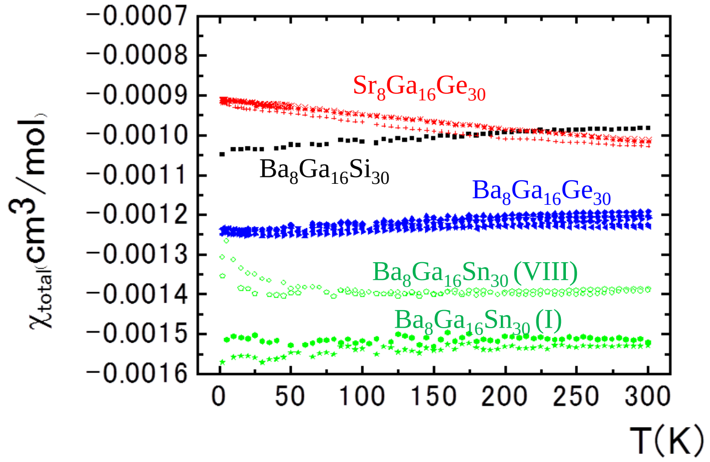

Figure 6.2: Temperature dependent magnetic susceptibilities of type-I clathrates: BGG, SGG, BGSi, and BGSn.

In order to interpret the data shown in fig. 6.2, for the first step, we follow the analytical method reported elsewhere [162, 163] and expand the susceptibility as:

$$\chi_{total} = \chi_{core} + \chi_{carrier} + \chi_{extra} \tag{6.2}$$

where χ_{total} is the experiment data, $\chi_{carrier}$ is the the contribution from conduction carriers and χ_{extra} is the additional contributions, which may come from structure factors or other factors like RC. The susceptibility of conduction electrons can be derived by the following formula [167]:

$$\chi_{carrier} = \chi_{pauli}(1 - \frac{1}{3}(\frac{m_0}{m^*})^2) \tag{6.3}$$

where m_0 is the free electron mass, m^* is the effective mass of conduction electrons and χ_{pauli} is Pauli paramagnetic susceptibility and can be analytically expressed as:

$$\chi_{pauli} = \frac{2m^*\mu_B^2}{\pi\hbar^2}(\frac{3}{8\pi}n)^{1/3} = \frac{m^*}{m_0} \times 2.21 \times 10^{-14} n^{1/3} \times (N_A \cdot a^3) \tag{6.4}$$

Here μ_B is the Bohr magneton, $\hbar$ is the reduced Planck constant, N_A is the Avogadro constant and a is the lattice constant. $\chi_{carrier}$ and the associated parameters at 300 K are summarized in Table 6.1 for the clathrate compounds in the present study. It should be noted that the lattice constants shown in the table are obtained from X-ray powder diffraction measurements at room temperatures and the effective mass are taken from chapter 4. For type-VIII BGSn and BGSi, free electron mass is assumed. Core diamagnetic contributions χ_{core} are estimated by using the values of closed-shell cations in the literature (unit: 10^{-6} cm^3/mol), -24 for Ba^{2+}, -15 for Sr^{2+}, -8 for Ga^{3+}, -1.5 for Si^{4+}, -7 for Ge^{4+}, and -16 for Sn^{4+} [168]. χ_{core} of the selected samples are shown in Table 6.1.

By subtracting χ_{core} and $\chi_{carrier}$ from χ_{total}, we obtained the additional diamagnetic contributions, χ_{extra}, as shown in table 6.1 at 300 K and fig. 6.3 from 2 K to 300 K. According to table 6.1 the additional magnetic susceptibility is 1-2 times the value of χ_{core} and much larger (absolute values) than the contributions from conduction electrons. The unexpected large values of χ_{extra} were ascribed to the conceptual RC by many researchers previously [162, 163, 169]; however our experiment data show some discrepancies here.

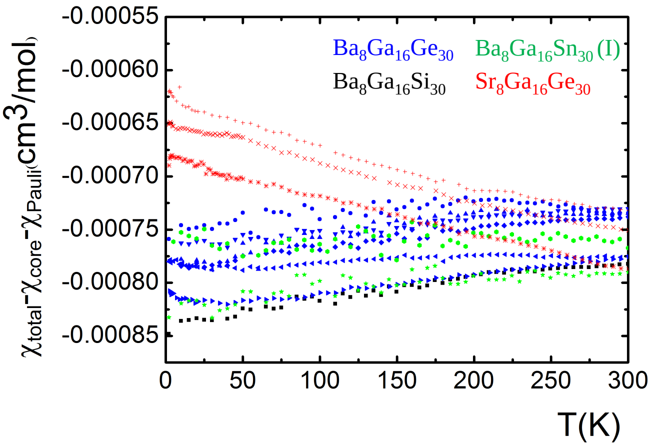

FIGURE 6.3: The additional diamagnetic susceptibility χ_{extra} for BGG, SGG, BGSi, and BGSn.

The lattice constants shown in table 6.1 give the relationship: a(BGSn(I))> a(BGG)> a(SGG)> a(BGSi). In principle, RC concept should give a consistent result, χ(BGSn(I))> χ(BGG)> χ(SGG)> χ(BGSi) for their absolute values. Nevertheless, the values in table 6.1 conflict this assumption: BGSi with the smallest size even shows the largest χ_{extra} within the experiment error. The cage size independent χ_{extra} suggests that RC might not be the reason of the large diamagnetism of clathrates, at least not the only factor.

The temperature dependent susceptibility, especially for SGG, also conflicts the RC concept, because the susceptibility due to RC should be temperature independent as pointed out previously [63, 149]. It should be noted that the contribution from conduction carriers can not be account for the temperature dependent susceptibility. In addition, the magnetic susceptibilities of type-I and type-VIII BGSn compounds only show small differences, but we do not expect that RC sustains while the crystal structure is tranformed from type-I to type-VIII. Our measurement on BG, which contains three vacancies on 6c sites, shows a χ_{extra} value of -15×10^{-4} cm^3/mol, which is much larger than the values shown in table 6.1 for other clathrates. It is quite hard to understand that the vacancies could enhance RC. In summary, RC concept fails to be applied in clathrate-system.

Possibly, we can consider the magnetic susceptibility of clathrates in a similar way as researchers did for tetrahedral semiconductors by using a chemical bond approach [166]. According to this method, susceptibility of clathrate should be expanded as: $\chi_{total} = \chi_{core} + \chi_{carrier} + \chi_{valence} + \chi_{van-vleck}$, where $\chi_{extra} = \chi_{valence} + \chi_{van-vleck}$. It means that the imbalance between $\chi_{valence}$ and $\chi_{van-vleck}$ may create large χ_{extra} values. It has been reported that there is a diamagnetic susceptibility enhancement in amorphous materials comparing with their crystalline state [170, 171]. For example, amorphous Ge is about 2.7 times more diamagnetic than crystalline Ge. Therefore we come to the conclusion that χ_{extra} is very sensitive to crystal structures, and it might be intrinsically large under the structure of clathrates.

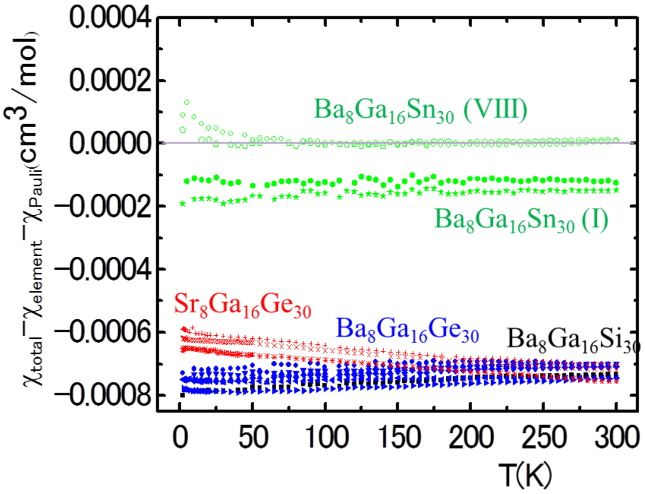

Figure 6.4: The additional diamagnetic susceptibility χ_{extra} for type-I clathrate compounds by applying $\chi_{element}$ instead of χ_{core}.

In order to test our idea, we modified eq. (6.2) as:

$$\chi_{total} = \chi_{element} + \chi_{carrier} + \chi_{extra} \tag{6.5}$$

In the above expression, valence electrons are considered. For example in the case of BGSn, we applied χ_{Sn} instead of $\chi_{Sn^{4+}}$. It is noted that $\chi_{element}$ strongly depends on the crystal form of the element. In our test, we applied the values of tetrahedral semiconductors for Si, Ge and Sn, and used χ_{Ge} for χ_{Ga}. The new χ_{extra} is shown in Figure 6.4, and surprisingly, BGSn shows almost zero χ_{extra}. In order to solve the problem completely, theoretical calculations are required. There are also other possibilities for interpreting the large χ_{extra} in clathrates. For instance, the large free space around rattlers may enable electrons to move along large orbits and lead to large diamagnetic susceptibility.

6.4 Summary

Magnetic susceptibility of type-I clathrates: BGSi, BGG, SGG, BGSn, BG and type VIII clathrate BGSn were studied from 2 K to 300 K. In addition to the core diamagnetic susceptibility and the susceptibility due to conduction electrons, an additional contribution around -7.5×10^{-4} cm^3/mol at 300 K was observed. We showed that ring current could not explain the additional diamagnetic susceptibility. Possible reasons were suggested, including the imbalance between the Langevin diamagnetism of valence electrons and the Van Vleck paramagnetism as well as the large electron orbits around the rattlers under large free space. We hope that theoretical calculations can be made to test our idea.

Chapter 7

Conclusion

7.1 Summary

As described in chapter 1, thermoelectric researches are of great importance as they contribute to energy saving, transferring waste heat into applicable electrical energy. Intermetallic clathrates are classified as the conceptual "phonon-glass electron-crystal" compounds and have been widely studied for thermoelectric application. The most valuable point in clathrates for thermoelectric study is the low-energy-lying guest phonon modes, which on one hand suppress heat conduction efficiently, while on the other hand exert little influence on electrical conduction. Systematic studies regarding guest vibrations were made in chapter 3 and 4.

First, we considered the guest atom vibrations at intermediate temperatures (from 2 K to 70 K), where "boson peaks" were observed for the low-energy phonon modes. We showed that the excitation energies of all boson peaks could surprisingly be unified as one single exponential line using a new space parameter (R_{free}) associated with the freedom of motion of guest atoms. By combining experiment data, first principle calculations and a theoretical model based on van der Waals interactions, we pointed out that the guest-framework interactions are basically van der Waals type interactions, and Coulombic ionic and/or covalent interactions are not significantly important on the energy scale of the boson peaks. We also pointed out the importance of symmetry-broken for having off-centered guest vibrations. The study on boson peaks in type-I clathrates is helpful for understanding the origin of boson peaks in glass system and contributes to thermoelectric materials design from the viewpoint of rattling phonons.

Then, we considered the guest atom vibrations at extremely low temperatures (below 1 K), where tunneling states were observed for off-centered guest atoms as indicated by a temperature linear as well as time dependent heat capacity. We successfully separated the total linear-T dependent C_{p} into two parts: the anharmonic phonon $\alpha\,\mathrm{T}$ and the electronic $\gamma_e\mathrm{T}$ terms, and m^*'s were evaluated from the γ_e values. Based on these parameters for a series of clathrate compounds, we concluded that the arrangement of framework atoms are very important for having off-centered guest vibrations. We also came to the conclusion that phonon anharmonicity, indicated by tunneling states, is quite useful for improving thermoelectric performance.

In addition to the guest atom phonon modes, we also studied the electrical and thermal properties of the rattling-system by focusing on the noble metal (mainly Cu, Ag and Au) containing clathrates grown by Sn-flux. We showed that our single crystals are of high quality as indicated by X-ray single crystal diffraction measurements as well as high electron mobilities. By comparing with previously reported data, we concluded that high mobility and large effective mass are favored for achieving high thermoelectric performance in clatharte-system, and high quality single crystals are very important. At the end of this dissertation, we mentioned an interesting but non-thermoelectricity related issue: the anomaly of diamagnetic susceptibility in type-I clathrates. In addition to the core diamagnetic susceptibility and the susceptibility due to conduction electrons, an extra contribution, around -7.5×10^{-4} cm^3/mol at 300 K, was observed. Although the extra contributions were once ascribed to the conceptual ring current (RC), we showed that RC was not the main factor. Possible suggestions, including the imbalance between the Langevin diamagnetism of valence electrons and the Van Vleck paramagnetism, were proposed.

In summary, our studies in this dissertation mainly considered the rattling phonons and the associated thermal and electrical properties in type-I clathrates for the purpose of an elementary study on how to improve the thermoelectric performance by including rattling phonons.

7.2 Contributions

This dissertation contributes to the research society of clathrates for the following several aspects:

(1) We summarized several parameters for describing the anharmonicity of guest vibrations: they are $\mathrm{N}^{'}$, the number of vibration modes as described in chapter 3, α, the parameter of the T-linear dependent heat capacity of tunneling states as described in chapter 4, and the rattling factor f_R as introduced by our collaborators [132]. These parameters should be applied to other rattling-systems as well.

(2) For the first time we unified the boson-peak energies as a relationship with the space factor R_{free} by a universal exponential line in clathrates. The unification picture is helpful for understanding the origin of boson peaks in clathrates as well as in amorphous materials.

(3) We introduced van der Waals interaction to describe the guest-host interaction in intermetallic clathrates for the first time. This weak type interaction makes the vibrations of a guest atom liquid-like, and it is useful for thermoelectric materials design from the viewpoint of ”part-liquid and part-crystalline” concept [23, 77, 78].

(4) We observed a time dependent heat capacity due to tunneling states in a crystalline material for the first time.

(5) We synthesized high quality single crystals of noble metal containing clathrates by using a Sn-flux method for the first time.

7.3 Closing Remarks

Clathrates have already been well studied so far, as any possible formula has been tested and discussed. Therefore, it provides a possibility for making a systematic study for a series of clathrate compounds. In the present work, we presented a systematic study on the guest vibration modes as well as diamagnetism in type-I clathrates. We also provided a new approach for preparing single crystals of noble metal containing clathrates by using a Sn-flux method. In addition to the highlighted research achievements mentioned earlier, the present summary work shall serve as an overview in the field of intermetallic clathrates.

Appendix A

Kelvin relations derived from Onsager reciprocal relations

In the Section 1.2.1 of Chapter 1, we derived the Kelvin relations between thermoelectric coefficients by using the laws of thermodynamics. Here we show a strict way to derive Kelvin relations without assuming that the process is reversible by using Onsager reciprocal relations [167].

Base on the semiclassical theory of conduction in metals, one can derive the electrical and thermal conduction behavior from the nonequilibrium distribution function and construct the electrical current density $\mathbf{j}_e$ and thermal current density $\mathbf{j}_q$ by the Osager relations:

$$\begin{aligned} \mathbf{j}_e &= \mathbf{L}_{EE}\boldsymbol{\varepsilon} + \mathbf{L}_{ET}(-\nabla T) \\ \mathbf{j}_q &= \mathbf{L}_{TE}\boldsymbol{\varepsilon} + \mathbf{L}_{TT}(-\nabla T) \end{aligned} \tag{A.1}$$

where, $\boldsymbol{\varepsilon} = \mathbf{E} + \frac{\nabla\mu}{e}$, is the effective electric field composed of an electric field ($\mathbf{E}$) and a diffusion electric field ($\frac{\nabla\mu}{e}$) due to chemical potential gradient. T is temperature; $\mathbf{L}_{\alpha\beta}$ are matrices, which can be simplified under cubic symmetry.

Now we derive the Seebeck coefficient by using the Osager relations with the help of Figure A.1. According to the definition of seebeck coefficient(Equation (1.1)),

$$S\triangle T = \triangle V = -\int \boldsymbol{\varepsilon} d\mathbf{l} \tag{A.2}$$

This equation can be changed in another form,

$$S\nabla T = \boldsymbol{\varepsilon} \tag{A.3}$$

The best voltage-measurement condition shown in Figure A.1 is that the electric current is zero. Thus,

$$\mathbf{j}_e = \mathbf{L}_{EE}\boldsymbol{\varepsilon} + \mathbf{L}_{ET}(-\nabla T) \approx 0 \tag{A.4}$$

Combining Equations (A.3) and (A.4), we find,

$$S = \mathbf{L}_{ET}(\mathbf{L}_{EE})^{-1} \tag{A.5}$$

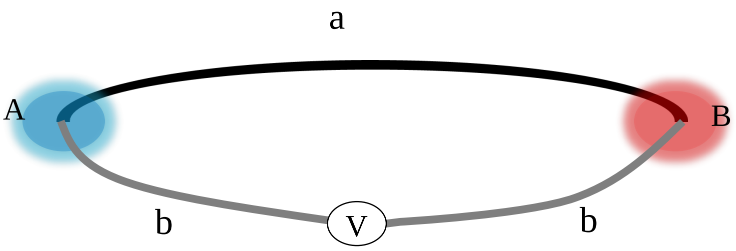

FIGURE A.1: A basic thermocouple, composed of metal a and b. The junction A is supposed to have a lower temperature T_{A} and the junction B is supposed to have a higher temperature T_{B}. V is a voltmeter.

For deriving the Peltier coefficient, we suggest the whole system is in a temperature T_0 as shown in Figure A.2. According to the Peltier effect, the flow of an electric current $\mathbf{j}_e$ will lead to heating at one junction and cooling at the other junction. (See chapter 1 for more details) In order to keep the system temperature T_0, there should be a thermal current flow as well as shown in Figure A.2. Following the definition of Peltier coefficient Π:

$$\Pi = \frac{q}{I} = \mathbf{j}_q(\mathbf{j}_e)^{-1} \tag{A.6}$$

As the temperature is homogenous, $\nabla T = 0$, the Osager relations can be simplified, and Π is found to be:

$$\Pi = \mathbf{L}_{TE}(\mathbf{L}_{EE})^{-1} \tag{A.7}$$

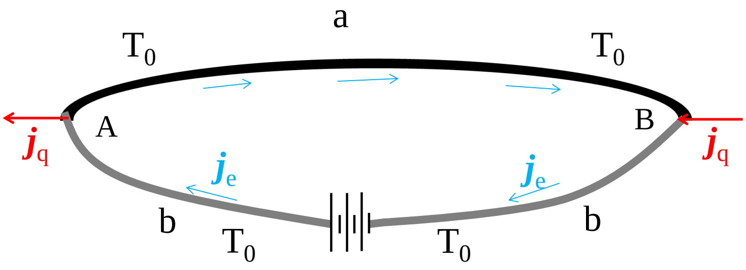

FIGURE A.2: A circuit composed of metal a and b for Peltier coefficient measurement.

The semiclassical theory of conduction in metals shows that $\mathbf{L}_{TE} = T\mathbf{L}_{ET}$ [167], thus the first Kelvin relation can be found: $\Pi = ST$ (same as eq. (1.4) in chapter 1).

In the case of Thomson effect, we need to consider a single homogenous metal in which thermal and electric currents flow simultaneously. The heat generation rate in unit volume can be written as (the first law of thermodynamics):

$$\frac{dq}{dt} = \frac{du}{dt} - \mu\frac{dn}{dt} \tag{A.8}$$

where u is the local internal energy, μ is the local chemical potential. There are normally three sources of the heat here: Joule heating, Thomson heating/cooling and heat conduction, which includes heat carried by electric current (Wiedemann-Franz law) and Peltier heat (heating or cooling). We will discuss about it later on.

In order to express Equation (A.8) more clearly, one has to use the continuity equations for carrier numbers and internal energy:

$$\begin{aligned} \frac{dn}{dt} + \nabla \mathbf{j}_n &= 0 \\ \frac{du}{dt} + \nabla \mathbf{j}_\epsilon &= \mathbf{E}\mathbf{j}_e \end{aligned} \tag{A.9}$$

where ϵ is the energy of a electron, the first equation indicates the conservation of the number of carriers and the second equation indicates the energy generation by Joule heating. Combining Equations (A.8) and (A.9),

$$\begin{aligned} \frac{dq}{dt} &= \frac{du}{dt} - \mu\frac{dn}{dt} \\ &= -\nabla \mathbf{j}_\epsilon + \mu\nabla\mathbf{j}_n + \mathbf{E}\mathbf{j}_e \\ &= -\nabla\mathbf{j}_q + \boldsymbol{\varepsilon}\mathbf{j}_e \end{aligned} \tag{A.10}$$

Here, $\boldsymbol{\varepsilon} = \mathbf{E} + \frac{\nabla\mu}{e}$ as we mentioned above, and we applied the relationships: $\mathbf{j}_q = \mathbf{j}_\epsilon - \mu\mathbf{j}_n$ and $\mathbf{j}_e = -e\mathbf{j}_n$.

According to the Onsager relations in Equation (A.1), we have

$$\boldsymbol{\varepsilon}\mathbf{j}_e = (\rho\mathbf{j}_e + (\mathbf{L}_{EE})^{-1}\mathbf{L}_{ET}\nabla T)\mathbf{j}_e \tag{A.11}$$

and,

$$\begin{aligned} \nabla\mathbf{j}_q &= \nabla(\mathbf{L}_{TE}\boldsymbol{\varepsilon} + \mathbf{L}_{TT}(-\nabla T)) \\ &= \nabla(TS\mathbf{j}_e - \kappa(\nabla T)) \\ &= (\nabla T)S\mathbf{j}_e - T(\nabla S)\mathbf{j}_e + (\nabla\kappa)(\nabla T) \end{aligned} \tag{A.12}$$

Here, we use cubic symmetry, where the matrices $\mathbf{L}_{\alpha\beta}$ are diagonal. We also used the following relations: $\mathbf{L}_{EE}^{-1} = \rho$, where ρ is resistivity; and $\kappa = \mathbf{L}_{TT} - \mathbf{L}_{TE}(\mathbf{L}_{EE})^{-1}\mathbf{L}_{TE}$, where the second term is due to Peltier heat as we mentioned above.

From Equations (A.10) to (A.12), we have:

$$\frac{dq}{dt} = \rho\mathbf{j}_e^2 + \frac{d\kappa}{dT}(\nabla T)^2 - T\frac{dS}{dT}(\nabla T)\mathbf{j}_e \tag{A.13}$$

where the first term is Joule heating, the second term is heat conduction and the third term is Thomson heating/cooling. Then we find the Thomson coefficient and the second Kelvin relation:

$$\beta = \frac{(dq/dt)_{Thom}}{(\nabla T)j_e} = T\frac{dS}{dT} \tag{A.14}$$

In addition, Equation (A.13) indicate thats, although Joule heating and heat conduction is not reversible, one can determine the temperature derivative of the Seebeck coefficient by measuring the differences of bulk heating as the current direction is reversed. Therefore S can be derived at high temperatures by measuring Thomson coefficient as we mentioned in chapter 1.

Appendix B

Heat capacity of tunneling states

In chapter 4, a temperature linear dependent heat capacity has been applied for tunneling states of a two-level system. Here we derive the relationship in details mainly based on the work of Anderson [79] and Phillips [141] and the subsequent works of other researchers [146].

B.1 Heat capacity of a two-level system

The heat capacity of a two-level system is basically the Schottky anomaly in heat capacity. Suppose we have a two level system with energy ε_1 and ε_2 with $\varepsilon_2 - \varepsilon_1 = \varepsilon > 0$. According to the classical Maxwell-Boltzmann statistics, the total energy of the two-level system can be expressed as:

$$\begin{aligned} U &= \frac{\varepsilon_1 e^{-\varepsilon_1/k_BT} + \varepsilon_2 e^{-\varepsilon_2/k_BT}}{e^{-\varepsilon_1/k_BT} + e^{-\varepsilon_2/k_BT}} \\ &= \varepsilon_1 + \frac{\varepsilon}{e^{\varepsilon/k_BT}+1} \end{aligned} \tag{B.1}$$

where k_B is the Boltzmann constant. The heat capacity is thus written as:

$$\begin{aligned} C_{aTLS} &= \frac{dU}{dT} \\ &= \frac{\varepsilon^2}{k_BT^2}\frac{e^{-\varepsilon/k_BT}}{(e^{-\varepsilon/k_BT}+1)^2} \end{aligned} \tag{B.2}$$

B.2 Heat capacity of a tunneling-state system

A tunneling-state system can be schematically expressed by a two-level system as shown in Figure B.1 (a). The configuration of the double well potential is described in the figure. The energy difference (ε) between the two levels is expressed as:

$$\varepsilon = \sqrt{\triangle_0^2 + \triangle^2} \tag{B.3}$$

where $\triangle$ is the asymmetry of the two-level system and $\triangle_0$ is the splitting which describes the coupling between the two levels, and can be written as (WKB approximation):

$$\begin{aligned} \triangle_0 &= \hbar\omega_0 e^{-\lambda} \\ \lambda &= \sqrt{\frac{2mV}{\hbar^2}}d \end{aligned} \tag{B.4}$$

Here, $\hbar$ is the reduced Planck constant, $\hbar\omega_0$ is the ground state energy (zero point energy), λ is the tunneling parameter, m is the mass of the atoms trapped in the system, V is the barrier hight between the two wells and d is the distance between the two wells.

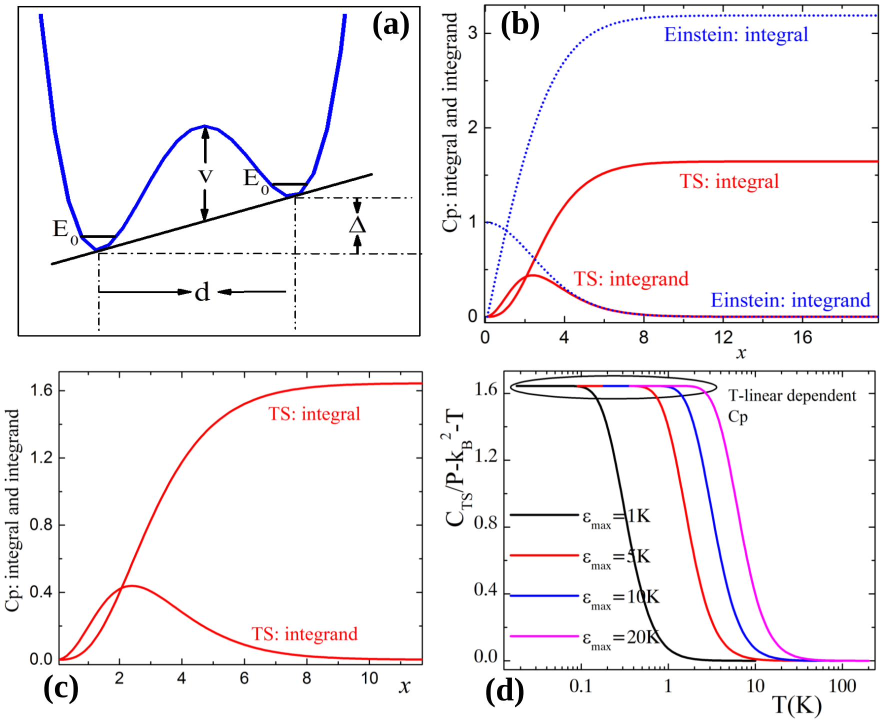

Figure B.1: Heat capacity due to tunneling states. (a) A sketched tunneling-state system: an asymmetric well. (b) A comparison between a tunnelling-state system and an Einstein-solid system. (c) The heat capacity a tunneling state is saturate at $x \simeq 10$. (d) Temperature-linear dependent heat capacity of a tunneling state.

Therefore, the heat capacity of a tunneling state is nothing but the heat capacity of a two-level system: eq. (B.2). Now we are considering many tunneling states, whose density of states (DOS) are expressed as follows.

$$P(\varepsilon, u)d\varepsilon\, du = \frac{P_0}{u\sqrt{1-u^2}}d\varepsilon\, du \tag{B.5}$$

where P_0 is a constant, $u = \triangle_0/\varepsilon$. According to Esquinazi *et al.*, if the measurement time is infinite, the DOS of tunneling states should be expressed as (in this case, the energy stored in the tunneling states releases completely):

$$P(\varepsilon, t \to \infty) = \int_{u_{min}}^{1} P(\varepsilon, u)du = P_0 \ln(\frac{2}{u_{min}}) \tag{B.6}$$

The heat capacity can be consequently derived as:

$$\begin{aligned} C_{TS}(T, t \to \infty) &= \int_0^\infty P(\varepsilon) C_{aTLS} d\varepsilon \\ &= P_0 \ln(\frac{2}{u_{min}}) k_B^2 T \int_0^\infty \frac{x^2 e^x}{(1+e^x)^2} dx \\ &= \frac{\pi^2}{6} k_B^2 P_0 \ln(\frac{2}{u_{min}}) T \end{aligned} \tag{B.7}$$

where C_{aTLS} is expressed in eq. (B.2) and $x = \varepsilon / k_B T$. The Equation (B.7) shows exactly the temperature-linear dependent heat capacity of tunneling states. However the density of tunneling states per volume (n), which is expressed as follows, tends to infinite if there isn't any constraint.

$$n = \int_0^\infty P(\varepsilon) d\varepsilon = \infty \tag{B.8}$$

So there must be an upper limit of energy (ε_{max}) for the integral (eq. (B.8)).

B.3 A simulation of the heat capacity due to tunneling states

In order to know ε_{max} as well as the feature of C_{TS}, a simulation is made as follows. We set,

$$\begin{aligned} f(x) &= C_{TS}(T, t \to \infty) / P_0 \ln(\frac{2}{u_{min}}) k_B^2 T \\ &= \int_0^\infty \frac{x^2 e^x}{(1+e^x)^2} dx = \int_0^\infty g(x) dx \end{aligned} \tag{B.9}$$

where $f(x)$ is the integral and $g(x)$ is the integrand. $f(x)$ and $g(x)$ are shown in Figure B.1 (b) as being compared with the situation in a Einstein-solid system (eq. (1.19)). The figure indicates that Einstein solids and tunneling states are intrinsically different. According to Figure B.1 (c), the integral $f(x)$ tends to saturate at around $x = 10$. This means that in order to have temperature-linear dependent heat capacity, x should be larger than 10, ie. $\frac{\varepsilon}{k_B T} > 10$ and $\varepsilon_{max} > 10 k_B T$.

We change the variable in eq. (B.9) from x to T (temperature), and the simulation result is shown in Figure B.1 (d). A temperature(T)-linear dependent behavior is clearly observed at low temperatures depending on the values of ε_{max}. Experimentally, the T-linear dependent heat capacity is observed below 1 K, which indicates that the value of ε_{max} should be larger than 10 K. With ε_{max}, one can calculate the density (n) of tunneling states as we did in chapter 4. The T-linear dependent heat capacity can be derived from other models as well, such as tunneling states under the soft potential model (SPM) [93] and a dipole-dipole interaction model proposed by Nakayama *et al.* [138].

B.4 Symmetric potential well vs. asymmetric potential well

A general question comes up: is the potential asymmetry ($\triangle$, shown in fig. B.1) really necessary for repeating a T-linear dependent heat capacity? The answer is yes, because in the case of a symmetric well, the energy splitting ($\triangle_0$) is very small and the two levels are quasi-degenerate and there is almost no additional heat due to tunneling states. For a clearer understanding, an estimation is shown below for reference.

According to fig. B.1 (a) and eqs. (B.3) and (B.4), in the case of a symmetric potential well: $\varepsilon = \triangle_0 = \hbar\omega_0 e^{-\lambda}$. Take BGSn as an example, the off-center displacement (r_0) of Ba(24k), estimated at 20 K, is 0.53 Å (Refer to table 4.1); if we assume that a Ba is rotating around the center as from one potential minimum to another, the distance between the nearest potential minima is $d = 0.53 \times \frac{\pi}{2} = 0.83$ Å. According to Ref. [73], a potential barrier V is estimated to be 2 meV, therefore we find $\lambda = \sqrt{\frac{2mV}{\hbar^2}}d \simeq 9.5$ and $\varepsilon \simeq \hbar\omega_0/13359.7$. According to Nakayama *et al.* [138], $\hbar\omega_0 \sim 4.6$ K and thus $\varepsilon \sim 0.00034$ K. This energy splitting is really small and the two levels can be regarded as quasi-degenerate. It should be noted that in the case of clathrates which show guest off-centered behavior, the corresponding off-centered potentials should be mostly symmetric, and only a small number of potentials are asymmetric as indicated by the small number (n) shown in table 4.2. It is also noted that in addition to the T-linear dependent heat capacity, there is a time dependent behavior as well [146], but it is beyond the description in this section.

List of Publications

[1] J. Wu, J. Xu, D. Prananto, H. Shimotani, Y. Tanabe, S. Heguri, K. Tanigaki. Systematic studies on anharmonicity of rattling phonons in type-I clathrates by low temperature heat capacity measurements. *Phys. Rev. B*, 89, 214301, (2014).

[2] J. Wu, K. Akagi, J. Xu, H. Shimotani, K. Tanigaki. Unification of boson peaks appearing in materials with cage structure (submitted).

[3] J. Xu, J. Wu, Y. Tanabe, S. Heguri, G. Mu, H. Shimotani, K. Tanigaki. Low-temperature physical and thermoelectric properties of $Ba_8Ni_5Ge_{41}$. *J. Electronic Materials*, 42, 2025 (2013).

[4] J. Xu, J. Wu, S. Heguri, G. Mu, Y. Tanabe, K. Tanigaki. Low-temperature physical properties of $Ba_8Ni_xGe_{46-x}$ (x = 3,4,6). *J. Electronic Material*s, 41, 1177 (2012).

[5] J. Xu, J. Wu, H. Shao, S. Heguri, Y. Tanabe, Y. Liu, G. Liu, J. Jiang, H. Jiang, K. Tanigaki. Structure and thermoelectric properties of the n-type clathrate $Ba_8Cu_{5.1}Ge_{40.2}Sn_{0.7}$, Journal of Material Chemistry A (Accepted).

[6] J. Xu, S. Heguri, Y. Tanabe, G. Mu, J. Wu, K. Tanigaki. Heat capacity studies on rattling vibrations in Ba-TM-Ge type-I clathrates. *J. Phys. Chem. Solids*, 73, 1521 (2012).

[7] G. Mu, B. Gao, X. Xie, Y. Tanabe, J. Xu, J. Wu, K. Tanigaki. Gap Structure of the Overdoped Iron-Pnictide Superconductor $Ba(Fe_{0.942}Ni_{0.058})_2As_2$: A Low-Temperature Specific-Heat Study. *Advances in Condensed Matter Physics*, 2015, 419017 (2015).

[8] K. Tanigaki, J. Wu, S. Heguri, J. Xu, D. Prananto, Y. Tanabe, H. Shimotani. Phonon anharmonicity and physical properties created by the endohedral atoms in material with nano-cage structures. *Solid State Physics*, 48, 471 (2013). (In Japanese)

List of Presentations

[1] APS March Meeting 2015 (San Antonio, TX, USA), Anharmonic phonons in type-I clathrates. J. Wu, H. Shimotani, K. Tanigaki, 3rd March 2015, (Oral).

[2] APS March Meeting 2014 (Denver, CO, USA), Studies on anharmonicity of rattling phonons in type-I clathrates by low temperature heat capacity measurements. J. Wu, Y. Tanabe, S. Heguri, H. Shimotani, K. Tanigaki, 6th March 2014, (Oral).

[3] The 32nd International Conference on Thermoelectrics, 2013 (Kobe, Japan), Harmonic and anharmonic phonons in clathrates and their applications to thermoelectric compounds. J. Wu, J. Xu, D. Prananto, S. Heguri, Y. Tanabe, H. Shimotani, K. Tanigaki, 2nd July 2013,(Oral).

[4] 17th International Symposium on Intercalation Compounds 2013 (Sendai, Japan), Low temperature specific heat study on type-I clathrates. J. Wu, J. Xu, D. Prananto, S. Heguri, Y. Tanabe, H. Shimotani, K. Tanigaki, 14th May 2013, (Poster).

[5] APS March Meeting 2013 (Baltimore, MD, USA), Low temperature specific heat study on type-I clathrate compounds. J. Wu, J. Xu, G. Mu, D. Prananto, Y. Tanabe, S. Heguri, H. Shimotani, K. Tanigaki, 21st March 2013, (Oral).

[6] MRS Fall Meeting & Exhibit 2012 (Boston, MA, USA), Low temperature specific heat study on thermoelectric type-I clathrates. J. Wu, J. Xu, G. Mu, D. Prananto, Y. Tanabe, S. Heguri, H. Shimotani, K. Tanigaki, 27th November 2012, (Oral).

[7] JPS Annual Autumn Meeting 2014 (Chubu University, Japan), Electrical and thermal properties study on Cu, Ag and Au containing type-I Clathrates. J. Wu, H. Suzuki, S. Heguri, Y. Tanabe, H. Shimotani, K. Tanigaki, 10th September 2014, (Oral).

[8] JPS Annual Spring Meeting 2014 (Tokai University, Japan), Physical properties study on noble metal containing type-I clathrate: Ba8MxGe46-x (M=Cu, Ag, Au), synthesized by Sn flux. J. Wu, Y. Tanabe, S. Heguri, H. Shimotani, K. Tanigaki, 27th March 2014, (Oral).

[9] JPS Annual Autumn Meeting 2013 (Tokushima University, Japan), Electrical and thermal properties study on Cu, Ag and Au containing type-I Clathrates. J. Wu, D. Prananto, S. Heguri, Y. Tanabe, H. Shimotani, K. Tanigaki, 27th September 2013, (Oral).

[10] JPS Annual Autumn Meeting 2012 (Yokohama National University, Japan), Low temperature specific heat study on type-I clathrates. J. Wu, J. Xu, G. Mu, D. Prananto, Y. Tanabe, S. Heguri, H. Shimotani, K. Tanigaki, 18th September 2012, (Oral).

[11] JPS Annual Spring Meeting 2012 (Kwansei Gakuin University, Japan), Discussion of magnetism in type-I clathrate compounds. J. Wu, J. Xu, S. Heguri, G. Mu, K. Tanigaki, 24th March 2012, (Oral).

Bibliography

[1] F. J. DiSalvo. Thermoelectric Cooling and Power Generation. *Science*, 285(30):703–706, 1999.

[2] G. J. Snyder and E. S. Toberer. Complex Thermoelectric Materials. *Nature Materials*, 7: 105–114, 2008.

[3] D. M. Rowe, editor. *Thermoelectrics Handbook.* CRC Press, Taylor & Francis Group, 2006.

[4] H. J. Goldsmid. *Introduction to Thermoelectricity.* Springer, 2006.

[5] K. Ikoma, M. Munekiyo, K. Furuya, M. Kobayashi, T. Izumi, and K. Shinohara. Thermoelectric Module and Generator for Gasoline Engine Vehicles. In *17th International Conference on Thermoelectrics*, pages 464–467, 1998.

[6] K. Matsubara. Development of a high efficient thermoelectric stack for a waste exhaust heat recovery of vehicles. In *21th International Conference on Thermoelectrics*, pages 418–423, 2002.

[7] L.D. Zhao, S.H. Lo, Y. Zhang, H. Sun, G. Tan, C. Uher, C. Wolverton, V. P. Dravid, and M. G. Kanatzidis. Ultralow Thermal Conductivity and High Thermoelectric Figure of Merit in SnSe Crystals. *Nature*, 508:373–377, 2014.

[8] M. C. Nicolaou. *Thermoelectric figure of merit of degenerate and nondegenerate semiconductors.* PhD thesis, Northeastern University, 2008.

[9] J. P. Jan, W. B. Pearson, and I. M. Templeton. Thermoelectricity at low temperatures V. The suitability of lead as a standard reference material. *Canadian Journal of Physics*, 36: 627–631, 1958.

[10] N. F. Mott and H. Jones. *The theory of the properties of metals and alloys.* Dover Publication, 1958.

[11] M. Cutler, J. F. Leavy, and R. L. Fitzpatrick. Electronic Transport in Semimetallic Cerium Sulfide. *Phys. Rev.*, 133:A1143–A1152, 1964.

[12] J. R. Sootsman, D. Y. Chung, and M. G. Kanatzidis. New and Old Concepts in Thermoelectric Materials. *Angewandte Chemie International Edition*, 48(46):8616–8639, 2009.

[13] Y. Pei, A. D. LaLonde, H. Wang, and G. J. Snyder. Low effective mass leading to high thermoelectric performance. *Energy Environ. Sci.*, 5:7963–7969, 2012.

[14] S. Bhattacharya, A. L. Pope, R. T. Littleton, T. M. Tritt, V. Ponnambalam, Y. Xia, and S. J. Poon. Effect of Sb doping on the thermoelectric properties of Ti-based half-Heusler compounds $\mathrm{TiNiSn}_{1-x}\mathrm{Sb}_x$. *Applied Physics Letters*, 77(16):2476–2478, 2000.

[15] J. L. Cohn, G. S. Nolas, V. Fessatidis, T. H. Metcalf, and G. A. Slack. Glasslike Heat Conduction in High-Mobility Crystalline Semiconductors. *Phys. Rev. Lett.*, 82:779–782, 1999.

[16] C. J. Vineis, A. Shakouri, A. Majumdar, and M. G. Kanatzidis. Nanostructured Thermoelectrics: Big Efficiency Gains from Small Features. *Advanced Materials*, 22(36):3970–3980, 2010. ISSN 1521-4095.

[17] Y. Lan, A. J. Minnich, G. Chen, and Z. Ren. Enhancement of Thermoelectric Figure-of-Merit by a Bulk Nanostructuring Approach. *Advanced Functional Materials*, 20(3):357–376, 2010.

[18] M. G. Kanatzidis. Nanostructured Thermoelectrics: The New Paradigm? *Chemistry of Materials*, 22(3):648–659, 2010.

[19] M. Christensen, A. B. Abrahamsen, N. B. Christensen, F. Juranyi, N. H. Andersen, K. Lefmann, J. Andreasson, C. R. H. Bahl, and B. B. Iversen. Avoided crossing of rattler modes in thermoelectric materials. *Nature Materials*, 7:811–815, 2008.

[20] B. C. Sales, D. Mandrus, and R. K. Williams. Filled skutterudite antimonides: A new class of thermoelectric materials. *SCIENCE*, 272(5266):1325–1328, 1996.

[21] O. Delaire, J. Ma, K. Marty, A. F. May, M. A. McGuire, M-H. Du, D. J. Singh, A. Podlesnyak, G. Ehlers, M. D. Lumsden, and B. C. Sales. Giant anharmonic phonon scattering in PbTe. *Nat Mater*, 10:614–619, 2011.

[22] R. Venkatasubramanian, E. Siivola, T. Colpitts, and B. O'Quinn. Thin-film thermoelectric devices with high room-temperature figures of merit. *Nature*, 413:597–602, 2001.

[23] D. J. Voneshen, K. Refson, E. Borissenko, M. Krisch, A. Bosak, A. Piovano, E. Cemal, M. Enderle, M. J. Gutmann, M. Hoesch, M. Roger, L. Gannon, A. T. Boothroyd, S. Uthayakumar, D. G. Porter, and J. P. Goff. Suppression of thermal conductivity by rattling modes in thermoelectric sodium cobaltate. *Nature Materials*, 12:1028–1032, 2013.

[24] X. Tang, Q. Zhang, L. Chen, T. Goto, and T. Hirai. Synthesis and thermoelectric properties of p-type- and n-type-filled skutterudite $\mathrm{R}_y\mathrm{M}_x\mathrm{Co}_{4-x}\mathrm{Sb}_{12}$ (R: Ce, Ba, Y; M: Fe, Ni). *Journal of Applied Physics*, 97(9):093712, 2005.

[25] A. Saramat, G. Svensson, A. E. C. Palmqvist, C. Stiewe, E. Mueller, D. Platzek, S. G. K. Williams, D. M. Rowe, J. D. Bryan, and G. D. Stucky. Large thermoelectric figure of merit at high temperature in Czochralski-grown clathrate $\mathrm{Ba}_8\mathrm{Ga}_{16}\mathrm{Ge}_{30}$. *Journal of Applied Physics*, 99(2):023708, 2006.

[26] H. Dave. The title is unknown. *Phil. Trans. Roy. Soc.*, 101:155, 1811.

[27] M. Faraday. The title is unkown. *Quart. J. Sci.*, 15:71, 1823.

[28] H. R. Mueller and M. von Stackelberg. The title is unknown. *Naturwiss*, 39:20, 1952.

[29] L. Pauling and R. E. Marsh. The structure of chlorine hydrate. *PNAS*, 38:112, 1952.

[30] G. A. Jeffrey. *Structural aspects of inclusion compounds formed by inorganic and organometallic host lattices.* Academic Press, London, 1984.

[31] J. S. Kasper, P. Hagenmuller, M. Pouchard, and C. Cros. Clathrate Structure of Silicon Na_8Si_{46} and Na_xSi_{136} ($x < 11$). *Science*, 150:1713–1714, 1965.

[32] S. Bobev and S. C. Sevov. Clathrate III of Group 14 Exists After All. *Journal of the American Chemical Society*, 123(14):3389–3390, 2001.

[33] U. Aydemir, L. Akselrud, W. Carrillo-Cabrera, C. Candolfi, N. Oeschler, M. Baitinger, F. Steglich, and Yu. Grin. BaGe5: A New Type of Intermetallic Clathrate. *Journal of the American Chemical Society*, 132(32):10984–10985, 2010.

[34] J. Fulmer, O. I. Lebedev, V. V. Roddatis, D. C. Kaseman, S. Sen, J. Dolyniuk, K. Lee, A. V. Olenev, and K. Kovnir. Clathrate $Ba_8Au_{16}P_{30}$: The "Gold Standard" for Lattice Thermal Conductivity. *Journal of the American Chemical Society*, 135(33):12313–12323, 2013.

[35] Shoji Yamanaka, Eiji Enishi, Hiroshi Fukuoka, and Masahiro Yasukawa. High-Pressure Synthesis of a New Silicon Clathrate Superconductor, Ba_8Si_{46}. *Inorganic Chemistry*, 39: 56–58, 2000.

[36] W. Carrillo-Cabrera, J. Curda, K. Peters, S. Paschen, M. Baenitz, Yu. Grin, and H. G. von Schnering. Crystal structure of the defect clathrate-I, Ba_8Ge_{43}. *Zeitschrift für Kristallographie - New Crystal Structures*, 215:321–322, 2000.

[37] G. K. Ramachandran, P. F. McMillan, J. Dong, and O. F. Sankey. $K_{7.62(1)}Si_{46}$ and $Rb_{6.15(2)}Si_{46}$: Two Structure I Clathrates with Fully Occupied Framework Sites. *Journal of Solid State Chemistry*, 154(2):626–634, 2000.

[38] Igor Veremchuk, Aron Wosylus, Bodo Böhme, Michael Baitinger, Horst Borrmann, Yurii Prots, Ulrich Burkhardt, Ulrich Schwarz, and Yuri Grin. Preparation and Crystal Structure of the Clathrate-I $Cs_{8-x}Ge_{44+y}\square_{2-y}$. *Zeitschrift für anorganische und allgemeine Chemie*, 637(10):1281–1286, 2011.

[39] Aron Wosylus, Igor Veremchuk, Walter Schnelle, Michael Baitinger, Ulrich Schwarz, and Yuri Grin. $Cs_{8-x}Si_{46}$: A Type-I Clathrate with Expanded Silicon Framework. *Chemistry – A European Journal*, 15(24):5901–5903, 2009.

[40] Andreas Kaltzoglou, Thomas Fassler, Mogens Christensen, Simon Johnsen, Bo Iversen, Igor Presniakov, Alexey Sobolev, and Andrei Shevelkov. Effects of the order-disorder phase transition on the physical properties of $A_8Sn_{44}\square_2$ (A = Rb, Cs). *J. Mater. Chem.*, 18: 5630–5637, 2008.

[41] K. Suekuni, M. A. Avila, K. Umeo, H. Fukuoka, S. Yamanaka, T. Nakagawa, and T. Takabatake. Simultaneous structure and carrier tuning of dimorphic clathrate $Ba_8Ga_{16}Sn_{30}$. *Phys. Rev. B*, 77:235119, 2008.

[42] J. H. Roudebush, N. Tsujii, A. Hurtando, H. Hope, Yu. Grin, and S. M. Kauzlarich. Phase Range of the Type-I Clathrate $Sr_8Al_xSi_{46-x}$ and Crystal Structure of $Sr_8Al_{10}Si_{36}$. *Inorganic Chemistry*, 51(7):4161–4169, 2012.

[43] S. B. Schujman, G. S. Nolas, R. A. Young, C. Lind, A. P. Wilkinson, G. A. Slack, R. Patschke, M. G. Kanatzidis, M. Ulutagay, and S.-J. Hwu. Structural analysis of $Sr_8Ga_{16}Ge_{30}$ clathrate compound. *Journal of Applied Physics*, 87(3):1529–1533, 2000.

[44] S. Paschen, W. Carrillo-Cabrera, A. Bentien, V. H. Tran, M. Baenitz, Yu. Grin, and F. Steglich. Structural, transport, magnetic, and thermal properties of $Eu_8Ga_{16}Ge_{30}$. *Phys. Rev. B*, 64:214404, 2001.

[45] A. Prokofiev, A. Sidorenko, K. Hradil, M. Ikeda, R. Svagera, M. Waas, H. Winkler, K. Neumaier, and S. Paschen. Thermopower enhancement by encapsulating cerium in clathrate cages. *Nat Mater*, 12:1096–1101, 2013.

[46] K. A. Kovnir, N. S. Abramchuk, J. V. Zaikina, M. Baitinger, U. Burkhardt, W. Schnelle, A. V. Olenev, O. I. Lebedev, G. V. Tendeloo, E. V. Dikarev, and A. V. Shevelkov. $Ge_{40.0}Te_{5.3}I_8$: synthesis, crystal structure, and properties of a new clathrate-I compound. *Z. Kristallogr.*, 221:527–532, 2006.

[47] Maria A. Kirsanova, Liudmila N. Reshetova, Andrei V. Olenev, Artem M. Abakumov, and Andrei V. Shevelkov. Semiclathrates of the Ge–P–Te System: Synthesis and Crystal Structures. *Chemistry - A European Journal*, 17:5719–5726, 2011.

[48] Yi Liu, Li-Ming Wu, Long-Hua Li, Shao-Wu Du, J. D. Corbett, and Ling Chen. The Antimony-Based Type-I Clathrate Compounds $Cs_8Cd_{18}Sb_{28}$ and $Cs_8Zn_{18}Sb_{28}$. *Angewandte Chemie International Edition*, 48:5305–5308, 2009.

[49] Sandra Scharfe, Florian Kraus, Saskia Stegmaier, Annette Schier, and Thomas F. Fässler. Zintl Ions, Cage Compounds, and Intermetalloid Clusters of Group 14 and Group 15 Elements. *Angewandte Chemie International Edition*, 50:3630–3670, 2011.

[50] C. Gatti, L. Bertini, N. P. Blake, and B. B. Iversen. Guest–Framework Interaction in Type I Inorganic Clathrates with Promising Thermoelectric Properties: On the Ionic versus Neutral Nature of the Alkaline-Earth Metal Guest A in $A_8Ga_{16}Ge_{30}$ (A = Sr, Ba). *Chemistry – A European Journal*, 9:4556–4568, 2003.

[51] Arčon Denis, Zorko Andrej, Jeglič Peter, Xu Jingtao, Tang Jun, Tanabe Yoichi, Heguri Satoshi, and Tanigaki Katsumi. Rattler Site Selectivity and Covalency Effects in Type-I Clathrates. *Journal of the Physical Society of Japan*, 82:014703, 2013.

[52] Alexander A. Demkov, Otto F. Sankey, K. E. Schmidt, Gary B. Adams, and Michael O'Keeffe. Theoretical investigation of alkali-metal doping in Si clathrates. *Phys. Rev. B*, 50:17001–17008, 1994.

[53] Mogens Christensen, Simon Johnsen, and Bo Brummerstedt Iversen. Thermoelectric clathrates of type I. *Dalton Trans.*, 39:978–992, 2010.

[54] B. C. Chakoumakos, B. C. Sales, D. G. Mandrus, and G. S. Nolas. Structural disorder and thermal conductivity of the semiconducting clathrate $Sr_8Ga_{16}Ge_{30}$. *Journal of Alloys and Compounds*, 296(1–2):80–86, 2000.

[55] Yuegang Zhang, Peter L. Lee, George. S. Nolas, and Angus P. Wilkinson. Gallium distribution in the clathrates $Sr_8Ga_{16}Ge_{30}$ and $Sr_4Eu_4Ga_{16}Ge_{30}$ by resonant diffraction. *Applied Physics Letters*, 80(16):2931–2933, 2002.

[56] Mogens Christensen, Nina Lock, Jacob Overgaard, and Bo B. Iversen. Crystal Structures of Thermoelectric n- and p-type $Ba_8Ga_{16}Ge_{30}$ Studied by Single Crystal, Multitemperature, Neutron Diffraction, Conventional X-ray Diffraction and Resonant Synchrotron X-ray Diffraction. *Journal of the American Chemical Society*, 128(49):15657–15665, 2006.

[57] Nick P. Blake, Dan Bryan, Susan Latturner, Lone Møllnitz, Galen D. Stucky, and Horia Metiu. Structure and stability of the clathrates $Ba_8Ga_{16}Ge_{30}$,$Sr_8Ga_{16}Ge_{30}$,$Ba_8Ga_{16}Si_{30}$, and $Ba_8In_{16}Sn_{30}$. *The Journal of Chemical Physics*, 114(22):10063–10074, 2001.

[58] B. C. Sales, B. C. Chakoumakos, R. Jin, J. R. Thompson, and D. Mandrus. Structural, magnetic, thermal, and transport properties of $X_8Ga_{16}Ge_{30}$ ($X = $Eu, Sr, Ba) single crystals. *Phys. Rev. B*, 63:245113, 2001.

[59] P. Toulemonde, Ch. Adessi, X. Blase, A. San Miguel, and J. L. Tholence. Superconductivity in the $(Ba_{1-x}Sr_x)_8Si_{46}$ clathrates ($x \leq 0.75$): Experimental and *ab initio* investigation. *Phys. Rev. B*, 71:094504, 2005.

[60] K. Tanigaki, T. Shimizu, K. M. Itoh, J. Teraoka, Y. Moritomo, and S. Yamanaka. Mechanism of superconductivity in the polyhedral-network compound Ba_8Si_{46}. *Nat Mater*, 2:653–655, 2003.

[61] Zenji Hiroi, Jun-ichi Yamaura, and Kazumasa Hattori. Rattling Good Superconductor: β-Pyrochlore Oxides AOs_2O_6. *Journal of the Physical Society of Japan*, 81(1):011012, 2012.

[62] Rüdiger F. W. Herrmann, Katsumi Tanigaki, Tetsuji Kawaguchi, Sadanori Kuroshima, and Otto Zhou. Electronic structure of Si and Ge gold-doped clathrates. *Phys. Rev. B*, 60: 13245–13248, 1999.

[63] R. C. Haddon. Magnetism of the carbon allotropes. *Nature*, 378:249–255, 1995.

[64] Terumasa Tadano, Yoshihiro Gohda, and Shinji Tsuneyuki. Impact of Rattlers on Thermal Conductivity of a Thermoelectric Clathrate: A First-Principles Study. *Phys. Rev. Lett.*, 114:095501, 2015.

[65] S. Pailhès, H. Euchner, V. M. Giordano, R. Debord, A. Assy, S. Gomès, A. Bosak, D. Machon, S. Paschen, and M. de Boissieu. Localization of Propagative Phonons in a Perfectly Crystalline Solid. *Phys. Rev. Lett.*, 113:025506, 2014.

[66] A. J. Sievers and S. Takeno. Isotope Shift of a Low-Lying Lattice Resonant Mode. *Phys. Rev.*, 140:A1030–A1032, 1965.

[67] W. A. Harrison. *Solid State Theory.* McGraw-Hill, New York, 1970.

[68] A. D. Caplin, G. Grüner, and J. B. Dunlop. $Al_{10}V$: An Einstein Solid. *Phys. Rev. Lett.*, 30: 1138–1140, 1973.

[69] A. I. Rykov, K. Nomura, T. Mitsui, and M. Seto. Low-energy excitations in brownmillerites and related oxides. *Physica B: Condensed Matter*, 350(4):287–304, 2004. ISSN 0921-4526.

[70] Raphaël P. Hermann, Rongying Jin, Werner Schweika, Fernande Grandjean, David Mandrus, Brian C. Sales, and Gary J. Long. Einstein Oscillators in Thallium Filled Antimony Skutterudites. *Phys. Rev. Lett.*, 90:135505, 2003.

[71] Hannu Mutka, Michael Marek Koza, Mark Robert Johnson, Zenji Hiroi, Jun-Ichi Yamaura, and Yohei Nagao. Generalized density-of-states and anharmonicity of the low-energy phonon bands from coherent inelastic neutron scattering response in the pyrochlore osmates AOs_2O_6 (A=K, Rb, Cs). *Phys. Rev. B*, 78:104307, 2008.

[72] Tetsuji Kume, Hiroshi Fukuoka, Toshihiro Koda, Shigeo Sasaki, Hiroyasu Shimizu, and Shoji Yamanaka. High-Pressure Raman Study of Ba Doped Silicon Clathrate. *Phys. Rev. Lett.*, 90:155503, 2003.

[73] T. Mori, K. Iwamoto, S. Kushibiki, H. Honda, H. Matsumoto, N. Toyota, M. A. Avila, K. Suekuni, and T. Takabatake. Optical Conductivity Spectral Anomalies in the Off-Center Rattling System β-$Ba_8Ga_{16}Sn_{30}$. *Phys. Rev. Lett.*, 106:015501, 2011.

[74] T. Mori, S. Goshima, K. Iwamoto, S. Kushibiki, H. Matsumoto, N. Toyota, K. Suekuni, M. A. Avila, T. Takabatake, T. Hasegawa, N. Ogita, and M. Udagawa. Optical conductivity of rattling phonons in type-I clathrate $Ba_8Ga_{16}Ge_{30}$. *Phys. Rev. B*, 79:212301, 2009.

[75] Jiazhen Wu, Jingtao Xu, Dwi Prananto, Hidekazu Shimotani, Yoichi Tanabe, Satoshi Heguri, and Katsumi Tanigaki. Systematic studies on anharmonicity of rattling phonons in type-I clathrates by low-temperature heat capacity measurements. *Phys. Rev. B*, 89: 214301, 2014.

[76] Jingtao Xu, Jun Tang, Kazumi Sato, Yoichi Tanabe, Hitoshi Miyasaka, Masahiro Yamashita, Satoshi Heguri, and Katsumi Tanigaki. Low-temperature heat capacity of $Sr_8Ga_{16}Ge_{30}$ and $Ba_8Ga_{16}Ge_{30}$: Tunneling states and electron-phonon interaction in clathrates. *Phys. Rev. B*, 82:085206, 2010.

[77] W. Qiu, L. Xi, P. Wei, X. Ke, J. Yang, and W. Zhang. Part-crystalline part-liquid state and rattling-like thermal damping in materials with chemical-bond hierarchy. *Proceedings of the National Academy of Sciences*, 111(42):15031–15035, 2014.

[78] H. Liu, X. Shi, F. Xu, L. Zhang, W. Zhang, L. Chen, Q. Li, C. Uher, T. Day, and G. J. Snyder. Copper ion liquid-like thermoelectrics. *Nature Materials*, 11:422–425, 2012.

[79] P. W. Anderson, B. I. Halperin, and C. M. Varma. Anomalous low-temperature thermal properties of glasses and spin glasses. *Philosophical Magazine*, 25(1):1–9, 1972.

[80] J. Xu, J. Wu, S. Heguri, G. Mu, Y. Tanabe, and K. Tanigaki. Low-temperature physical properties of $Ba_8Ni_xGe_{46-x}$ (x = 3, 4, 6). *Journal of Electronic Materials*, 41(6):1177–1180, 2012.

[81] Takeshi Rachi, Masaki Kitajima, Kensuke Kobayashi, FangZhun Guo, Takehito Nakano, Yuka Ikemoto, Keisuke Kobayashi, and Katsumi Tanigaki. Soft x-ray spectroscopy of $Ba_{24}Ge_{100}$: Electronic phase transition and Ba-atom rattling. *The Journal of Chemical Physics*, 123(7):074503, 2005.

[82] Jun Tang, Jingtao Xu, Satoshi Heguri, Hiroshi Fukuoka, Syoji Yamanaka, Koji Akai, and Katsumi Tanigaki. Electron-Phonon Interactions of Si_{100} and Ge_{100} Superconductors with Ba Atoms Inside. *Phys. Rev. Lett.*, 105:176402, 2010.

[83] Jun Tang, Takeshi Rachi, Ryotaro Kumashiro, Marcos A. Avila, Kouichirou Suekuni, Toshiro Takabatake, FangZhun Guo, Keisuke Kobayashi, Koji Akai, and Katsumi Tanigaki. Energetics of endohedral atoms in type-I clathrates observed by soft x-ray spectroscopy. *Phys. Rev. B*, 78:085203, 2008.

[84] M. A. Avila, K. Suekuni, K. Umeo, H. Fukuoka, S. Yamanaka, and T. Takabatake. Glasslike versus crystalline thermal conductivity in carrier-tuned $Ba_8Ga_{16}X_{30}$ clathrates ($X = Ge$, Sn). *Phys. Rev. B*, 74:125109, 2006.

[85] P. C. Canfield and Z. Fisk. Growth of single crystals from metallic fluxes. *Philosophical Magazine Part B*, 65(6):1117–1123, 1992.

[86] W. H. Bragg. The nature of Röntgen rays. *Transactions of the Royal Society of Science of Australia*, 31:94, 1907.

[87] B. H. Toby. EXPGUI, a graphical user interface for GSAS. *J. Appl. Cryst.*, 34:210–213, 2001.

[88] A. C. Larson and R. B. Von Dreele. General Structure Analysis System (GSAS). *Los Alamos National Laboratory Report LAUR*, 86:748, 1994.

[89] Louis J. Farrugia. WinGX and ORTEP for Windows: an update. *Journal of Applied Crystallography*, 45(4):849–854, 2012.

[90] Francesco Sette, Michael H. Krisch, Claudio Masciovecchio, Giancarlo Ruocco, and Giulio Monaco. Dynamics of Glasses and Glass-Forming Liquids Studied by Inelastic X-ray Scattering. *Science*, 280(5369):1550–1555, 1998.

[91] B. Frick and D. Richter. The Microscopic Basis of the Glass Transition in Polymers from Neutron Scattering Studies. *Science*, 267(5206):1939–1945, 1995.

[92] B. Hehlen, E. Courtens, R. Vacher, A. Yamanaka, M. Kataoka, and K. Inoue. Hyper-Raman Scattering Observation of the Boson Peak in Vitreous Silica. *Phys. Rev. Lett.*, 84:5355–5358, 2000.

[93] U. Buchenau, Yu. M. Galperin, V. L. Gurevich, and H. R. Schober. Anharmonic potentials and vibrational localization in glasses. *Phys. Rev. B*, 43:5039–5045, 1991.

[94] Y. Fan, T. Iwashita, and T. Egami. How thermally activated deformation starts in metallic glass. *Nature Communications*, 5:5083, 2014.

[95] Toshiro Takabatake, Koichiro Suekuni, Tsuneyoshi Nakayama, and Eiji Kaneshita. Phonon-glass electron-crystal thermoelectric clathrates: Experiments and theory. *Rev. Mod. Phys.*, 86:669–716, 2014.

[96] Walter Schirmacher, Gregor Diezemann, and Carl Ganter. Harmonic Vibrational Excitations in Disordered Solids and the "Boson Peak". *Phys. Rev. Lett.*, 81:136–139, 1998.

[97] S. N. Taraskin, Y. L. Loh, G. Natarajan, and S. R. Elliott. Origin of the Boson Peak in Systems with Lattice Disorder. *Phys. Rev. Lett.*, 86:1255–1258, 2001.

[98] H. Shintani and H. Tanaka. Universal link between the boson peak and transverse phonons in glass. *Nat. Mater.*, 7:870–877, 2008.

[99] J. S. Tse, D. D. Klug, J. Y. Zhao, W. Sturhahn, E. E. Alp, J. Baumert, C. Gutt, M. R. Johnson, and W. Press. Anharmonic motions of Kr in the clathrate hydrate. *Nat. Mater.*, 4:917–921, 2005.

[100] J. Xu, S. Heguri, Y. Tanabe, J. Mu, G. Wu, and K. Tanigaki. Heat capacity studies on rattling vibrations in Ba type I clathrates. *J. Phys. Chem. Solids*, 73:1521–1523, 2012.

[101] U. Aydemir, C. Candolfi, A. Ormeci, Y. Oztan, M. Baitinger, N. Oeschler, F. Steglich, and Yu. Grin. Low-temperature thermoelectric, galvanomagnetic, and thermodynamic properties of the type-I clathrate $\mathrm{Ba_8Au_xSi_{46-x}}$. *Phys. Rev. B*, 84:195137, 2011.

[102] M. Falmbigl, M. X. Chen, A. Grytsiv, P. Rogl, E. Royanian, H. Michor, E. Bauer, R. Podloucky, and G. Giester. Type-I clathrate $\mathrm{Ba_8Ni_xSi_{46-x}}$: Phase relations, crystal chemistry and thermoelectric properties. *Dalton Trans.*, 41:8839–8849, 2012.

[103] K. Suekuni, M. A. Avila, K. Umeo, and T. Takabatake. Cage-size control of guest vibration and thermal conductivity in $\mathrm{Sr_8Ga_{16}Si_{30-x}Ge_x}$. *Phys. Rev. B*, 75:195210, 2007.

[104] S. Stefanoski, J. Martin, and G. S. Nolas. Low temperature transport properties and heat capacity of single-crystal $\mathrm{Na_8Si_{46}}$. *J. Phys. Condens. Matter*, 22:485404, 2010.

[105] D. Nataraj and J. Nagao. Structure and Raman scattering study on $\mathrm{Ba_8Ga_xSi_{46-x}}$ ($x = 10$ and 16) type I clathrates. *J. Solid State Chem.*, 177:1905–1911, 2004.

[106] A. Bentien, B. B. Iversen, J. D. Bryan, G. D. Stucky, A. E. C. Palmqvist, A. J. Schultz, and R. W. Henning. Maximum entropy method analysis of thermal motion and disorder in thermoelectric clathrate $\mathrm{Ba_8Ga_{16}Si_{30}}$. *Journal of Applied Physics*, 91(9):5694–5699, 2002.

[107] S. Johnsen, M. Christensen, B. Thomsen, G. K. H. Madsen, and B. B. Iversen. Barium dynamics in noble-metal clathrates. *Phys. Rev. B*, 82:184303, 2010.

[108] H. Shimizu, Y. Takeuchi, T. Kume, S. Sasaki, K. Kishimoto, N. Ikeda, and T. Koyanagi. Raman spectroscopy of type-I and type-VIII silicon clathrate alloys $\mathrm{Sr_8Al_xGa_{16-x}Si_{30}}$. *Journal of Alloys and Compounds*, 487(1–2):47–51, 2009.

[109] M. Christensen, S. Johnsen, F. Juranyi, and B. B. Iversen. Clathrate guest atoms under pressure. *Journal of Applied Physics*, 105:073508, 2009.

[110] M. Christensen and B. B. Iversen. Host–guest coupling in semiconducting $\mathrm{Ba_8Zn_8Ge_{38}}$. *Journal of Physics: Condensed Matter*, 20(10):104244, 2008.

[111] Simon Johnsen, Anders Bentien, Georg K. H. Madsen, Mats Nygren, and Bo B. Iversen. Crystal structure and transport properties of nickel containing germanium clathrates. *Phys. Rev. B*, 76:245126, 2007.

[112] T. Tanaka, T. Onimaru, K. Suekuni, S. Mano, H. Fukuoka, S. Yamanaka, and T. Takabatake. Interplay between thermoelectric and structural properties of type-I clathrate $\mathrm{K_8Ga_8Sn_{38}}$ single crystals. *Phys. Rev. B*, 81:165110, 2010.

[113] Tetsuji Kume, Toshihiro Koda, Shigeo Sasaki, Hiroyasu Shimizu, and John S. Tse. High-pressure Raman study of the potassium-doped silicon clathrate $\mathrm{K_8Si_{46}}$. *Phys. Rev. B*, 70: 052101, 2004.

[114] Hiroyasu Shimizu, Takahiko Imai, Tetsuji Kume, Shigeo Sasaki, Andreas Kaltzoglou, and Thomas F. Fässler. Raman spectroscopy study of type-I clathrates A_8Sn_{44} ($A = Rb$, Cs) and $Rb_8Hg_4Sn_{42}$. *Chemical Physics Letters*, 464:54–57, 2008.

[115] M. J. et al. Frisch. Gaussian 09, Revision D. 01. Technical report, Gaussian, Inc., Wallingford CT, 2009.

[116] Axel D. Becke. Density-functional thermochemistry. III. The role of exact exchange. *The Journal of Chemical Physics*, 98(7):5648–5652, 1993.

[117] Chengteh Lee, Weitao Yang, and Robert G. Parr. Development of the Colle-Salvetti correlation-energy formula into a functional of the electron density. *Phys. Rev. B*, 37: 785–789, 1988.

[118] Vitaly A. Rassolov, Mark A. Ratner, John A. Pople, Paul C. Redfern, and Larry A. Curtiss. 6-31G* basis set for third-row atoms. *Journal of Computational Chemistry*, 22(9):976–984, 2001.

[119] P. Jeffrey Hay and Willard R. Wadt. Ab initio effective core potentials for molecular calculations. Potentials for K to Au including the outermost core orbitals. *The Journal of Chemical Physics*, 82:299–310, 1985.

[120] G. Kresse and J. Furthmüller. Efficient iterative schemes for *ab initio* total-energy calculations using a plane-wave basis set. *Phys. Rev. B*, 54:11169–11186, 1996.

[121] P. E. Blöchl. Projector augmented-wave method. *Phys. Rev. B*, 50:17953–17979, 1994.

[122] G. Kresse and D. Joubert. From ultrasoft pseudopotentials to the projector augmented-wave method. *Phys. Rev. B*, 59:1758–1775, 1999.

[123] John P. Perdew, Kieron Burke, and Matthias Ernzerhof. Generalized Gradient Approximation Made Simple. *Phys. Rev. Lett.*, 77:3865–3868, 1996.

[124] R. H. Stokes. The van der Waals Radii of Gaseous Ions of the Noble Gas Structure in Relation to Hydration Energies. *Journal of the American Chemical Society*, 86(6):979–982, 1964.

[125] Manjeera Mantina, Adam C. Chamberlin, Rosendo Valero, Christopher J. Cramer, and Donald G. Truhlar. Consistent van der Waals Radii for the Whole Main Group. *The Journal of Physical Chemistry A*, 113(19):5806–5812, 2009.

[126] A. Bondi. van der Waals volumes and radii. *J. Phys. Chem.*, 68:441–451, 1964.

[127] Philip M. Morse. Diatomic Molecules According to the Wave Mechanics. II. Vibrational Levels. *Phys. Rev.*, 34:57–64, 1929.

[128] Yu. P. Mitrofanov, M. Peterlechner, S. V. Divinski, and G. Wilde. Impact of Plastic Deformation and Shear Band Formation on the Boson Heat Capacity Peak of a Bulk Metallic Glass. *Phys. Rev. Lett.*, 112:135901, 2014.

[129] G. S. Nolas, J. L. Cohn, G. A. Slack, and S. B. Schujman. Semiconducting Ge clathrates: Promising candidates for thermoelectric applications. *Applied Physics Letters*, 73(2): 178–180, 1998.

[130] V. L. Kuznetsov, L. A. Kuznetsova, A. E. Kaliazin, and D. M. Rowe. Preparation and thermoelectric properties of $A_8^{II}B_{16}^{III}B_{30}^{IV}$ clathrate compounds. *Journal of Applied Physics*, 87(11):7871–7875, 2000.

[131] G. A. Slack. *New Materials and Performance Limits for Thermoelectric Cooling. In CRC Handbook of Thermoelectrics.* CRC Press: Boca Raton, FL, 1995.

[132] Akihiko Fujiwara, Kunihisa Sugimoto, Che-Hsiu Shih, Hiroshi Tanaka, Jun Tang, Yoichi Tanabe, Jingtao Xu, Satoshi Heguri, Katsumi Tanigaki, and Masaki Takata. Quantitative relation between structure and thermal conductivity in type-I clathrates $X_8Ga_{16}Ge_{30}$ (X = Sr, Ba) based on electrostatic-potential analysis. *Phys. Rev. B*, 85:144305, 2012.

[133] Xiang Zheng, Sergio Y. Rodriguez, and Joseph H. Ross. NMR relaxation and rattling phonons in the type-I $Ba_8Ga_{16}Sn_{30}$ clathrate. *Phys. Rev. B*, 84:024303, 2011.

[134] Hideki Tou, Kanto Sonoda, Kazuya Furumoto, Hisashi Kotegawa, Koichiro Suekuni, Marcos A. Avila, and Toshiro Takabatake. Strong Coupling of Rattling Phonon to Conduction Electrons in Semimetallic Type-I Clathrate $Ba_8Ga_{16}Sn_{30}$. *Journal of the Physical Society of Japan*, 82(11):114603, 2013.

[135] K. Suekuni, Y. Takasu, T. Hasegawa, N. Ogita, M. Udagawa, M. A. Avila, and T. Takabatake. Off-center rattling modes and glasslike thermal conductivity in the type-I clathrate $Ba_8Ga_{16}Sn_{30}$. *Phys. Rev. B*, 81:205207, 2010.

[136] Isao Ishii, Yasuhiko Suetomi, Takahiro K. Fujita, Koichiro Suekuni, Tomoo Tanaka, Toshiro Takabatake, Takashi Suzuki, and Marcos A. Avila. Lattice instability and elastic dispersion due to the rattling motion in the type-I clathrate $Ba_8Ga_{16}Sn_{30}$. *Phys. Rev. B*, 85:085101, 2012.

[137] M. A. Ramos and U. Buchenau. *Tunneling Systems in Amorphous and Crystalline Solids.* Springer, Berlin, 1998.

[138] T. Nakayama and E. Kanashita. Interacting dipoles in typ-I clathrates: Why glass-like though crystalline? *EPL (Europhysics Letters)*, 84(6):66001, 2008.

[139] A. Bentien, M. Christensen, J. D. Bryan, A. Sanchez, S. Paschen, F. Steglich, G. D. Stucky, and B. B. Iversen. Thermal conductivity of thermoelectric clathrates. *Phys. Rev. B*, 69: 045107, 2004.

[140] R. D. Shannon. Revised effective ionic radii and systematic studies of interatomic distances in halides and chalcogenides. *Acta Crystallogr., Sect. A: Cryst. Phys., Diffr., Theor. Gen. Crystallogr.*, 32:751–767, 1976.

[141] W.A. Phillips. Tunneling states and the low-temperature thermal expansion of glasses. *Journal of Low Temperature Physics*, 11:757–763, 1973.

[142] J. Tang, R Kumashiro, J. Ju, Z. Li, M. A. Avila, K. Suekuni, T. Takabatake, F. Guo, K. Kobayashi, and K. Tanigaki. p- and n-Type $Ba_8Ga_{16}Ge_{30}$ studied by X-ray photoelectron spectroscopy. *Chemical Physics Letters*, 472(1–3):60–64, 2009.

[143] Martin Deye and Pablo Esquinazi. Time and temperature dependence of the specific heat of non-crystalline solids within the tunneling model. *Zeitschrift für Physik B Condensed Matter*, 76(3):283–288, 1989. ISSN 0722-3277.

[144] P. L. Kapitza. The Study of Heat Transfer in Helium II. *Zh. Eksp. Teor. Fiz. Pis'ma Red.*, 11:1–31, 1941.

[145] *PPMS (Quantum Design) manual "Anomalously Low Heat Capacity Below 1K" Heat Capacity Application Note 1085-151*, on line.

[146] A. Nittke, S. Sahling, and P. Esquinazi. *Tunneling Systems in Amorphous and Crystalline Solids, Chapter 2.* Springer, Berlin, 1998.

[147] Takeshi Rachi, Harukazu Yoshino, Ryotaro Kumashiro, Masaki Kitajima, Kensuke Kobayashi, Keiichi Yokogawa, Keizo Murata, Noriaki Kimura, Haruyoshi Aoki, Hiroshi Fukuoka, Syoji Yamanaka, Hidekazu Shimotani, Taishi Takenobu, Yoshihiro Iwasa, Takahiko Sasaki, Norio Kobayashi, Yuji Miyazaki, Kazuya Saito, FangZhun Guo, Keisuke Kobayashi, Keiichi Osaka, Kenichi Kato, Masaki Takata, and Katsumi Tanigaki. Superconductivity and physical properties of $Ba_{24}Si_{100}$ determined from electric transport, specific-heat capacity, and magnetic susceptibility measurements. *Phys. Rev. B*, 72:144504, 2005.

[148] Sebastian Christensen, Marcos A. Avila, Koichiro Suekuni, Ross Piltz, Toshiro Takabatake, and Mogens Christensen. Combined X-ray and neutron diffraction study of vacancies and disorder in the dimorphic clathrate Ba8Ga16Sn30 of type I and VIII. *Dalton Trans.*, 42: 14766–14775, 2013.

[149] A. P. Ramirez, M. J. Rosseinsky, D. W. Murphy, and R. C. Haddon. Specific-heat jump at T_c and normal-state magnetic susceptibility of A_3C_{60}. *Phys. Rev. Lett.*, 69:1687–1690, 1992.

[150] Vladimir Z. Kresin. On the critical temperature for any strength of the electron-phonon coupling. *Physics Letters A*, 122(8):434–438, 1987.

[151] Xun Shi, Jiong Yang, Shengqiang Bai, Jihui Yang, Hsin Wang, Miaofang Chi, James R. Salvador, Wenqing Zhang, Lidong Chen, and Winnie Wong-Ng. On the Design of High-Efficiency Thermoelectric Clathrates through a Systematic Cross-Substitution of Framework Elements. *Advanced Functional Materials*, 20(5):755–763, 2010.

[152] Hui Zhang, Horst Borrmann, Niels Oeschler, Christophe Candolfi, Walter Schnelle, Marcus Schmidt, Ulrich Burkhardt, Michael Baitinger, Jing-Tai Zhao, and Yuri Grin. Atomic Interactions in the p-Type Clathrate I $Ba_8Au_{5.3}Ge_{40.7}$. *Inorganic Chemistry*, 50(4):1250–1257, 2011.

[153] Kengo Kishimoto, Yuta Sasaki, Tsuyoshi Koyanagi, Kenji Ohoyama, and Koji Akai. Crystal structure and thermoelectric properties of $K_xBa_{8-x}Zn_yGe_{46-y}$ clathrates. *Journal of Applied Physics*, 111(9):093716, 2012.

[154] H. Anno, M. Hokazono, H. Takakura, and K. Matsubara. Thermoelectric Properties of $Ba_8Au_xGe_{46-x}$ Clathrate Compounds. In *24th International Conference on Thermoelectrics*, pages 102–105, 2005.

[155] I. Zeiringer, N. Meinychenko-Koblyuk, A. Grytsiv, E. Bauer, G. Giester, and P. Rogl. Phase Equilibria, Crystal Chemistry and Physical Properties of Au-Ba-Ge Clathrates. *Journal of Phase Equilibria and Diffusion*, 32:115–127, 2011.

[156] I. Zeiringer, M. Chen, I. Bednar, E. Royanian, E. Bauer, R. Podloucky, A. Grytsiv, P. Rogl, and H. Effenberger. Phase Equilibria, Crystal Chemistry and Physical Properties of Au-Ba-Ge Clathrates. *Acta Materialia*, 59:2368–2384, 2011.

[157] Z. Ye, J. Cho, M. M. Tessema, J. R. Salvador, R. A. Waldo, J-H. Yang, H. Wang, W. Cai, M. J. Kirkham, J. Yang, and W. Zhang. Thermoelectric properties of Au-containing type-I clathrates $Ba_8Au_xGa_{16-3x}Ge_{30+2x}$. *Journal of Alloys and Compounds*, 587:747–754, 2014.

[158] G Cordier and P. Woll. Neue ternäre intermetallische Verbindungen mit Clathratstruktur: $Ba_8(T,Si)_6Si_{40}$ und $Ba_6(T,Ge)_6Ge_{40}$ mit T = Ni, Pd, Pt, Cu, Ag, Au. *Journal of the Less Common Metals*, 169(2):291–302, 1991.

[159] Y. Li, J. Chi, W Gou, S. Khandekar, and J. H. Ross Jr. Structure and stability of Ba-Cu-Ge type-I clathrates. *Journal of Physics: Condensed Matter*, 15(32):5535, 2003.

[160] J. Xu, J. Wu, H. Shao, S. Heguri, Y. Tanabe, Y. Liu, G. Liu, J. Jiang, H. Jiang, and K. Tanigaki. Structure and thermoelectric properties of the n-type clathrate $Ba_8Cu_{5.1}Ge_{40.2}Sn_{0.7}$. Accepted, 2015.

[161] Jing-Han Chen, Ali Sirusi Arvij, Xiang Zheng, Sergio Y. Rodriguez, and Jr. Joseph H. Ross. NMR and computational study of $Ba_8Cu_xGe_{46-x}$ clathrate semiconductors. *Journal of Alloys and Compounds*, 593:261–266, 2014.

[162] Takeshi Rachi, Katsumi Tanigaki, Ryotaro Kumashiro, Kensuke Kobayashi, Harukazu Yoshino, Keizo Murata, Hiroshi Fukuoka, Syoji Yamanaka, Hidekazu Shimotani, Taishi Takenobu, Yoshihiro Iwasa, Takahiko Sasaki, Norio Kobayashi, Yuji Miyazaki, and Kazuya Saito. Specific heat capacity and magnetic susceptibility of superconducting $Ba_{24}Si_{100}$. *Journal of Physics and Chemistry of Solids*, 67(5–6):1334–1337, 2006.

[163] C. Candolfi, U. Aydemir, A. Ormeci, M. Baitinger, N. Oeschler, F. Steglich, and Yu. Grin. Low-temperature magnetic, galvanomagnetic, and thermoelectric properties of the type-I clathrates $Ba_8Ni_xSi_{46-x}$. *Phys. Rev. B*, 83:205102, 2011.

[164] Christian Cros, Michel Pouchard, and Paul Hagenmuller. Sur une nouvelle famille de clathrates minéraux isotypes des hydrates de gaz et de liquides. Interprétation des résultats obtenus. *Journal of Solid State Chemistry*, 2(4):570–581, 1970. ISSN 0022-4596.

[165] Rodica M. Candea, C. M. Gee, S. J. Hudgens, and Marc Kastner. Temperature dependence of the diamagnetic and dielectric susceptibility of silicon. *Phys. Rev. B*, 16:2657–2662, Sep 1977.

[166] S. Hudgens, Marc Kastner, and H. Fritzsche. Diamagnetic Susceptibility of Tetrahedral Semiconductors. *Phys. Rev. Lett.*, 33:1552–1555, Dec 1974.

[167] N. W. Ashcroft and N. D. Mermin. *Solid State Physics*. Thomson Learning, 1976.

[168] P. W. Selwood, editor. *Magnetochemistry*. Interscience, New York, 1956.

[169] Julia V. Zaikina, Walter Schnelle, Kirill A. Kovnir, Andrei V. Olenev, Yuri Grin, and Andrei V. Shevelkov. Crystal structure, thermoelectric and magnetic properties of the type-I clathrate solid solutions $Sn_{24}P_{19.3(2)}Br_xI_{8-x}$ ($0\leq\ x\ \leq 8$) and $Sn_{24}P_{19.3(2)}Cl_yI_{8-y}$ ($y \leq 0.8$). *Solid State Sciences*, 9(8):664–671, 2007. ISSN 1293-2558.

[170] D. J. Chadi, R. M. White, and W. A. Harrison. Theory of the Magnetic Susceptibility of Tetrahedral Semiconductors. *Phys. Rev. Lett.*, 35:1372–1375, Nov 1975.

[171] Stephen J. Hudgens. Effect of Disorder on the Temperature-Independent Magnetic Susceptibility of Se and Ge. *Phys. Rev. B*, 7:2481–2485, Mar 1973.